Vol. 1, No. 4, December 2025
jams.hsu.ac.ir

JOURNAL OF APPLIED MATERIAL SCIENCE

Hakim Sabzevari University

JOURNAL OF
APPLIED
MATERIAL
SCIENCE
jams.hsu.ac.ir

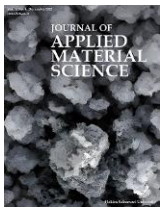

Contents

Volume 1, No. 4, December 2025

Editorial 210149

Aims and scope of the journal, a brief submission guideline, and the list of the editorial board.

Ahmad Allahbakhsh

doi: 10.22034/jams.2025.210149

Comparison of the Corrosion Inhibition Effect of *Portulaca oleracea* Extracts ..... 210150 Prepared Using Ethanol and Water

In this study, Shiri developed a new class of sustainable coating for mild steel using extracts from *Portulaca oleracea*, prepared with two solvents: ethanol and water. The results indicate that the choice of solvent significantly influences the corrosion inhibition efficiency of the resulting inhibitor, highlighting more effective methods for creating sustainable corrosion protection systems.

Sara Shiri

doi: 10.22034/jams.2025.210150

Synthesis and Characterization of Polyethylene Glycol Coated Superparamagnetic ..... 210151 Fe_3O_4 Nanoparticles

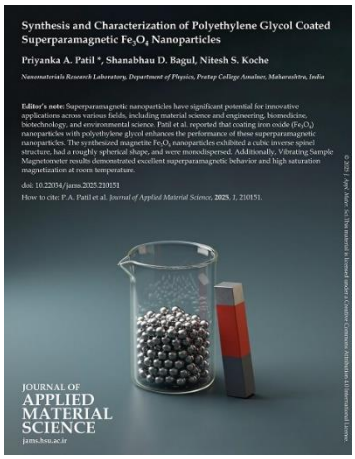

Patil et al. reported that coating iron oxide (Fe_3O_4) nanoparticles with polyethylene glycol enhances the performance of these superparamagnetic nanoparticles. The synthesized magnetite Fe_3O_4 nanoparticles exhibited a cubic inverse spinel structure, had a roughly spherical shape, and were monodispersed. Additionally, Vibrating Sample Magnetometer results demonstrated excellent superparamagnetic behavior and high saturation magnetization at room temperature.

Priyanka A. Patil, Shanabhau D. Bagul, Nitesh S. Koche

doi: 10.22034/jams.2025.210151

© 2025 *J. Appl. Mater. Sci.* This material is licensed under a Creative Commons Attribution 4.0 International License.

Deep Eutectic Solvent-Water Solvated Synthesis of Tungsten Oxide Nanoparticles with Photochromic and Antimicrobial Properties 210152

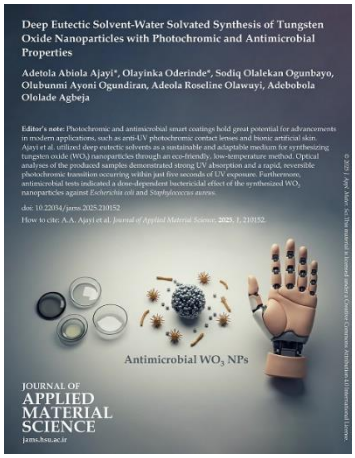

Ajayi et al. utilized deep eutectic solvents as a sustainable and adaptable medium for synthesizing tungsten oxide (WO_3) nanoparticles through an eco-friendly, low-temperature method. Optical analyses of the produced samples demonstrated strong UV absorption. Furthermore, antimicrobial tests indicated a dose-dependent bactericidal effect of the synthesized WO_3 nanoparticles against *Escherichia coli* and *Staphylococcus aureus*.

Adetola Abiola Ajayi, Olayinka Oderinde, Sodiq Olalekan Ogunbayo, Olubunmi Ayoni Ogundiran, Adeola Roseline Olawuyi, Adebobola Ololade Agbeja

doi: 10.22034/jams.2025.210152

Evaluation of *Phytolacca americana* L. extract as green corrosion inhibitor for mild steel: a study of the solution phase 210153

Green corrosion inhibitors are gaining popularity, particularly those derived from plants, due to their non-toxic nature, affordability, and accessibility. Sheydaei conducted a study on the extract of *Phytolacca americana* L. (also known as American pokeweed), assessing its effectiveness in preventing mild steel corrosion. The findings indicated that the plant extract successfully inhibited corrosion, as it contains compounds such as betacyanins, flavonoids, and polyphenols.

Milad Sheydaei

doi: 10.22034/jams.2025.210153

Preparation and Characterization of a Ni-Co-Ce Coordination Framework Coated Nickel Foam Electrode for Supercapacitor Applications 210154

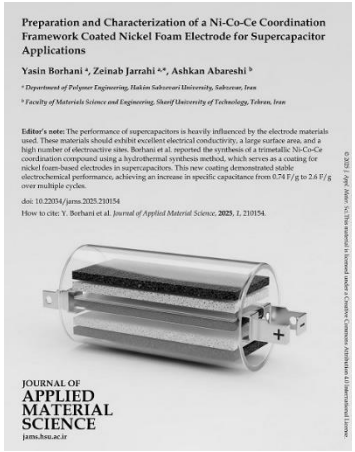

Borhani et al. reported the synthesis of a trimetallic Ni-Co-Ce coordination compound using a hydrothermal synthesis method, which serves as a coating for nickel foam-based electrodes in supercapacitors. This new coating demonstrated stable electrochemical performance, achieving an increase in specific capacitance from 0.74 F/g to 2.6 F/g over multiple cycles.

Yasin Borhani, Zeinab Jarrahi, Ashkan Abareshi

doi: 10.22034/jams.2025.210154

© 2025 *J. Appl. Mater. Sci.* This material is licensed under a Creative Commons Attribution 4.0 International License.

Fabrication, Testing, and Optimization of MWCNT Epoxy Polymer Nanocomposites Through Taguchi, TOPSIS, and Response Surface Techniques 210155

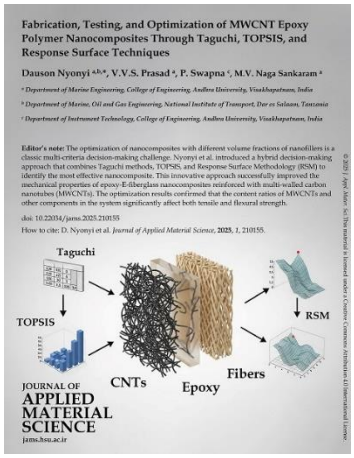

Nyonyi et al. introduced a hybrid decision-making approach that combines Taguchi methods, TOPSIS, and Response Surface Methodology (RSM) to identify the most effective nanocomposite. This innovative approach successfully improved the mechanical properties of epoxy-E-fiberglass nanocomposites reinforced with multi-walled carbon nanotubes (MWCNTs). The optimization results confirmed that the content ratios of MWCNTs and other components in the system significantly affect both tensile and flexural strength

Dauson Nyonyi, V.V.S. Prasad, P. Swapna, M.V. Naga Sankaram

doi: 10.22034/jams.2025.210155

ABOUT COVER

Graphene quantum dots, much like the well-known reduced graphene oxide aerogels, can be transformed into hydrogels and aerogels using the hydrothermal reduction process. The cover showcases a regenerated image derived from a Scanning Electron Microscope image of highly porous aerogels created through the hydrothermal reduction of graphene quantum dots derived from citric acid.

(Note: The covers of this journal are created in part using artificial intelligence (AI) technologies, with direct human supervision. AI and AI-assisted technologies are permitted only for generating graphical abstract suggestions. If such technologies are used in the manuscript preparation, it must be clearly disclosed in the Acknowledgments section.)

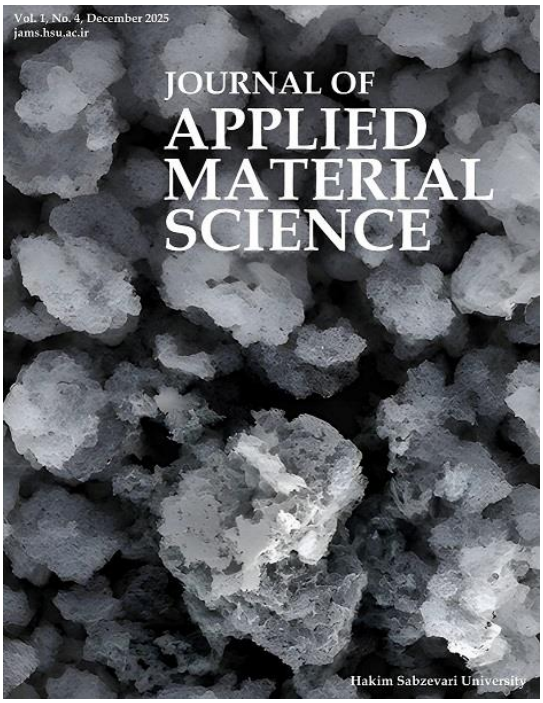

© 2025 *J. Appl. Mater. Sci.* This material is licensed under a Creative Commons Attribution 4.0 International License.

jams.hsu.ac.ir JOURNAL OF APPLIED MATERIAL SCIENCE

Journal of Applied Material Science:

an *open-access* platform to publish scientific developments in all aspects of material science under the *highest publication standards* and *the fastest peer-review process*

The Journal of Applied Material Science publishes original research in the form of ***communications*** and ***full papers***, as well as ***reviews***, invited ***mini-reviews***, and invited research news. Publication in this journal is **entirely free of charge**, and all accepted papers will be available online immediately after typesetting. Dr. Ahmad Allahbakhsh, along with an international team of editors, leads the journal to meet the highest publication standards. We are looking forward to receiving your submissions.

Editor-in-Chief: Dr. Ahmad Allahbakhsh (Hakim Sabzevari University)

Director in charge: Prof. Gholamali Farzi (Hakim Sabzevari University)

International Editorial Board Members:

Prof. Ahmad Reza Bahramian (Tarbiat Modares University),
Prof. Mohammadhosein (Momo) Safari (Hasselt University),
Prof. Denis Rodrigue (Laval University),
Prof. Ursula Windberger (Medical University of Vienna),
Prof. Gholamali Farzi (Hakim Sabzevari University),
Prof. Sabu Thomas (Mahatma Gandhi University),
Dr. Hamidreza Oveisi (Hakim Sabzevari University),
Prof. Manoj Balachandran (CHRIST University),
Prof. Raffaella Mancuso (University of Calabria),
Dr. Ahmad Allahbakhsh (Hakim Sabzevari University)

Journal of Applied Material Science is an open-access journal, which means that all content is freely available without charge to the users and institutions. Users are allowed to read, download, copy, distribute, print, search, or link to the full texts of the articles, or use them for any other lawful purpose, without asking prior permission from the publisher or the author. This is in accordance with the BOAI definition of open access. Authors are free to deposit a copy of their paper (Published version, Version of Record) in an institutional or other repository of their choice.

To submit a manuscript: Please consult the **aim and scope** of the journal at: https://jams.hsu.ac.ir/journal/aim_scope

Guide for Authors is available at: https://jams.hsu.ac.ir/journal/authors.note

To **submit** your paper, please visit: https://jams.hsu.ac.ir/author

https://doi.org/10.22034/jams.2025.210149
J. Appl. Mater. Sci., **2025**, *1*, 210149.
© 2025 *J. Appl. Mater. Sci.* This material is licensed under a Creative Commons Attribution 4.0 International License.

Comparison of the Corrosion Inhibition Effect of *Portulaca oleracea* Extracts Prepared Using Ethanol and Water

Sara Shiri *

Department of Chemical Engineering, Faculty of Engineering, University of Garmsar, Garmsar, Iran

Editor's note: Corrosion inhibition through sustainable coatings based on plant extracts has garnered significant research interest in recent years, paving the way for the development of next-generation corrosion protection systems. In this study, Shiri developed a new class of sustainable coating for mild steel using extracts from *Portulaca oleracea*, prepared with two solvents: ethanol and water. The results indicate that the choice of solvent significantly influences the corrosion inhibition efficiency of the resulting inhibitor, highlighting more effective methods for creating sustainable corrosion protection systems.

doi: 10.22034/jams.2025.210150

How to cite: S. Shiri. *Journal of Applied Material Science*, **2025**, *1*, 210150.

JOURNAL OF
APPLIED
MATERIAL
SCIENCE
jams.hsu.ac.ir

© 2025 *J. Appl. Mater. Sci.*This material is licensed under a Creative Commons Attribution 4.0 International License.

Journal of Applied Material Science **2025**, *1*, 210150
How to cite: S. Shiri, *Journal of Applied Material Science*, **2025**, *1*, 210150.
Journal homepage: **jams.hsu.ac.ir**

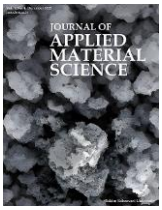

Communication

Comparison of the Corrosion Inhibition Effect of *Portulaca oleracea* Extracts Prepared Using Ethanol and Water

Sara Shiri *

Department of Chemical Engineering, Faculty of Engineering, University of Garmsar, Garmsar, Iran

Abstract

The most important problem that threatens metal structures is corrosion. Corrosion is a slow process, although it is very fast in environments such as industrial estates or the ocean. This phenomenon causes huge environmental pollution. Many chemical corrosion inhibitors are very toxic, but they are still used. Therefore, researchers are looking for green inhibitors, many of which are prepared from plant extracts. In this study, *Portulaca oleracea* extracts were prepared using two solvents (ethanol and water), and their corrosion inhibition potential on mild steel (MS) in salt solution was evaluated. For this purpose, electrochemical impedance spectroscopy (EIS) was used for electrochemical tests. The results showed that the role of the solvent is effective in preparing the extract, and ethanol is a more suitable solvent for preparing the inhibitor from *Portulaca oleracea*. Also, the extract prepared with ethanol showed an inhibition efficiency of 64%. According to the results of this study, it can be said that this extract can be investigated in protective coatings.

Keywords: Green chemistry; Plants; Corrosion Protection.

1. Introduction

Coating is one of the main methods of corrosion protection. Polymer coatings are one of the main classes of coatings widely explored for different corrosion protection applications [1-3]. Although properties and performance of polymers can be improved via nanomaterials and nanostructure [4-7], the unsustainable nature of polymeric coatings is the main reason for the growing interest in nature-based chemical inhibitors. In recent years, due to the toxicity of common chemical inhibitors, the use of plant extracts as green alternatives has received considerable attention, and researchers have conducted numerous studies [8-10].

The results of some studies have shown that inhibitors with an inhibition efficiency of up to 99% can be obtained from some plants [11, 12]. In general, all different parts of a plant can be used to prepare inhibitors, but the inhibition efficiency directly depends on the active phytochemical compounds of the plant, so inhibitors prepared from different parts of a plant will have different inhibition efficiencies [13-15]. Typically, a solvent is used to extract the active phytochemicals from a plant [16]. The solvent can penetrate the plant tissue and thus extract the desired compounds [17]. *Portulaca*

* Corresponding author.
Email address: sarashiri.chem.eng@gmail.com (S. Shiri)

Received 4 August 2025
Revised 1 September 2025
Accepted 1 September 2025
Available online 2 September 2025

https://doi.org/10.22034/jams.2025.210150
© 2025 The Authors. This article is licensed under a Creative Commons Attribution 4.0 International License.

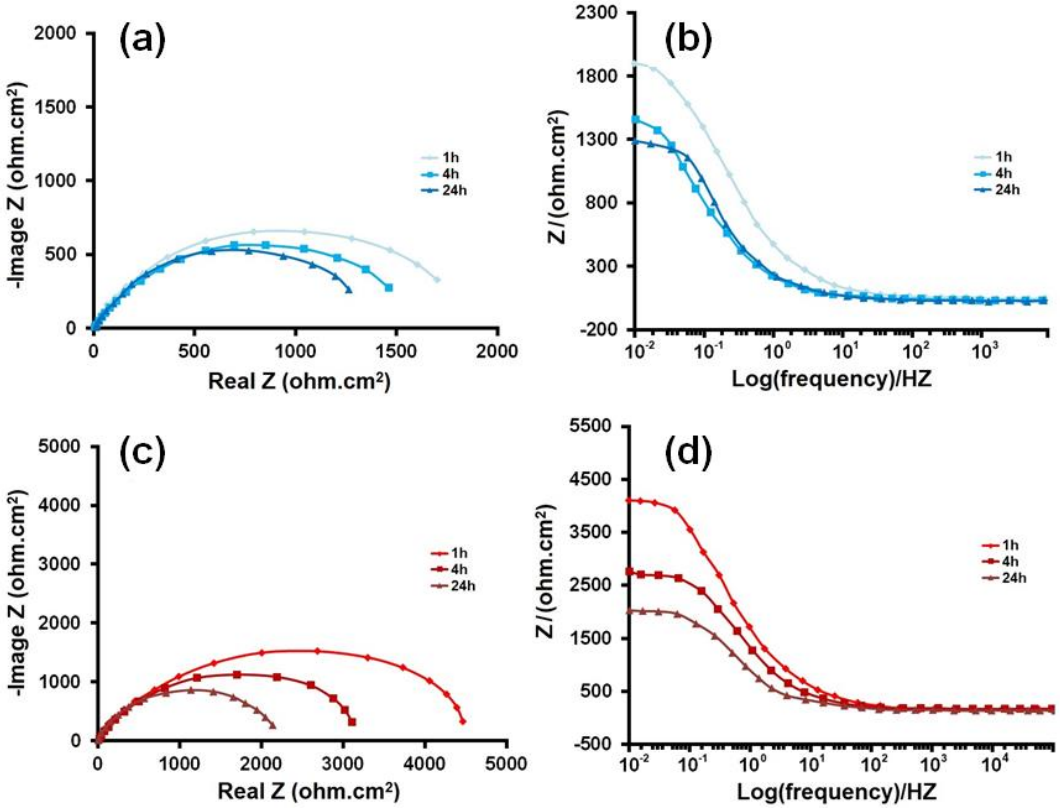

Figure 1. Nyquist and Bode plots of MS at different immersion times (a and b), and in the presence of the *Portulaca oleracea* extract prepared using ethanol (c and d).

oleracea is a herbaceous plant that originally belonged to India but is now spread to various parts of the world [18]. This plant is rich in nutrients, including polysaccharides, which have numerous applications, making it a popular vegetable [19]. In this study, *Portulaca oleracea* was extracted using water and ethanol, and its inhibition efficiency was evaluated.

2. Experimental

2.1. Materials

Sodium chloride (NaCl) and MS were obtained from Merck and Mobarakeh Steel Company, respectively. The *Portulaca oleracea* plant was obtained from a local market (Lahijan city, a region in northern Iran).

2.2. Preparation of extract, MS substrate, and electrochemical tests

First, the *Portulaca oleracea* leaves were washed with distilled water. Then, ethanol was added to the *Portulaca oleracea*, and the extract was prepared after 20 min of heating (at 50 °C). To prepare the extract using water, the same procedure as before was repeated. Substrates and electrochemical tests were performed as reported in a previous paper [20].

3. Results and discussion

The evaluation results are reported in Figure 1 and Table 1. The changes in the diameter of the Nyquist plots (see Figure 1a) indicate the degradation of the MS in the absence of the extract. The diameter of the curve represents the charge transfer resistance (R_{ct}), which is seen to decrease with increasing immersion time. It can be said that with increasing immersion time, the corrosive species will have the time to penetrate the MS and cause its degradation. Also, the Bode plots (see Figure 1b) show a decreasing trend with increasing immersion time. But, the evaluation results in the presence of extract are very different (see Figures 1c-d and Figure 2a-b). As can be seen, we see an increase in the R_{ct} value. Also, the Bode plots show a significant

© 2025 The Authors. This article is licensed under a Creative Commons Attribution 4.0 International License.

Table 1. Electrochemical parameters obtained from EIS results

Samples	Time (h)	R_{ct}(a) (ohm.cm²)	R_s (ohm.cm²)	log |z| (ohm.cm²)	η (%)
Without extract	1	1701.18	7	1900.27	-
	4	1461.28	7.8	1456.86	-
	24	1264.23	7.5	1288.16	-
Extract prepared *via* ethanol	1	4680.59	12	4497.43	64
	4	3348.66	14	2963.91	56
	24	2298.42	13	2229.97	45
Extract prepared *via* water	1	4463.56	12	4105.31	62
	4	3108.61	14	2763.91	53
	24	2133.62	13	2029.97	40

increase in the presence of the extract, which is due to the surface passivation of the MS surface by the functional groups of the extract [20-22].

As mentioned earlier, in this manuscript, two solvents (ethanol and water) were used to prepare the extract. It can be said that the most important factor that affects the quality of the extract is the solvent [13, 23, 24]. In fact, the solvent penetrates the plant and extracts the active compounds. It has been reported in the literature that ethanol can extract alkaloids, flavonols, polyacetylenes, polyphenols, propolis, sterols, tannins, and terpenoids, and water can extract anthocyanins, lectins, polypeptides, saponins, starches, tannins, and terpenoids [13, 20]. *Portulaca oleracea* contains malic acid, polysaccharides, alkaloids, flavonols, terpenoids, polyphenols, carotene, and vitamins B, C, and E [18, 19]. Therefore, ethanol is a better solvent for preparing the extract, and as the results show, the inhibition efficiency of the extract prepared with ethanol is higher, indicating that there are more active compounds in the prepared extract.

Figure 2c shows the equivalent circuit that matched the impedance results. Typically, the compounds in the extracts are adsorbed onto the surface. As previously mentioned, *Portulaca oleracea* contains compounds such as flavonoids, polyphenols, and terpenoids. These

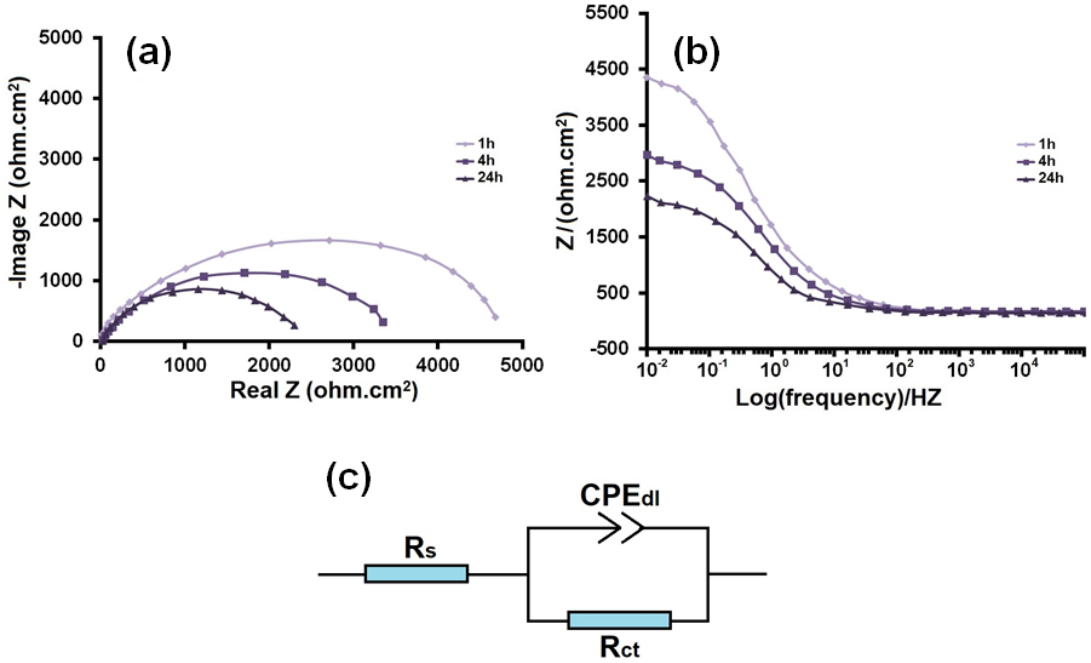

Figure 2. Nyquist and Bode plots of MS at different immersion times in the presence of the extract prepared using water (e and f) and an equivalent circuit to describe the results (c), with Rs representing the solution resistance

© 2025 The Authors. This article is licensed under a Creative Commons Attribution 4.0 International License.

Table 2. Comparison between the highest inhibition efficiency of *Portulaca oleracea* with other plants

Plant	Substrate	Corrosive Medium	Maximum inhibition efficiency (%)	Reference
Date seed	Mild steel	NaCl	71	[10]
Morus alba 'Pendula'	Mild steel	NaCl	61	[20]
Matcha	Mild steel	NaCl	70	[22]
Orange peel	Mild steel	NaCl	94	[23]
Portulaca oleracea	Mild steel	NaCl	64	This study

compounds can adsorb onto the metal surface. This adsorption is related to the π-electron transfer between oxygen atoms and aromatic rings of compounds with vacant *d*-orbitals on the surface, which block the anodic regions and form a protective layer [20-22]. Also, Table 2 presents a comparison between the highest inhibition efficiency in this study and the results of several other studies.

4. Conclusions

In summary, a corrosion inhibitor was prepared from *Portulaca oleracea* using two solvents (ethanol and water). The results showed that this extract has the ability to inhibit corrosion. Also, considering the compounds of this plant, ethanol is a more suitable solvent for preparing the inhibitor. In general, inhibitors prepared from plants are very popular due to their non-toxicity and cheapness, but their effectiveness is of great importance with temperature changes and increasing immersion time. Normally, many active compounds are degraded with increasing temperature, so this aspect of research is very important.

Conflict of Interest

The authors declare no conflict of interest.

References

1. N.N. Xia, et al. Self-passivation/self-delivery/self-healing anticorrosion polymer coating for marine applications. *Journal of Colloid and Interface Science*, **2025**, *678*, 494.
2. L. Meng, et al. All-in-one in-situ constructed neutral inhibitors entrapped polyaniline fibers enable robust anti-corrosion polymer coatings. *Progress in Organic Coatings*, **2025**, *208*, 109463.
3. M. Sheydaei. Sodium sulfide-based polysulfide polymers: synthesis, cure, thermal and mechanical properties. *Journal of Sulfur Chemistry*, **2022**, *43*, 643.
4. F. Mahdavian, et al. Flexible Polymer Hydrogels for Wearable Energy Storage Applications. *Advanced Materials Technologies*, **2023**, *8*, 2202199.
5. Z. Jarrahi, S. Ghorbanzadeh, and A. Allahbakhsh, *Hydrogels-based Nanostructured Materials for Energy Generation, Conversion, and Storage Applications*, in *Materials for Energy Production, Conversion, and Storage*. **2024**, CRC Press. p. 301.
6. M. Khalaj, et al. Structural, mechanical and thermal behaviors of novolac/graphene oxide nanocomposite aerogels. *Journal of Non-Crystalline Solids*, **2017**, *460*, 19.
7. M. Sheydaei, M. Edraki, and S.M. Radeghi Mehrjou. Anticorrosion and Antimicrobial Evaluation of Sol-Gel Hybrid Coatings Containing Clitoria ternatea Modified Clay. *Gels*, **2023**, *9*, 490.
8. M. Sheydaei. Investigation of Heavy Metals Pollution and Their Removal Methods: A Review. *Geomicrobiology Journal*, **2024**, *41*, 213.
9. M. Lavanya, J. Ghosal, and P. Rao. A comprehensive review of corrosion inhibition of aluminium alloys by green inhibitors. *Canadian Metallurgical Quarterly*, **2023**, *63*, 119.
10. M. Edraki and M. Sheydaei. Investigation of date seed powder as green corrosion inhibitor for mild steel: A study of solution and coating phases. *Hybrid Advances*, **2024**, *6*, 100238.
11. H. Li, S. Zhang, and Y. Qiang. Corrosion retardation effect of a green cauliflower extract on copper in H2SO4 solution: Electrochemical and theoretical explorations. *Journal of Molecular Liquids*, **2021**, *321*, 114450.
12. Q. Liu, et al. A novel green reinforcement corrosion inhibitor extracted from waste Platanus acerifolia leaves. *Construction and Building Materials*, **2020**, *260*, 119695.
13. M. Sheydaei. The Use of Plant Extracts as Green Corrosion Inhibitors: A Review. *Surfaces*, **2024**, *7*, 380.
14. E. Milad, et al. Protective Nanocomposite Coating Based on Ginger Modified Clay and Polyurethane: Preparation, Characterization and Evaluation Anti-Corrosion and Mechanical Properties. *Polymer Science, Series B*, **2022**, *64*, 756.

© 2025 The Authors. This article is licensed under a Creative Commons Attribution 4.0 International License.

15. M. Edraki, et al. Enhanced mechanical, anticorrosion and antimicrobial properties of epoxy coating via pine pollen modified clay incorporation. *Iranian Journal of Chemistry and Chemical Engineering*, **2023**, *42*, 2775.

16. M. Kalaskar, et al., *Methods of Extraction*, in *Pharmacognosy and Phytochemistry*. **2025**, Wiley. p. 121.

17. S. Hlatshwayo, et al. Extraction and Processing of Bioactive Phytoconstituents from Widely Used South African Medicinal Plants for the Preparation of Effective Traditional Herbal Medicine Products: A Narrative Review. *Plants*, **2025**, *14*, 206.

18. Z. Mzoughi and H. Majdoub. Pectic polysaccharides from edible halophytes: Insight on extraction processes, structural characterizations and immunomodulatory potentials. *International Journal of Biological Macromolecules*, **2021**, *173*, 554.

19. M. Wang, et al. Extraction, Purification, Structural Characteristics, Biological Activity and Application of Polysaccharides from Portulaca oleracea L. (Purslane): A Review. *Molecules*, **2023**, *28*, 4813.

20. S. Shiri. Exploring Corrosion Protection Potential of Sustainable and Green Morus alba 'Pendula' Fruit Extracts. *Journal of Applied Material Science*, **2025**, *1*, 210139.

21. M. Edraki and M. Sheydaei. Investigation of the Dual Active/Barrier Corrosion Protection, Mechanical and Thermal Properties of a Vinyl Ester Coating Doped with Ginger Modified Clay Nanoparticles. *Russian Journal of Applied Chemistry*, **2022**, *95*, 1481.

22. M. Sheydaei, M. Edraki, and F.S.-J. Abad. Matcha-modified clay polyurethane coating: improving thermal, mechanical, antimicrobial, and anticorrosion performance. *Iranian Polymer Journal*, **2023**, *32*, 1643.

23. M. Sheydaei and M. Edraki. Orange Peel-impregnated Sodium Montmorillonite as a Sustainable Corrosion Inhibitor for Mild Steel. *Journal of Applied Material Science*, **2025**, *1*, 210136.

24. S. Milad, M. Edraki, and S. Javanbakht. Ganoderma Lucidum-Modified Clay Epoxy Coating: Investigation of Thermal, Mechanical, Anticorrosion, and Antimicrobial Properties. *Polymer Science, Series B*, **2023**, *65*, 991.

© 2025 The Authors. This article is licensed under a Creative Commons Attribution 4.0 BY International License.

© 2025 The Authors. This article is licensed under a Creative Commons Attribution 4.0 International License.

Synthesis and Characterization of Polyethylene Glycol Coated Superparamagnetic Fe_3O_4 Nanoparticles

Priyanka A. Patil *, Shanabhau D. Bagul, Nitesh S. Koche

Nanomaterials Research Laboratory, Department of Physics, Pratap College Amalner, Maharashtra, India

Editor's note: Superparamagnetic nanoparticles have significant potential for innovative applications across various fields, including material science and engineering, biomedicine, biotechnology, and environmental science. Patil et al. reported that coating iron oxide (Fe_3O_4) nanoparticles with polyethylene glycol enhances the performance of these superparamagnetic nanoparticles. The synthesized magnetite Fe_3O_4 nanoparticles exhibited a cubic inverse spinel structure, had a roughly spherical shape, and were monodispersed. Additionally, Vibrating Sample Magnetometer results demonstrated excellent superparamagnetic behavior and high saturation magnetization at room temperature.

doi: 10.22034/jams.2025.210151

How to cite: P.A. Patil et al. *Journal of Applied Material Science*, **2025**, *1*, 210151.

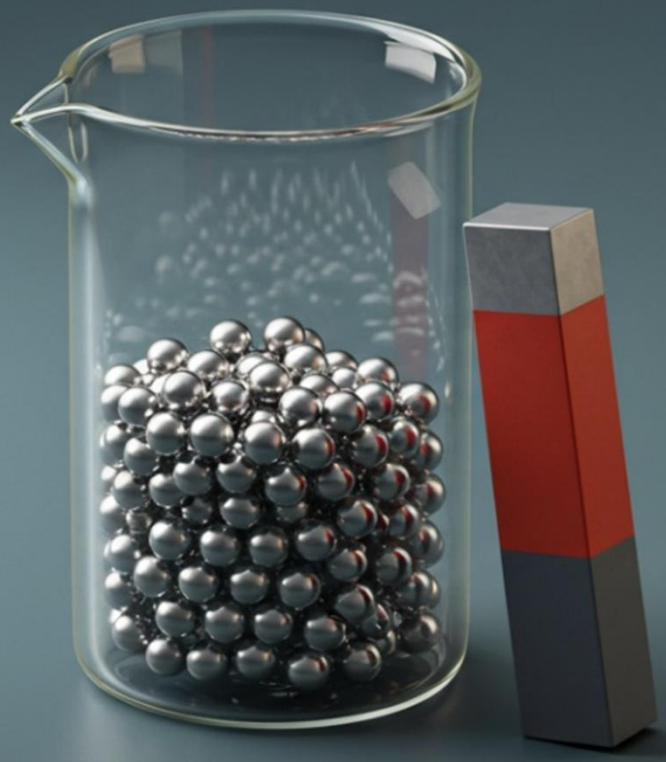

JOURNAL OF
APPLIED
MATERIAL
SCIENCE
jams.hsu.ac.ir

© 2025 *J. Appl. Mater. Sci.*This material is licensed under a Creative Commons Attribution 4.0 International License.

Journal of Applied Material Science **2025**, *1*, 210151
How to cite: P.A. Patil et al., *Journal of Applied Material Science*, **2025**, *1*, 210151.
Journal homepage: **jams.hsu.ac.ir**

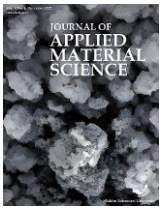

Original Research

Synthesis and Characterization of Polyethylene Glycol Coated Superparamagnetic Fe_3O_4 Nanoparticles

Priyanka A. Patil *, Shanabhau D. Bagul, Nitesh S. Koche

Nanomaterials Research Laboratory, Department of Physics, Pratap College Amalner, Maharashtra, India

Abstract

The purpose of the present study is to synthesize polyethylene glycol (PEG) coated superparamagnetic iron oxide (Fe_3O_4) nanoparticles using a non-toxic, low-temperature, and cost-effective sol-gel method. $Fe(NO_3)_3.9H_2O$ is used as the iron precursor, ethanol as the solvent, and non-toxic triethylamine (TEA) as the gelation agent. Reactions are carried out at a low synthesis temperature of 60°C. The X-ray diffraction (XRD) pattern of the synthesized powder confirmed the magnetite (Fe_3O_4) phase of iron oxide with a cubic inverse spinel structure. Field emission scanning electron microscopy (FE-SEM) results confirmed that the resulting Fe_3O_4 nanoparticles were roughly spherical in shape and monodisperse in nature. Fourier transform infrared spectroscopy (FTIR) results confirmed that the surface of Fe_3O_4 nanoparticles was coated with PEG through carbonyl groups. FTIR results also showed that the intensity of the band related to the coated powder increased with an increase in the concentration of PEG. The quantitative elemental analysis was done by energy-dispersive X-ray spectroscopy (EDAX). Thermo-gravimetric analysis (TGA) confirmed the presence of PEG in the structure of Fe_3O_4 nanoparticles. Results of the vibrating sample magnetometer (VSM) showed that the obtained Fe_3O_4 nanoparticles exhibit excellent superparamagnetic behavior with high saturation magnetization at room temperature. Such superparamagnetic Fe_3O_4 nanoparticles with a favorable size are promising candidates for biomedical applications.

Keywords: Fe_3O_4 nanoparticles; PEG coating; Superparamagnetic; FTIR; VSM.

1. Introduction

In recent years, nanoscience and nanotechnology have reached great heights to such an extent that it is easy to synthesize, characterize, and control the functional properties of nanomaterials. Nanomaterials possess a great scientific interest because of their outstanding, unique, and beneficial properties [1-4]. Nowadays, considerable attention has been focused on the magnetic iron oxide nanoparticles (MIONPs) because of their unique properties, such as superparamagnetic, biocompatibility, non-toxicity, etc. They therefore found widespread applications in various disciplines such as material science and engineering, biomedicine, biotechnology, and environmental science.

MIONPs have become a promising candidate for biomedical applications, which include detection and

* Corresponding author.
Email address: priyapatil2186@gmail.com (P.A. Patil)

Received 16 August 2025
Revised 6 September 2025
Accepted 11 September 2025
Available online 14 September 2025

https://doi.org/10.22034/jams.2025.210151
© 2025 The Authors. This article is licensed under a Creative Commons Attribution 4.0 International License.

bioseparation of biological entities, magnetic resonance imaging (MRI), Drug delivery systems (DDS), and hyperthermia [5-9]. Several experiments have been carried out on iron oxides, which include Fe_3O_4 (Magnetite), γ-Fe_2O_3 (Maghemite), α-Fe_2O_3 (Hematite), β-Fe_2O_3, ε-Fe_2O_3, and FeO. Out of these, magnetite and maghemite are the promising candidates for biomedical applications [10].

However, because of the hydrophobic surface and large surface area to volume ratio, MIONPs possess high surface energy, which tends to agglomerate and form large clusters. In order to avoid agglomeration and cluster formation, a suitable coating should be applied on the surface of the MIONPs. Organic polymers, as well as inorganic materials (gold, silica, etc.), are used as coating materials. Polyethylene glycol (PEG) is widely used as a coating material because: (i) it improves the biocompatibility, (ii) it is non-antigenic, (iii) it is non-immunogenic, and (iv) it is water soluble [11-14].

PEG-coated MIONPs can be obtained by many synthesis techniques, such as coprecipitation [15], hydrothermal synthesis [16], electrochemical deposition [17], and thermal decomposition [18]. Among all of these methods, the sol-gel method is widely used because it possesses several advantages such as: (i) it is very simple and cost effective, (ii) it takes place at low temperature, (iii) it controls the stoichiometry of the resultant product, (vi) homogeneous growth of particles with uniform size distribution [19, 20].

In the present study, a two-step synthesis route was used to obtain PEG-coated MIONPs. In the first step, the MIONPs were synthesized, and in the second step, the MIONPs were coated using different amounts of PEG. Characterizations of PEG-coated MIONPs were made by X-ray diffraction (XRD), field emission scanning electron microscopy (FE-SEM), Fourier transform infrared spectroscopy (FT-IR), energy dispersive analysis by X-rays (EDAX), thermogravimetric analysis (TGA), and vibrating sample magnetometry (VSM).

It was observed that the nanoparticles were successfully coated, and magnetic characterization of the nanoparticles showed that the saturation magnetization (Ms) of PEG-coated MIONPs was higher than the Ms value of reported PEG-coated MIONPs [21, 22]. An enhancement of Ms may make a contribution to the properties of PEG-coated MIONPs and offer improved control over the delivery of nanoparticles for potential applications.

2. Experimental

2.1. Materials

Chemicals used to synthesize Fe_3O_4 nanoparticles were Ferric nitrate ($Fe(NO_3)_3.9H_2O$), ethanol, and triethylamine (TEA). Polyethylene glycol (PEG-6000) was used to coat the surface of Fe_3O_4 nanoparticles so as to make them biocompatible. All chemicals used were from Merk Co. and of AR grade.

2.2. Synthesis of MIONPs

Ferric nitrate (10.4 mg) was dissolved in 10 ml of ethanol. The solution is stirred under a permanent magnetic stirrer at 350-400 rpm to ensure complete dissolution of the ferric nitrate in ethanol. The temperature of the solution was maintained at 60 °C using a water bath. After complete dissolution, the solution of orange color was obtained. Subsequently, 1.5 ml of TEA was added dropwise to the solution. The color of the solution rapidly changed from orange to reddish brown, accompanied by appreciable heat release, and the gel was formed. The gel was then completely dried. The dried gel was calcined at 300 °C in an air atmosphere to obtain MIONPs. The powder so prepared was referred to as S-1.

2.3. Coating of iron oxide nanoparticles with PEG-6000

For coating MIONPs, PEG solutions with different concentrations were prepared by dissolving PEG-6000 flakes in distilled water. MIONPs were added and mixed with the PEG-6000 solution for 3 hours. The coated particles were dried under an IR lamp. Following the above procedure, four sets of samples were prepared by varying the concentration (5%, 10%, 20% and 30% by weight) of PEG and were respectively referred to as S-5, S-10, S-20, and S-30.

2.4. Measurements

The structural characterization of PEG-coated and uncoated Fe_3O_4 nanoparticles was carried out using an X-ray diffractometer (Miniflex 600, Rigaku) with CuKα1 radiation (λ=1.5406 Å). Morphological study of the Fe_3O_4 nanoparticles was performed using field emission scanning electron microscopy (FESEM model S4800 type II, Hitachi High Technologies). Quantitative analysis of the Fe_3O_4 nanoparticles was carried out using EDAX analysis of the FESEM equipment (model Bruker Nano

© 2025 The Authors. This article is licensed under a Creative Commons Attribution 4.0 International License.

GmbH X Flash Detector 5030). Fourier transform infrared spectroscopy (FTIR) of Fe_3O_4 nanoparticles was recorded using Spectrum BX (Perkin Elmer) in the range of 600-4000 cm^{-1}. Thermogravimetric analysis (TGA) study of Fe_3O_4 nanoparticles was done by STA-6000 (Perkin Elmer) in the temperature range 50-800 °C under nitrogen atmosphere. Magnetic properties of Fe_3O_4 nanoparticles were carried out at room temperature using a vibrating sample magnetometer (VSM EZ9; Microsense Inc., USA).

3. Results and discussion

3.1. X-ray Diffraction (XRD) studies

Figure 1 shows the XRD patterns of (a) uncoated and (b) PEG-coated Fe_3O_4 nanoparticles. The XRD patterns in Figure 1 (a) and Figure 1 (b) confirmed the nanoparticles to be magnetite (Fe_3O_4) phase of iron oxide (ICDD Card No. 01-080-6410) with a cubic inverse spinel structure. The average crystallite size of Fe_3O_4 nanoparticles was determined using Scherrer's formula $t=0.94\lambda/B\cos\theta$, where λ is the wavelength (CuKα1 radiation $\lambda=1.5406$Å), B is the full width at half maximum in radians, and θ is the diffraction angle of the peak [23]. The most prominent peak at $\theta=35.6°$ was chosen to calculate the average crystallite size. The estimated average size of the Fe_3O_4 nanoparticles was found to be 16.2nm.

3.2. Field Emission Scanning Electron Microscopy (FESEM) and EDAX

Figure 2 (a) and (b) indicate the FESEM images of uncoated and PEG-coated Fe_3O_4 nanoparticles. These figures reveal that the synthesized Fe_3O_4 nanoparticles are approximately spherical in shape. The uncoated Fe_3O_4 nanoparticles are agglomerated due to magneto-dipole interactions between the Fe_3O_4 nanoparticles. After the coating of PEG on the surfaces of Fe_3O_4 nanoparticles, the agglomeration of nanoparticles is observed to be minimized [24]. Image blurring in the case of coated Fe_3O_4 nanoparticles may be due to the film formation [25]. The surface of the PEG-coated Fe_3O_4 nanoparticles seems to be rougher due to the polymerization occurring on the surface of the nanoparticles and strong interfacial interaction between the polymer and Fe_3O_4 nanoparticles [26].

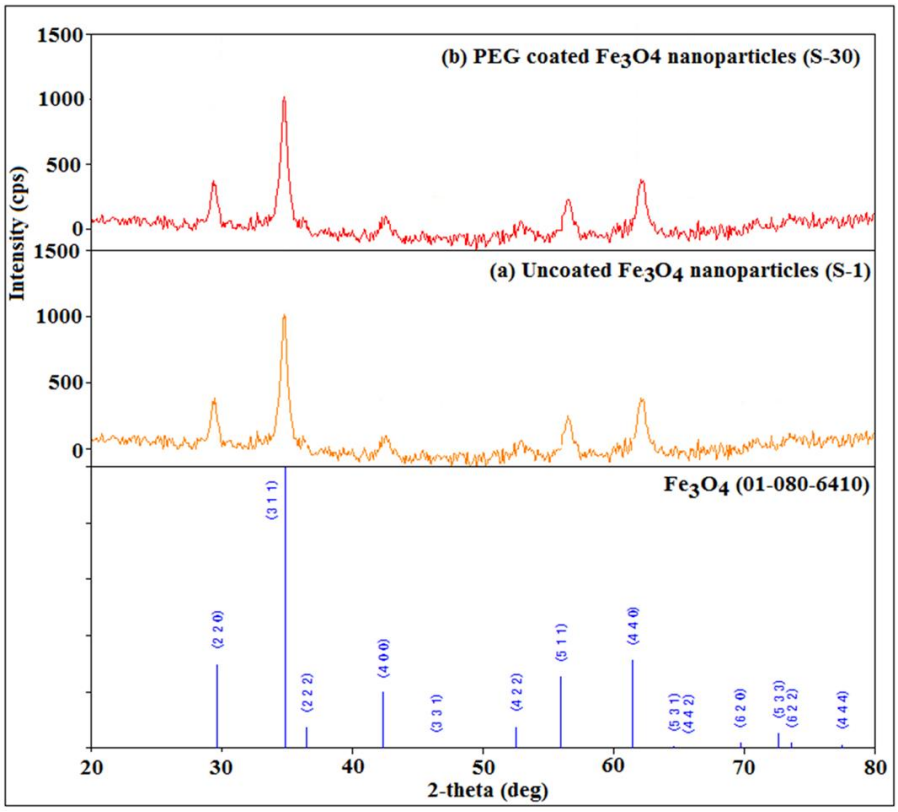

Figure 1. XRD Patterns of (a) uncoated Fe_3O_4 nanoparticles (S-1) and (b) PEG-coated Fe_3O_4 nanoparticles (S-30).

© 2025 The Authors. This article is licensed under a Creative Commons Attribution 4.0 International License.

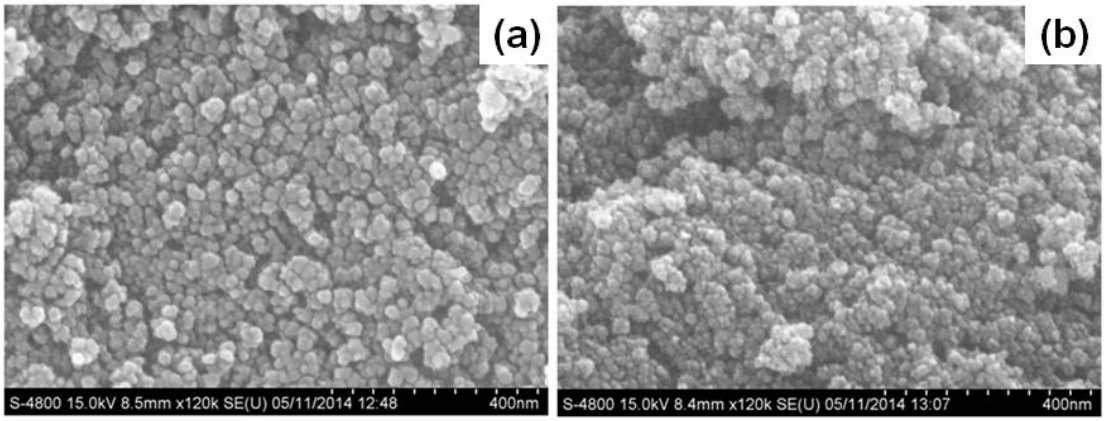

Figure 2. FESEM images of (a) uncoated Fe_3O_4 nanoparticles (S-1) and (b) PEG-coated Fe_3O_4 nanoparticles (S-30).

Figure 3 (a) and (b) present EDAX spectra of uncoated and PEG-coated Fe_3O_4 nanocrystalline powders. The spectrum in Figure 3 (a) consists of two peaks related to Fe and O, while Figure 3 (b) includes three peaks related to Fe, O, and C. The peak corresponding to C in Figure 3 (b) may be due to the existence of PEG on the surface of Fe_3O_4 nanoparticles. The EDAX technique is unable to detect light elements like H. Therefore, the peak corresponding to H may be absent [27, 28].

3.3. Thermo Gravimetric Analysis (TGA)

Curves (a), (b), and (c) in Figure 4 show TGA curves of pure PEG-6000 flakes, uncoated and PEG-coated iron oxide nanocrystalline powder, respectively. It is clear from curve (a) in Figure 4 that there was a weight loss of 2.9% during 50 °C to 340 °C and a weight loss of 95.3% during 340 °C to 420 °C. The PEG was observed to be completely decomposed at 420 °C. In Figure 4, the curve (b) corresponds to the uncoated Fe_3O_4 nanoparticles, which were almost stable, and the weight loss of only 2.4% was seen. This showed that the powder was thermodynamically stable. Curve (c) shows the weight loss of 1.1% in the temperature range 50 °C to 230 °C. But a continuous weight loss of 17.3% was observed in the temperature range of 230 °C to 390 °C. The weight loss may be due to the decomposition of PEG on the surface of Fe_3O_4 nanoparticles. At 390 °C, PEG was completely decomposed, and only Fe_3O_4 nanoparticles remained. The decomposition temperature of PEG was shifted from 420 °C to 390 °C as indicated in curve (c). It may be because of a change in the chemical environment and oxidative degradation reactions, which can lower the decomposition temperature [29].

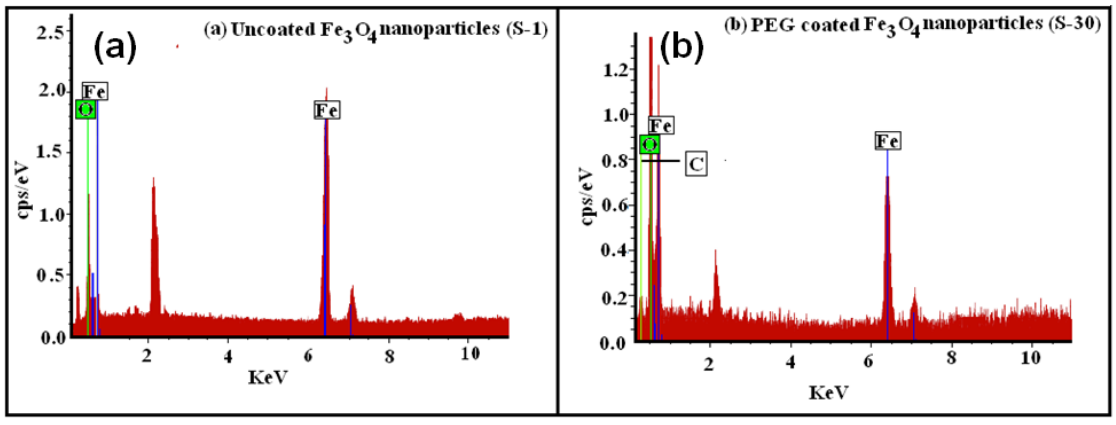

Figure 3. EDAX spectra of (a) uncoated Fe_3O_4 nanoparticles (S-1) and (b) PEG-coated Fe_3O_4 nanoparticles (S-30).

© 2025 The Authors. This article is licensed under a Creative Commons Attribution 4.0 International License.

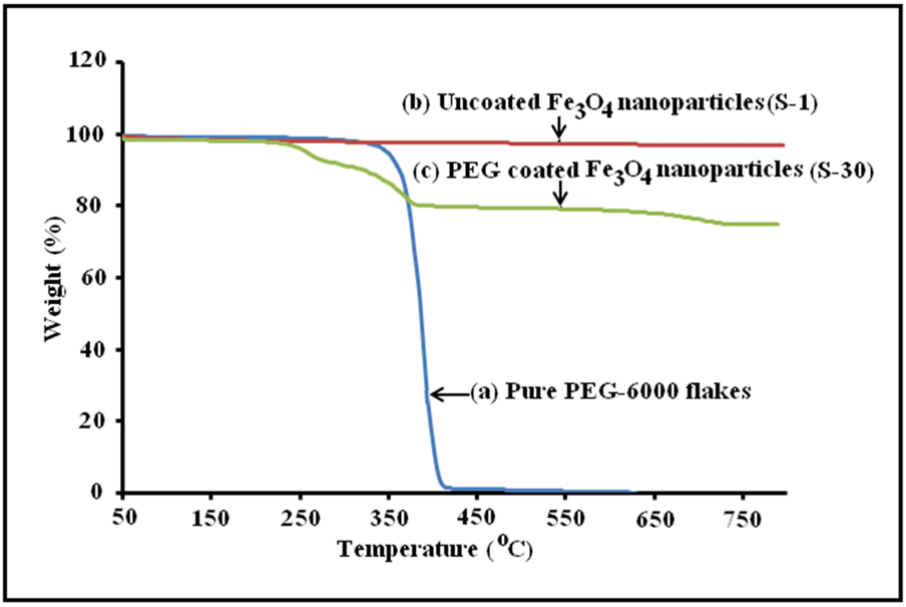

Figure 4. TGA curves of: (a) pure PEG-6000 flakes, (b) uncoated Fe_3O_4 nanoparticles (S-1), and (c) PEG-coated Fe_3O_4 nanoparticles (S-30).

3.4. Fourier Transform Infrared Spectroscopy (FT-IR)

Curves (a), (b), and (c) in Figure 5 show the FT-IR spectrum of uncoated Fe_3O_4 nanoparticles, PEG-6000-coated Fe_3O_4 nanoparticles, and pure PEG-6000 flakes, respectively. The peak at 2883.88 cm^{-1} may be attributed to the symmetric stretching of the CH_2 group [27, 30]. The absorption peak observed at 2359.65 cm^{-1} may be due to the absorption of atmospheric CO_2 on the metallic cations [31, 32]. The absorption peak observed around 1466.01 cm^{-1} in curves in Figure 5 (b) may be caused by the bending vibration of the C-H bond of the CH_2 group. The absorption peaks at 1359.33, 1340.45, 1278.27, 1240.05, 1142.75, 1100.65, 1060.03 cm^{-1} in curves (b) and (c) may result from the bending vibration of the O-H bond and stretching vibration of the C-O bond of the –CH_2-OH group [33, 34].

The strong absorption peak at 1100.41 cm^{-1} in curve (b) and 1100.65 cm^{-1} in curve (c) may be attributed to the –CH_2-O-CH_2- group of PEG-6000. The presence of CH_2-O-CH_2, -CH_2, and –CH peaks in the spectrum of coated

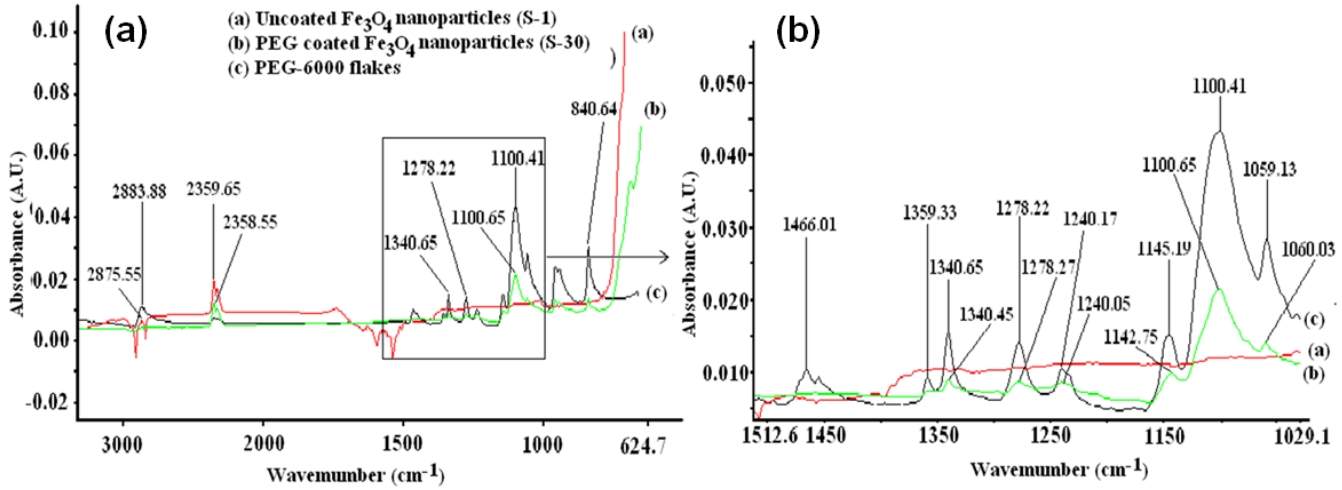

Figure 5. FT-IR spectra (a) and results in a selected wavenumber area (b) of uncoated Fe_3O_4 nanoparticles (S-1, curve a), PEG-coated Fe_3O_4 nanoparticles (S-30, curve b), and pure PEG-6000 (curve c).

© 2025 The Authors. This article is licensed under a Creative Commons Attribution 4.0 International License.

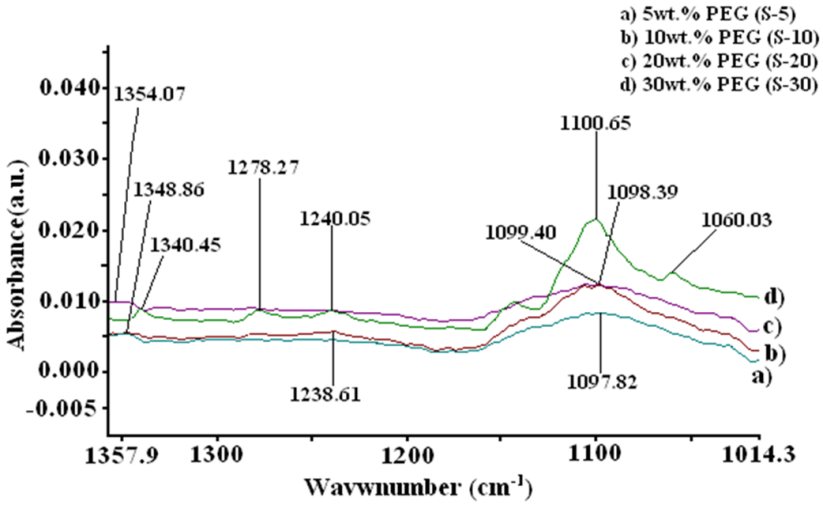

Figure 6. FT-IR spectra of Fe3O4 nanoparticles coated with (5-30wt %) of PEG.

powder, as shown in Figure 5 (b), may be due to PEG-6000 covering on the surface of Fe_3O_4 nanoparticles. The above results suggest that the nanoparticles associated with iron oxide powder were successfully coated by PEG [35].

Curves (a), (b), (c), and (d) in Figure 6 represent FT-IR spectra of Fe_3O_4 nanoparticles coated with 5 wt% %, 10wt %, 20wt%, and 30wt% PEG, respectively. The FT-IR spectra consist of strong and well-defined bands around 1100 cm^{-1}. It is clear from **Fig. 6**(a-d) that the height of the absorption peak (1100 cm^{-1}) increases with the increase of PEG content. It may be due to a larger quantity of hydroxyl group ($–CH_2$-O-CH_2-) bonding to the Fe_3O_4 nanoparticles [36].

3.5. Magnetization

Figure 7 (a) and (b) show the simple laboratory experiment with a bar magnet to demonstrate the magnetic nature of the Fe_3O_4 nanoparticles using a bar magnet. In the absence of a bar magnet, Fe_3O_4

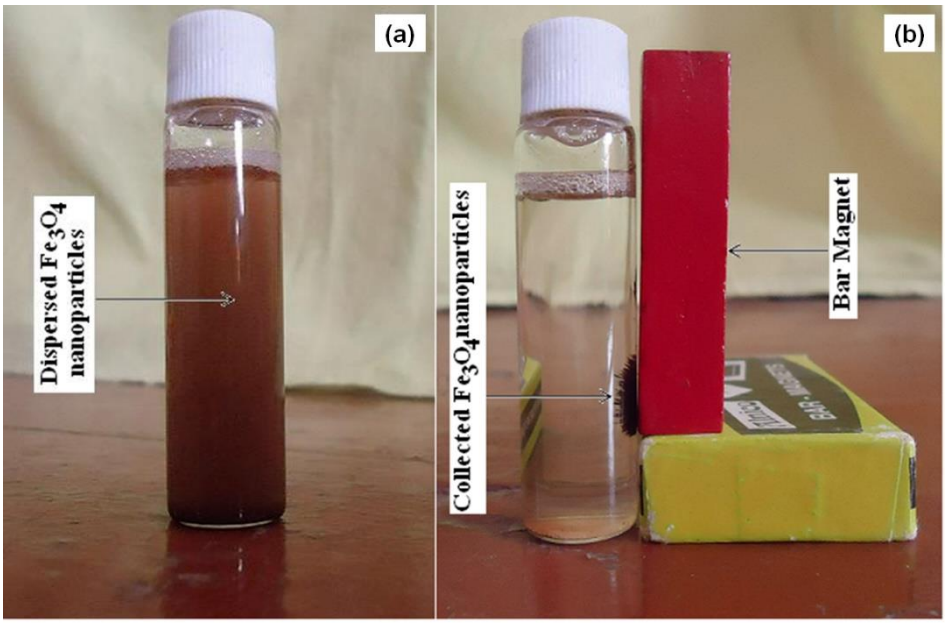

Figure 7. (a) Dispersed nanoparticles in the absence of a bar magnet and (b) collection of nanoparticles in the presence of a bar magnet.

© 2025 The Authors. This article is licensed under a Creative Commons Attribution 4.0 International License.

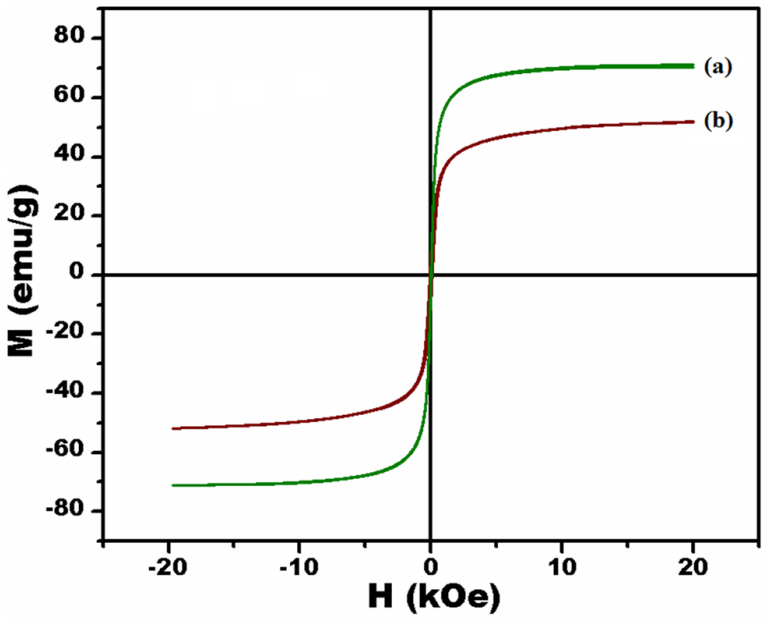

Figure 8. Magnetization curves for (a) Fe_3O_4 nanoparticles (S-1) and (b) PEG-coated Fe_3O_4 nanoparticles (S-30).

nanoparticles were observed to be dispersed uniformly in solution, as indicated in Figure 7 (a). In the presence of a bar magnet, Fe_3O_4 nanoparticles were observed to be collected toward the bar magnet as shown in Figure 7(b). Due to their magnetic nature, Fe_3O_4 nanoparticles were observed to gather near the magnet [28, 37, 38].

The magnetic properties of uncoated and PEG-coated Fe_3O_4 nanoparticles were studied at room temperature by the vibrating sample magnetometer (VSM), as shown in Figure 8. From Figure 8, it can be seen that the magnetization curves appeared to be S-shaped over the applied field from -20 to +20 kOe. The uncoated and PEG-coated Fe_3O_4 nanoparticles exhibit excellent superparamagnetic behavior with zero coercivity and high saturation magnetization. The saturation magnetization (Ms) for uncoated and PEG-coated Fe_3O_4 nanoparticles was found to be 71 emu/g and 51 emu/g, respectively. The value of saturation magnetization of PEG-coated Fe_3O_4 nanoparticles is lower than that of uncoated Fe_3O_4 nanoparticles. This may be due to the existence of PEG. For biomedical applications, it is required that Fe_3O_4 nanoparticles should be monodisperse in nature, superparamagnetic with high saturation magnetization. Therefore, the PEG-coated Fe_3O_4 nanoparticles may be promising candidates for biomedical applications, such as hyperthermia treatment, magnetic resonance imaging, etc. [39-43].

4. Conclusions

PEG-coated Fe_3O_4 nanoparticles were synthesized by a simple, cost-effective sol-gel method by optimizing experimental conditions. The structural, morphological, and thermal properties of PEG-coated Fe_3O_4 nanoparticles were studied using different techniques. Coating of PEG on the surface of Fe_3O_4 nanoparticles was confirmed by FT-IR spectroscopy. As the concentration of PEG increases, the absorbance also increases. PEG-coated Fe_3O_4 nanoparticles were observed to be superparamagnetic in nature and also exhibit high saturation magnetization. Therefore, the PEG-coated Fe_3O_4 nanoparticles may be promising for biomedical applications.

Acknowledgments

Authors are heartily thankful to Rashtriya Uchchatar Shiksha Abhiyan (RUSA) MHRD, New Delhi, for financial support. The authors would also like to thank the Head of Physics Department and Principal Pratap College, Amalner, Dist: Jalgaon, Maharashtra, for providing laboratory facilities.

© 2025 The Authors. This article is licensed under a Creative Commons Attribution 4.0 International License.

Conflict of Interest

The authors declare no conflict of interest.

References

1. L.S. Ganapathe, et al. Magnetite (Fe3O4) Nanoparticles in Biomedical Application: From Synthesis to Surface Functionalisation. *Magnetochemistry*, 2020, *6*, 68.
2. C. Vincent, et al. Iron Oxide Nanoparticles: Types, Synthesis, Biomedical applications and Scope of Nanoinformatics. *Biological Forum – An International Journal*, **2023**, *15*, 927.
3. M.L. López-Moreno, et al. Environmental behavior of coated NMs: Physicochemical aspects and plant interactions. *Journal of Hazardous Materials*, **2018**, *347*, 196.
4. M.E.A. El-sayed. Nanoadsorbents for water and wastewater remediation. *Science of The Total Environment*, **2020**, *739*, 139903.
5. S. Matsuo, S. Kobayashi, and K. Ono. Magnetization process of concave Fe3O4 nanoparticles. *Journal of Physics and Chemistry of Solids*, **2026**, *208*, 113020.
6. L. Peixoto, et al. Magnetic nanostructures for emerging biomedical applications. *Applied Physics Reviews*, **2020**, *7*, 011310.
7. Y. Yan, et al. Morphology-dependent magnetic hyperthermia characteristics of Fe3O4 nanoparticles. *Materials Chemistry and Physics*, **2025**, *329*, 130045.
8. D.L. Peréz, et al. Synthesis of superparamagnetic iron oxide nanoparticles coated with polyethylene glycol as potential drug carriers for cancer treatment. *Journal of Nanoparticle Research*, **2024**, *26*, 2.
9. J.E. Ogbezode, et al. A narrative review of the synthesis, characterization, and applications of iron oxide nanoparticles. *Discover Nano*, **2023**, *18*, 125.
10. F. Chang and G.-L. Davies. From 0D to 2D: Synthesis and bio-application of anisotropic magnetic iron oxide nanomaterials. *Progress in Materials Science*, **2024**, *144*, 101267.
11. B. Thapa, et al. Enhanced MRI T 2 Relaxivity in Contrast-Probed Anchor-Free PEGylated Iron Oxide Nanoparticles. *Nanoscale Research Letters*, **2017**, *12*, 312.
12. G. Antarnusa and E. Suharyadi. A synthesis of polyethylene glycol (PEG)-coated magnetite Fe₃O₄ nanoparticles and their characteristics for enhancement of biosensor. *Materials Research Express*, **2020**, *7*, 056103.
13. G. Antarnusa, et al. The Effect of Additional Polyethylene Glycol (PEG) as Coating Fe3O4 for Magnetic Nanofluid Applications. *Recent Innovations in Chemical Engineering (Formerly Recent Patents on Chemical Engineering)*, **2021**, *14*, 335.
14. S. Arsalani, et al. Uniform size PEGylated iron oxide nanoparticles as a potential theranostic agent synthesized by a simple optimized coprecipitation route. *Journal of Magnetism and Magnetic Materials*, **2022**, *564*, 170091.
15. C. Ravikumar. Unveiling the formation mechanism of polydisperse iron oxide nanoparticles in coprecipitation route. *Journal of Crystal Growth*, **2023**, *624*, 127419.
16. C. Zhang and I. Zhitomirsky. Hydrothermal synthesis of iron oxides in the presence of catecholate capping agent for supercapacitor electrodes. *Materials Letters*, **2025**, *401*, 139229.
17. I. Karimzadeh, H.R. Dizaji, and M. Aghazadeh. Development of a facile and effective electrochemical strategy for preparation of iron oxides (Fe3O4 and γ-Fe2O3) nanoparticles from aqueous and ethanol mediums and in situ PVC coating of Fe3O4 superparamagnetic nanoparticles for biomedical applications. *Journal of Magnetism and Magnetic Materials*, **2016**, *416*, 81.
18. A. Ullrich, et al. Synthesis of iron oxide nanoparticles by decomposition of iron-oleate: influence of the heating rate on the particle size. *Journal of Nanoparticle Research*, **2022**, *24*, 183.
19. L. Durães, et al. Phase investigation of as-prepared iron oxide/hydroxide produced by sol–gel synthesis. *Materials Letters*, **2005**, *59*, 859.
20. L. Durães, et al. Characterization of iron(III) oxide/hydroxide nanostructured materials produced by sol–gel technology based on the Fe(NO3)3·9H2O–C2H5OH–CH3CHCH2O system. *Materials Chemistry and Physics*, **2011**, *130*, 548.
21. M. Anuje, et al. Synthesis, Characterization, and Cytotoxicity Evaluation of Polyethylene Glycol-Coated Iron Oxide Nanoparticles for Radiotherapy Application. *Journal of Medical Physics*, **2021**, *46*, 154.
22. V. Patsula, et al. Size-dependent magnetic properties of iron oxide nanoparticles. *Journal of Physics and Chemistry of Solids*, **2016**, *88*, 24.
23. A.E. Eken and M. Ozenbas. Characterization of nanostructured magnetite thin films produced by sol–gel processing. *Journal of Sol-Gel Science and Technology*, **2009**, *50*, 321.
24. D.-L. Zhao, et al. Magnetic and inductive heating properties of Fe3O4/polyethylene glycol composite nanoparticles with core–shell structure. *Journal of Alloys and Compounds*, **2010**, *502*, 392.
25. A. Petri-Fink, et al. Effect of cell media on polymer coated superparamagnetic iron oxide nanoparticles (SPIONs): Colloidal stability, cytotoxicity, and cellular uptake studies. *European Journal of Pharmaceutics and Biopharmaceutics*, **2008**, *68*, 129.

© 2025 The Authors. This article is licensed under a Creative Commons Attribution 4.0 International License.

26. H. Gu, et al. Magnetoresistive polyaniline-magnetite nanocomposites with negative dielectrical properties. *Polymer*, **2012**, *53*, 801.

27. A. Mukhopadhyay, et al. A Facile Synthesis of PEG-Coated Magnetite (Fe₃O₄) Nanoparticles and Their Prevention of the Reduction of Cytochrome C. *ACS Applied Materials & Interfaces*, **2011**, *4*, 142.

28. M. Mahdavi, et al. Synthesis, Surface Modification and Characterisation of Biocompatible Magnetic Iron Oxide Nanoparticles for Biomedical Applications. *Molecules*, **2013**, *18*, 7533.

29. K. Król-Morkisz and K. Pielichowska, *Thermal Decomposition of Polymer Nanocomposites With Functionalized Nanoparticles*, in *Polymer Composites with Functionalized Nanoparticles*. **2019**, Elsevier. p. 405.

30. Y.F. Shen, et al. Preparation and application of magnetic Fe3O4 nanoparticles for wastewater purification. *Separation and Purification Technology*, **2009**, *68*, 312.

31. S. Maensiri, et al. Synthesis and optical properties of nanocrystalline V-doped ZnO powders. *Optical Materials*, **2007**, *29*, 1700.

32. C.C. Vidyasagar, et al. Optical Properties of Dye-Sensitized Films Based on Cd-ZnO Nanoparticles. *Nanoscience and Nanotechnology: An International Journal*, **2012**, *2*, 18.

33. H. Matsuura and T. Miyazawa. Vibrational analysis of molten poly(ethylene glycol). *Journal of Polymer Science Part A-2: Polymer Physics*, **1969**, *7*, 1735.

34. C. Barrera, A.P. Herrera, and C. Rinaldi. Colloidal dispersions of monodisperse magnetite nanoparticles modified with poly(ethylene glycol). *Journal of Colloid and Interface Science*, **2009**, *329*, 107.

35. C.I. Covaliu, et al. Core–shell hybrid nanomaterials based on CoFe2O4 particles coated with PVP or PEG biopolymers for applications in biomedicine. *Powder Technology*, **2013**, *237*, 415.

36. L.T.M. Hoa, et al. Preparation and characterization of magnetic nanoparticles coated with polyethylene glycol. *Journal of Physics: Conference Series*, **2009**, *187*, 012048.

37. J. Drbohlavova, et al. Preparation and Properties of Various Magnetic Nanoparticles. *Sensors*, **2009**, *9*, 2352.

38. E. Darezereshki, M. Ranjbar, and F. Bakhtiari. One-step synthesis of maghemite (γ-Fe2O3) nano-particles by wet chemical method. *Journal of Alloys and Compounds*, **2010**, *502*, 257.

39. T. Ozkaya, et al. Synthesis of Fe3O4 nanoparticles at 100°C and its magnetic characterization. *Journal of Alloys and Compounds*, **2009**, *472*, 18.

40. P.B. Santhosh and N.P. Ulrih. Multifunctional superparamagnetic iron oxide nanoparticles: Promising tools in cancer theranostics. *Cancer Letters*, **2013**, *336*, 8.

41. S. García-Jimeno and J. Estelrich. Ferrofluid based on polyethylene glycol-coated iron oxide nanoparticles: Characterization and properties. *Colloids and Surfaces A: Physicochemical and Engineering Aspects*, **2013**, *420*, 74.

42. L. Dai, et al. One-pot facile synthesis of PEGylated superparamagnetic iron oxide nanoparticles for MRI contrast enhancement. *Materials Science and Engineering: C*, **2014**, *41*, 161.

43. M. Anbarasu, et al. Synthesis and characterization of polyethylene glycol (PEG) coated Fe3O4 nanoparticles by chemical co-precipitation method for biomedical applications. *Spectrochimica Acta Part A: Molecular and Biomolecular Spectroscopy*, **2015**, *135*, 536.

© 2025 The Authors. This article is licensed under a Creative Commons Attribution 4.0 BY International License.

© 2025 The Authors. This article is licensed under a Creative Commons Attribution 4.0 International License.

Deep Eutectic Solvent-Water Solvated Synthesis of Tungsten Oxide Nanoparticles with Photochromic and Antimicrobial Properties

Adetola Abiola Ajayi*, Olayinka Oderinde*, Sodiq Olalekan Ogunbayo, Olubunmi Ayoni Ogundiran, Adeola Roseline Olawuyi, Adebobola Ololade Agbeja

Editor's note: Photochromic and antimicrobial smart coatings hold great potential for advancements in modern applications, such as anti-UV photochromic contact lenses and bionic artificial skin. Ajayi et al. utilized deep eutectic solvents as a sustainable and adaptable medium for synthesizing tungsten oxide (WO_3) nanoparticles through an eco-friendly, low-temperature method. Optical analyses of the produced samples demonstrated strong UV absorption and a rapid, reversible photochromic transition occurring within just five seconds of UV exposure. Furthermore, antimicrobial tests indicated a dose-dependent bactericidal effect of the synthesized WO_3 nanoparticles against *Escherichia coli* and *Staphylococcus aureus*.

doi: 10.22034/jams.2025.210152

How to cite: A.A. Ajayi et al. *Journal of Applied Material Science*, **2025**, *1*, 210152.

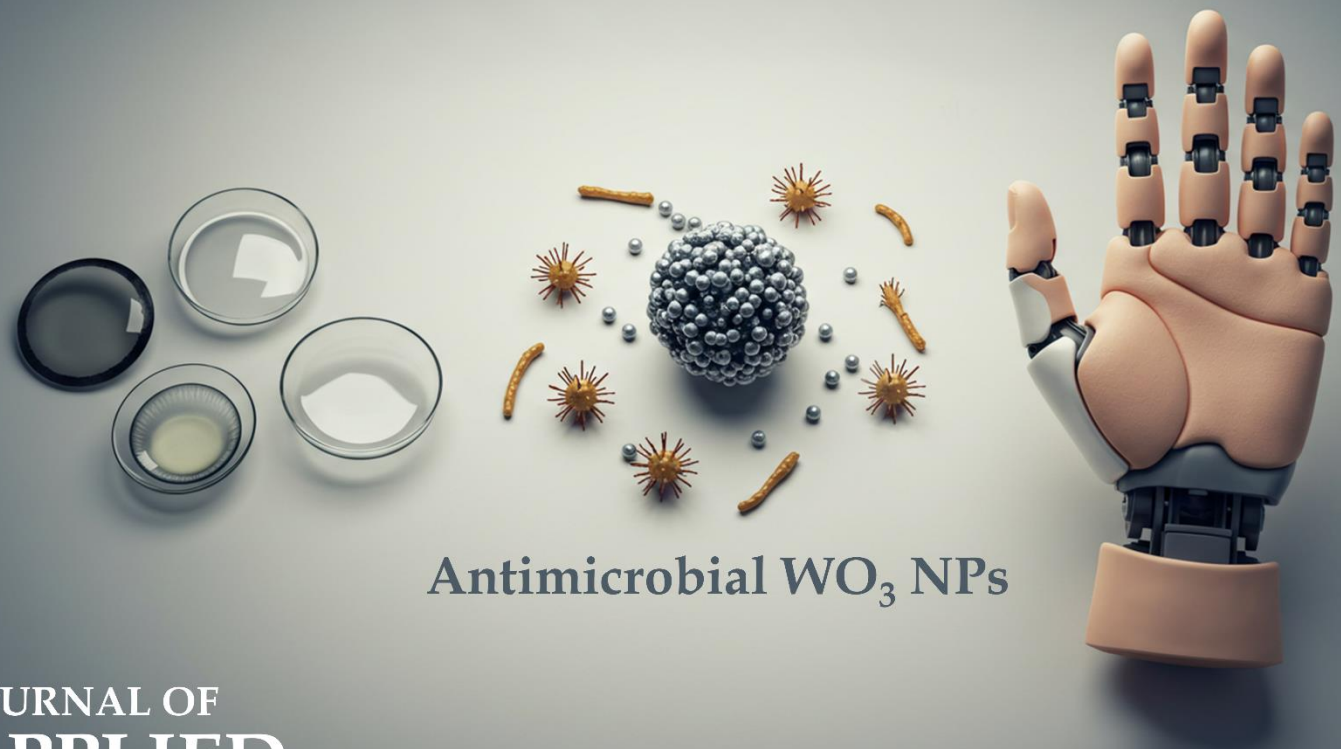

JOURNAL OF
APPLIED
MATERIAL
SCIENCE
jams.hsu.ac.ir

© 2025 *J. Appl. Mater. Sci.*This material is licensed under a Creative Commons Attribution 4.0 International License.

Journal of Applied Material Science **2025**, *1*, 210152
How to cite: A.A. Ajayi et al., *Journal of Applied Material Science*, **2025**, *1*, 210152.
Journal homepage: **jams.hsu.ac.ir**

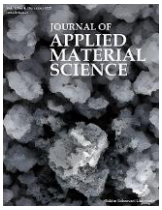

Original Research

Deep Eutectic Solvent-Water Solvated Synthesis of Tungsten Oxide Nanoparticles with Photochromic and Antimicrobial Properties

Adetola Abiola Ajayi [a,b,*], Olayinka Oderinde [a,c,*], Sodiq Olalekan Ogunbayo [a], Olubunmi Ayoni Ogundiran [d], Adeola Roseline Olawuyi [a], Adebobola Ololade Agbeja [e]

[a] *Department of Chemistry, Faculty of Natural and Applied Sciences, Lead City University, Ibadan, Nigeria*

[b] *Department of Science Laboratory Technology, School of Pure and Applied Sciences, Federal Polytechnic, PMB 50, Ilaro, Nigeria*

[c] *Department of Chemistry, Nile University of Nigeria, Plot 681, Cadastral Zone C-OO, Research & Institution Area, Jabi Airport Bypass, Abuja, FCT 900001, Nigeria*

[d] *Department of Chemical Sciences, Faculty of Sciences, Taraba State University, PMB 1167, Jalingo, Nigeria*

[e] *Department of Sustainable Forest Management, Forestry Research Institute of Nigeria, PMB 5054, Ibadan, Nigeria*

Abstract

Deep eutectic solvents (DESs) provide sustainable, tunable media for nanomaterial synthesis. In this work, tungsten oxide (WO_3) nanoparticles were prepared via a low-temperature green route using DES (choline chloride:ethylene glycol, 1:2) with varying water fractions to enhance solubility and reaction kinetics. Comprehensive characterization by FTIR, XRD, UV-Vis, SEM, and EDX confirmed the successful formation of WO_3 nanostructures with tunable crystallinity, morphology, and surface chemistry. FTIR spectra revealed distinct O-W-O/W-OH vibrational modes, while XRD identified monoclinic crystalline phases. SEM analysis demonstrated a morphology shift from irregular aggregates to sponge-like structures with increasing water content. Optical studies showed strong UV absorption (250-373 nm) and a rapid, reversible photochromic transition from transparent to blue within 5 s of UV exposure, fading back within 20 min under ambient conditions. Antimicrobial assays revealed dose-dependent bactericidal activity against *Escherichia coli* and *Staphylococcus aureus*, attributed to reactive oxygen species generation and oxygen-vacancy-mediated redox cycling, with the T1-D90W10 sample exhibiting the highest inhibition. This work establishes DES-water systems as versatile green platforms for fabricating multifunctional WO_3 Nanoparticles with synergistic photochromic and antimicrobial properties.

Keywords: Deep eutectic solvents; Tungsten oxide nanoparticles; Photochromic; Antimicrobial properties.

* Corresponding authors.
Email addresses: adetola.ajayi@federalpolyilaro.edu.ng (A.A. Ajayi), yinkaoderinde@yahoo.com (O. Oderinde)

Received 21 September 2025
Revised 4 October 2025
Accepted 14 October 2025
Available online 16 October 2025

https://doi.org/10.22034/jams.2025.210152
© 2025 The Authors. This article is licensed under a Creative Commons Attribution 4.0 International License.

1. Introduction

Semiconducting metal oxides (SMOs) are increasingly recognized as multifunctional materials with applications spanning energy conversion, photocatalysis, smart coatings, and environmental remediation [1]. Their chemical robustness, tunable electronic structures, and strong light-matter interactions provide a solid foundation for developing next-generation functional materials [2]. Beyond these well-established uses, semiconducting metal oxides have also demonstrated promising antibacterial properties, positioning them as alternatives to traditional antimicrobial agents in biomedical and environmental settings.

Among these SMOs, tungsten trioxide (WO_3) has sparked notable interest as a result of its desirable qualities, including low toxicity, rich oxygen vacancy chemistry, and exhibiting a bandgap estimated at 2.6-3.0 eV, which enables visible-light responsiveness [1-3]. This optical activity not only underpins its photochromic behavior, where reversible color changes occur under light irradiation, but also supports the generation of reactive oxygen species (ROS) capable of disrupting bacterial membranes and metabolic functions [4].

Compared with conventional organic antibacterial compounds, WO_3-based nanostructures offer higher stability, extended durability, and broad-spectrum antimicrobial action [5]. Nevertheless, progress in the development of WO_3 nanomaterials that combine photochromic response with antibacterial activity has been limited, and much of the current research relies on synthesis methods such as electrospinning, which can be energy-intensive, high-cost of production, and less environmentally sustainable [6].

To address these challenges, DESs have arisen as attractive green media for nanomaterial fabrication, usually obtained by hydrogen-bond association between a salt and a hydrogen-bond donor.

DESs provide advantages such as low vapor pressure, tunable composition, and the ability to direct nanostructure formation [6, 7]. Importantly, the incorporation of water into DESs significantly modifies their physicochemical properties by lowering viscosity, enhancing ion mobility, and facilitating more uniform particle nucleation and growth. This DES-water medium thus provides a versatile platform for tailoring nanoscale morphology and functionality [8]. Furthermore, the use of DES-water systems in nanomaterial synthesis aligns with the growing emphasis on sustainable and low-energy processing routes, enabling scalable fabrication of WO_3 nanostructures with controlled features.

Adjusting the water content in DES serves as a tunable parameter that influences morphology, crystallinity, and surface activity, which in turn can optimize photocatalytic and antibacterial performance under visible light. Such flexibility highlights DES-assisted synthesis as a promising route for the development of multifunctional WO_3-based nanomaterials with industrial and biomedical relevance [9].

In the present study, WO_3 nanoparticles were synthesized using a DES-water co-solvent system as a structure-directing medium. The as-prepared WO_3 nanoparticles were systematically characterized for their morphological and structural properties, while their photochromic response and antibacterial activity were evaluated to highlight the multifunctional potential of DES-assisted synthesis routes.

2. Experimental

2.1. Materials

Analytical-grade reagents of high purity were used throughout the synthesis. Sodium tungstate dihydrate ($Na_2WO_4 \cdot 2H_2O$, 98.5%) was supplied by Shanghai Yuanye BioTech Co. Ltd. Choline chloride ($C_5H_{14}ClNO$, 98.0%) was obtained from Eastman Chemical Co. Ltd, while ethylene glycol ($C_2H_6O_2$, 99.0%), Ethanol (C_2H_5OH, 99.8%) and Glacial acetic acid (CH_3COOH, 99.5%) were purchased from Dow Chemical, USA. The bacterial strains *Escherichia coli* and *Staphylococcus aureus* were sourced from Thermo Fisher Scientific (USA).

2.2. Preparation of Ethaline (DES) Solution

Ethaline was obtained by mixing choline chloride (1 mol) with ethylene glycol (2 mol) and heating the mixture at 80 °C under continuous stirring for 60 min until a homogeneous, clear liquid was obtained. The resultant deep eutectic solvent was subsequently allowed to cool at room temperature before use [9].

2.3. Preparation of Tungsten Oxide Nanoparticles

An appropriate quantity (1 g) of sodium tungstate dihydrate was added separately into DES/water

© 2025 The Authors. This article is licensed under a Creative Commons Attribution 4.0 International License.

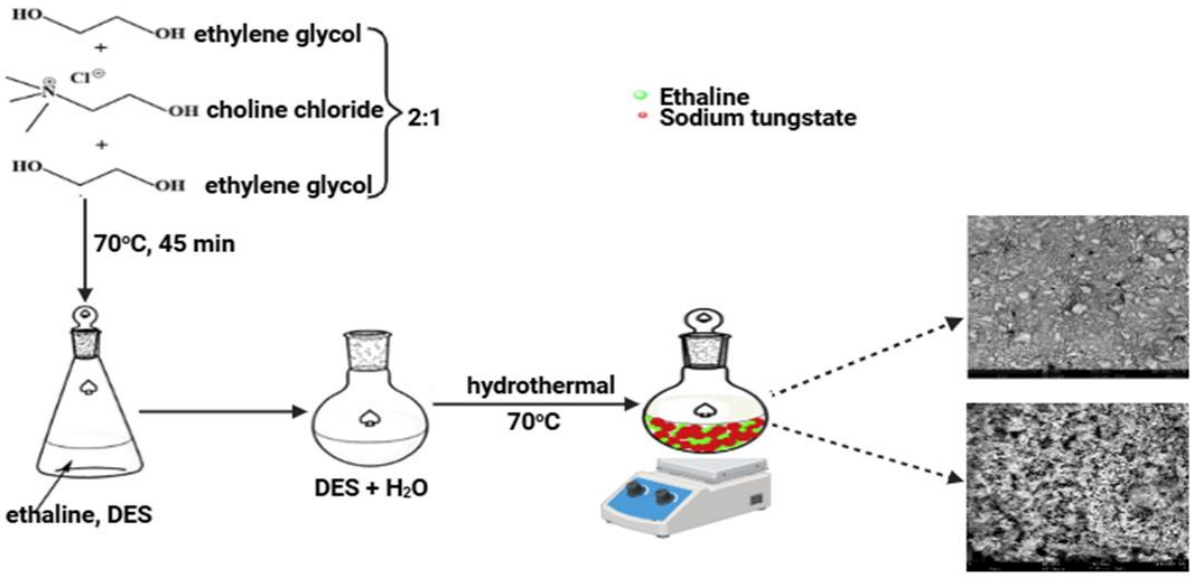

Figure 1. Schematic illustration showing the preparation and morphological transformation of the WO_3-NPs.

mixtures with different volume ratios: 90% DES/10% water (denoted as T1-D90W10), 80% DES/20% water (T1-D80W20), and 70% DES/30% water (T1-D70W30). Each mixture was heated to 70 °C on a magnetic stirrer hot plate under constant stirring for 30 min. Subsequently, 5 mL of glacial acetic acid ($C_2H_4O_2$) was added dropwise while stirring, and the reaction mixture was further stirred for 120 min. After cooling to room temperature, the suspensions were centrifuged at 5000 rpm for 20 min. The obtained precipitates were rinsed three times with ethanol to remove residual impurities, followed by drying in a hot-air oven at 80 °C for 12 h to yield tungsten oxide nanoparticles (Figure 1).

2.4. Measurements

Fourier transform infrared (FT-IR) spectra were obtained using a Nicolet iS50 spectrometer (Thermo Fisher, USA) in the 4000-400 cm^{-1} range with KBr pellets. X-ray diffraction (XRD) patterns were recorded on a SmartLab SE diffractometer (Rigaku, Japan) using Cu Kα radiation (λ = 0.15418 nm, 40 kV, 40 mA) over 10°-70° (2θ). Morphology and elemental composition were examined by scanning electron microscope (SEM) (JSM-7900F, JEOL, Japan) equipped with EDX. Optical absorption was measured with a Cary 5000 UV-Vis-NIR spectrophotometer (Agilent, USA) from 200-800 nm. Photochromic response was evaluated under 365 nm Xe lamp irradiation (300 mW cm^{-2}, Newport, USA) at 15 cm, with bleaching monitored in a dark, oxygen-rich atmosphere.

2.5. Photochromic Activity of As-Prepared Tungsten Oxide Nanoparticle.

The photochromic behavior of as-prepared samples was examined by dissolving 0.025 g of each material in 2 mL of deionized DI water. The mixtures were shaken for a few minutes, after which 1 mL of the resulting solution was transferred into a hollow groove. The samples were then irradiated with a 3 W, 365 nm light source (Shenyu Aic, Suzhou, China) placed 5 cm away, under ambient conditions [10, 11].

2.6. Antibacterial Test

To test their antibacterial effects, T1-D90W10 and T1-D70W30 were examined against *Staphylococcus aureus* and *Escherichia coli* using the agar disk diffusion method. Amoxicillin (30 mg) was included as a standard reference drug. The bacteria were first grown in nutrient broth and then evenly spread onto agar plates. Small sterile discs, each loaded with 100, 200, or 400 mg of the samples, were placed on the plates and left to incubate at 37 °C for 24 hours. After incubation, the clear zones around the discs, showing where bacterial growth was prevented, were measured. Each experiment was repeated three times, and the results are shown as the average values with their standard errors [12].

© 2025 The Authors. This article is licensed under a Creative Commons Attribution 4.0 International License.

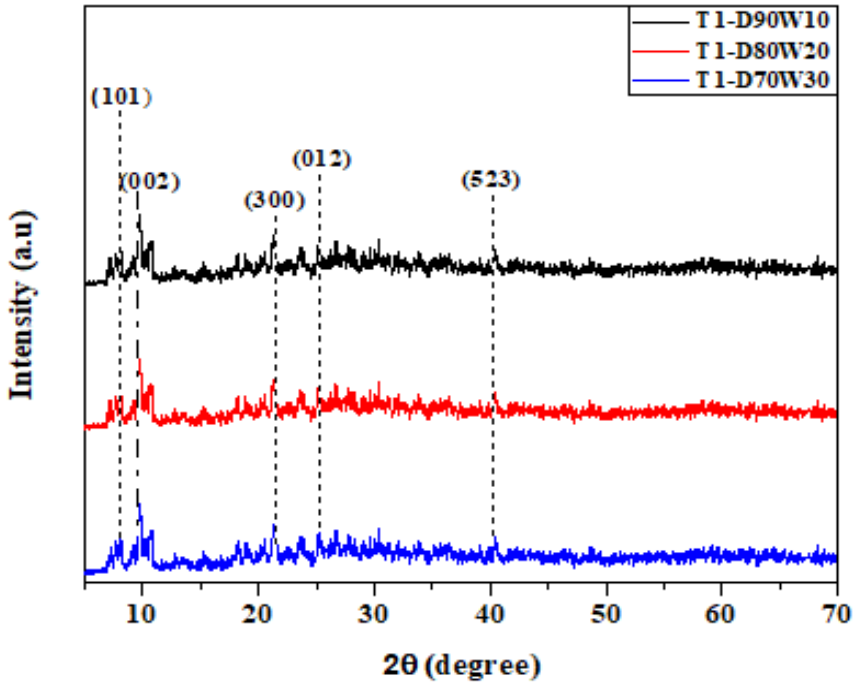

Figure 2. XRD patterns of as-prepared WO_3-NPs at different solvent volume ratios.

3. Results and discussion

3.1. XRD Analysis

Figure 2 shows XRD patterns of WO_3 nanoparticles synthesized using DES-water mixtures with different water contents. The diffraction peaks appear at the same position 8.12° (010), 10.66° (002), 21.34° (113), and 30.50° (130), corresponding to monoclinic tritungsten nonaoxide W_3O_9 (JPCDS Card 00-025-1496). However, the T1-D70W30 sample displays the most intense and well-defined crystallinity, while the T1-D90W10 sample presents broader and weaker peaks. This trend suggests that higher water content enhances crystallinity and promotes the growth of larger crystallite domains, whereas lower water levels result in smaller, less ordered particles. The improvement can be attributed to the ability of water to lower the viscosity of DES and accelerate the hydrolysis-condensation of the tungsten precursor, thereby supporting crystal development of WO_3 [13]. The crystallite sizes (Dc) of the samples were calculated using Scherrer's equation:

$$Dc = \frac{0.8\lambda}{\beta cos\,\theta} \qquad (1)$$

where Dc is the average crystallite diameter, λ is the wavelength of Cu Kα radiation (λ = 0.15418 nm), θ is the Bragg diffraction angle, and β is the full width at half maximum (FWHM) of the diffraction plane. Based on calculations from the intense diffraction peak, the crystallite sizes were determined to be 33.14nm, 33.59nm, and 33.89nm, respectively.

3.2. FTIR Analysis

Figure 3 shows FTIR spectra of as-prepared WO_3-NPs at different solvent volume ratios. In the fingerprint region (below 1000 cm^{-1}), the spectra clearly reveal the structural signatures of tungsten oxide nanoparticles. An intense signal around 898 cm^{-1} arises from the fundamental stretching vibrations of the metal-oxygen framework, while the peak at 776 cm^{-1} is linked to O-W-O bonds; both indicate the presence of WO_3 [14, 15]. Additional absorption features at 898 cm^{-1} and 979 cm^{-1} are linked to W-OH stretching vibrations [16]. The coexistence of O-W-O and W-OH modes in this region provides strong evidence for the successful formation of WO_3 nanoparticles [15, 16]. Moving to the mid-infrared region, distinct bands were also observed at 1469 cm^{-1} and 1081 cm^{-1}. The 1469 cm^{-1} peak corresponds to N-O stretching, pointing to traces of nitrate species possibly originating from the DES precursor, while bending

© 2025 The Authors. This article is licensed under a Creative Commons Attribution 4.0 International License.

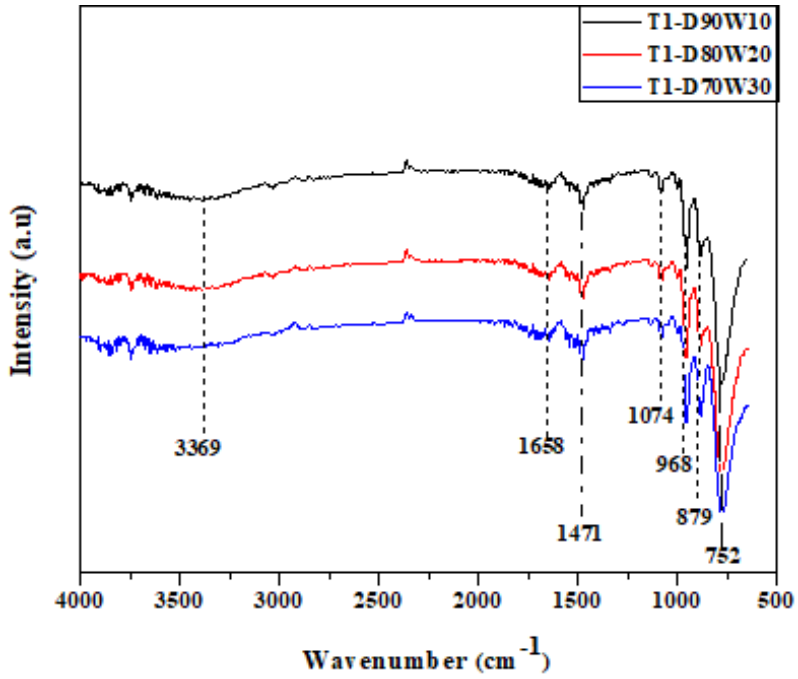

Figure 3. FTIR spectra of as-prepared WO_3-NPs at different solvent volume ratios.

vibrations of N-H in the same range indicate residual organic groups attached to the WO_3 surface [17].

At higher wavenumbers, a broad band near 3377 cm^{-1} represents O-H stretching, confirming the presence of hydroxyl groups from surface-adsorbed water or hydroxides. Similarly, a band at 1663 cm^{-1} is assigned to O-H bending, further highlighting the hydrated nature of the samples [17].

3.3. SEM Analysis

The SEM micrograph in Figure 4a reveals that the T1-D90W10 sample is composed of irregularly distributed, clustered crystals with non-uniform shapes. The particles appear highly aggregated, forming compact and coarse structures. This clustered morphology can be attributed to the limited solvation capacity and high viscosity of the DES medium in the absence of sufficient

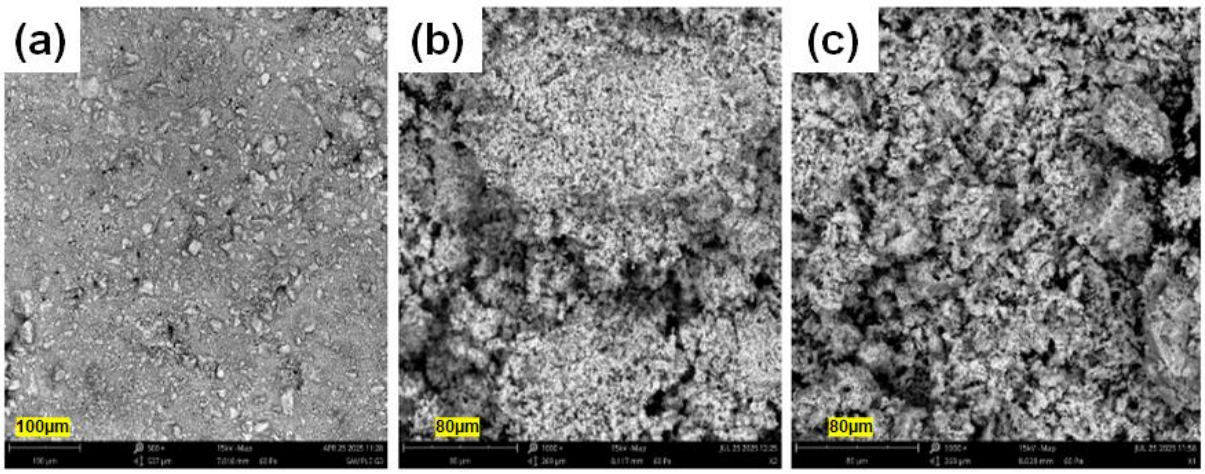

Figure 4. SEM images of the as-prepared WO_3-NPs: (a) T1-D90W10, (b) T1-D80W20, and (c) T1-D70W30.

© 2025 The Authors. This article is licensed under a Creative Commons Attribution 4.0 International License.

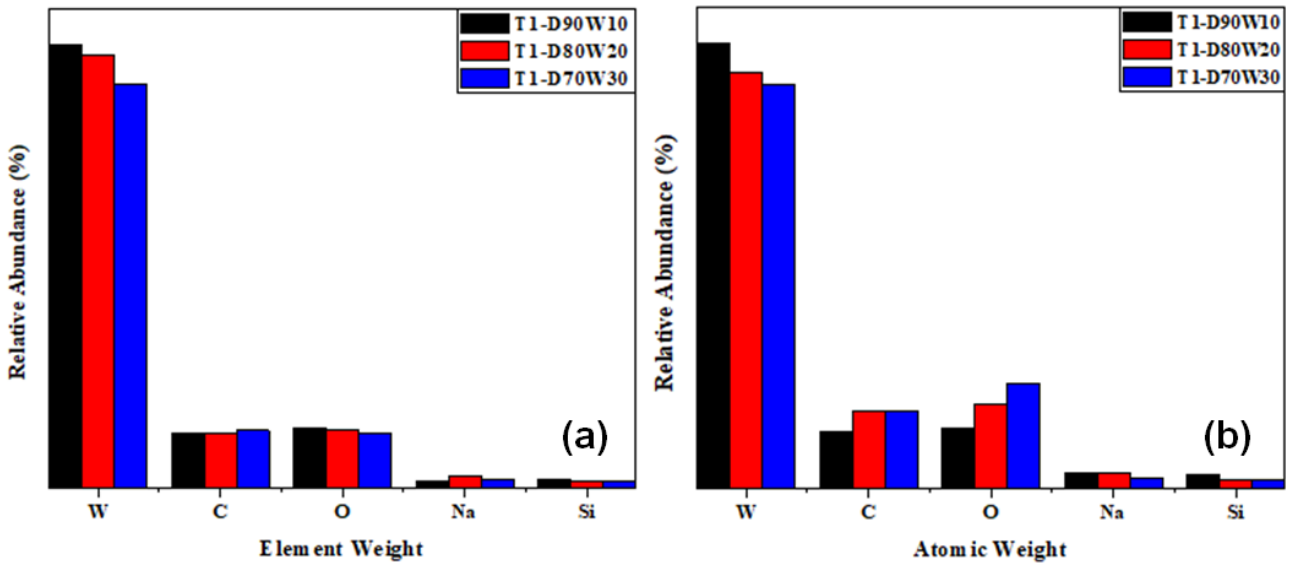

Figure 5. Variations in the relative elemental weight percent of the nanoparticles synthesized using different solvent volume ratios.

water, which restricts ion mobility and hinders uniform particle dispersion [18, 19].

Conversely, with increased water content (T1-D70W30), the morphology transforms into sponge-like formations, as shown in Figure 4c. This clearly demonstrates that the water concentration strongly influences the structural development and growth behavior of the composites. The observed morphological variation suggests that higher water content enhances solvation, thereby providing a more favorable reaction environment for uniform nucleation and controlled particle growth[12, 13]. Consequently, this results in a more refined and open microstructure within the DES-water-assisted system [10].

Energy Dispersive X-ray (EDX) analysis confirms the presence of tungsten (W), carbon (C), oxygen (O), sodium (Na), and chlorine (Cl) within the nanoparticles. Tungsten dominates the elemental composition, validating the formation of tungsten oxide (WO_3) as the principal crystalline phase [18, 19]. The high tungsten content suggests efficient incorporation of the metal precursor during synthesis, a factor critical for enhancing the nanoparticle's redox properties and antibacterial activity (Figure 5a and 5b).

3.4. UV Analysis

To assess the photochromic performance of the prepared samples, their light absorption behavior was examined using UV-Vis spectroscopy. As illustrated in Figure 6, the particles showed a strong and broad absorption response in the UV region, spanning 250-373 nm, with a peak threshold around 406 nm. This pronounced UV absorption can be linked not only to the influence of water but also to the presence of -OH and -NH groups originating from the deep eutectic solvent (DES) [17]. These groups, likely trapped within the aggregated particles, appear to facilitate the movement

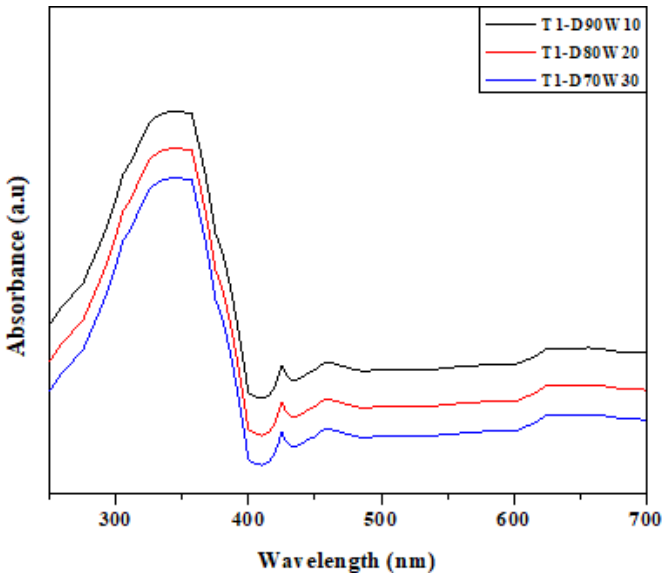

Figure 6. Absorbance characteristics of the as-synthesized WO_3-NPs at different solvent volume ratios.

© 2025 The Authors. This article is licensed under a Creative Commons Attribution 4.0 International License.

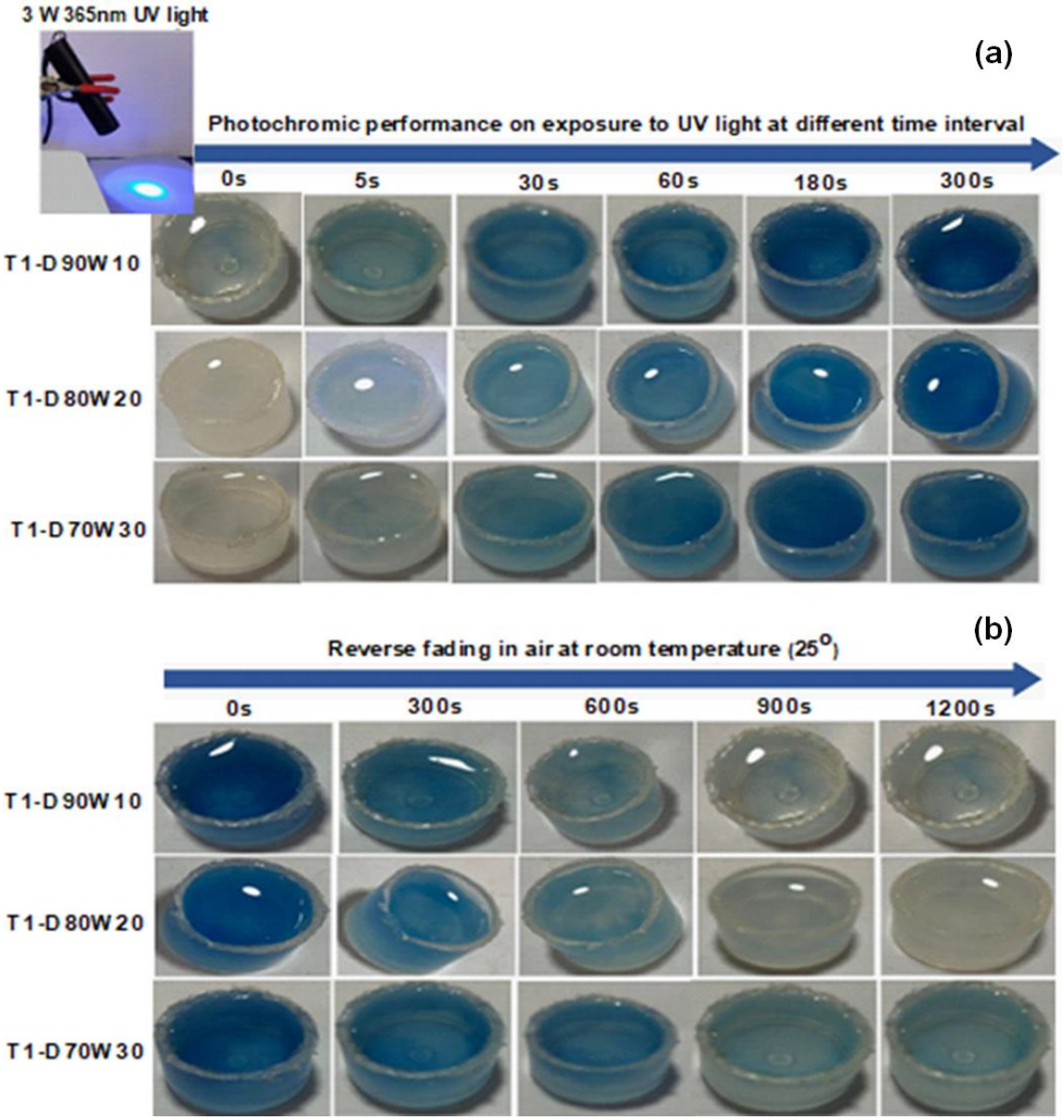

Figure 7. (a) Photochromic response and (b) reverse fading process of as-prepared WO_3 nanoparticles.

of photogenerated protons and electrons, thereby enhancing their transfer into the tungsten oxide semiconductor matrix (WO_3) [12]. In addition, the redshifted absorption edge observed in the samples indicates a slight narrowing of the bandgap, which favors visible-light responsiveness. Such modifications in optical properties highlight the synergistic role of DES-water interactions and functional groups in tailoring the electronic structure and improving the overall photochromic activity of WO_3 [16].

3.5. Photochromic Response and Reverse Fading Process

The photochromic behavior of the synthesized samples dispersed in deionized (DI) water was evaluated using a 3W UV lamp positioned 5 cm from the samples. As presented in Figure 7a, all samples showed a swift shift from transparency to a blue color within 5 seconds of irradiation, with the coloration gradually intensifying as the exposure time increased.

© 2025 The Authors. This article is licensed under a Creative Commons Attribution 4.0 International License.

This optical transition is attributed to the participation of mobile ionic species (NH_4^+ and H^+) and water molecules, which facilitate photo-induced charge transfer processes. Ammonium and protonic species, originating from donor components such as ethylene glycol in the DES medium and water, are adsorbed onto the WO_3 surface and migrate through hydrated pathways, thereby accelerating the charge transport [17].

The observed coloration is governed by a reversible reduction of W^{6+} to W^{5+}, a mechanism that underpins the switching efficiency of WO_3 and highlights its suitability for photo-responsive applications, including smart coatings and optical sensors [18].

Among the tested materials, the T1-D70W30 sample displayed the most intense coloration. This behavior can be linked to the role of water, as hydrogen species are detached from hydrogen-donor molecules (the ethylene glycol component of the DES solvent) and from H_2O, subsequently becoming adsorbed onto the surface of the metal oxides through specialized water-mediated pathways. Under irradiation, this process promotes hydrogen spillover, which facilitates the development of photochromic systems with enhanced sensitivity [19]. The bleaching process, as shown in Figure 7b, occurred gradually in open air. The T1-D70W30 sample required approximately 1200 s for full fading, whereas the T1-D90W10 and T1-D80W20 dispersions recovered more rapidly. This accelerated recovery at lower water contents is attributed to enhanced re-oxidation of W^{5+} to W^{6+} by ambient oxygen, coupled with faster electron-hole recombination dynamics [15, 16]. Collectively, these results highlight the critical role of water in modulating proton availability, charge transport pathways, and ultimately the balance between coloration depth and recovery speed [16].

3.6. Antibacterial Activity of As-Prepared Samples

The antimicrobial activity of the synthesized samples (T1-D90W10 and T1-D70W30), shown in Figure 8, was evaluated using the disc diffusion method to measure the zone of inhibition, while the microtube dilution method was employed to determine the Minimum Inhibitory Concentration (MIC) across varying concentrations. To ensure uniformity of the inoculum and achieve confluent microbial growth, a McFarland 0.5 turbidity standard was applied. At its highest tested concentration (400 mg/ml), the T1-D70W30 sample exhibited no inhibitory activity against *Staphylococcus aureus* (Gram-positive). However, the same sample produced moderate inhibition zones against *Escherichia coli* (Gram-negative) when compared to ciprofloxacin (positive control), indicating some degree of selective antibacterial activity.

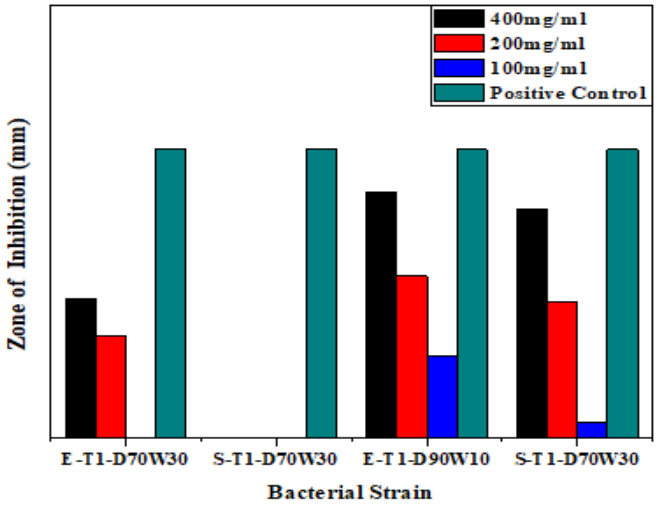

Figure 8. Antimicrobial activities of T1-D90W10 and T1-D70W30 composite against *S. aureus* and *E. coli*.

In contrast, the T1-D90W10 sample demonstrated stronger antimicrobial performance (Figure 8). It produced pronounced inhibition zones against *S. aureus* and moderate zones against *E. coli*, showing broader efficacy relative to ciprofloxacin [7]. However, the comparative results indicate that the T1-D90W10 sample was more effective than the T1-D70W30 sample in terms of inhibition zone diameter, MIC, and Minimum Bactericidal Concentration (MBC) [20, 21]. The reduced potency observed in the T1-D70W30 ml sample may be attributed to the higher water content, which could dilute active components, alter the chemical structure of Ethaline, or interfere with antimicrobial interactions at the bacterial membrane level. Such effects appear to vary with bacterial cell wall architecture, as differences were noted between Gram-positive (*S. aureus*) and Gram-negative (*E. coli*) strains [7, 22].

4. Conclusions

This work demonstrated the successful synthesis of reversible photochromic tungsten oxide nanoparticles via a simple, low-temperature, and environmentally friendly DES-water approach. Characterizations (FTIR,

© 2025 The Authors. This article is licensed under a Creative Commons Attribution 4.0 International License.

XRD, UV-Vis, SEM-EDX) confirmed their controlled crystallinity, uniform distribution, and stable metal-oxygen bonding. The nanoparticles showed strong UV-Vis absorption, rapid coloration under UV irradiation, and reversible fading, highlighting their suitability for optical devices, sensors, and rewritable media. In addition, the WO_3 nanocomposites exhibited strong antimicrobial activity, effectively inhibiting both *Staphylococcus aureus* and *Escherichia coli* through synergistic ROS generation and oxygen vacancy-mediated redox cycling. This dual functionality, photochromism, and antimicrobial performance demonstrate the potential of DES-water synthesis as a sustainable platform for developing advanced nanomaterials with applications in healthcare, water purification, food safety, and protective equipment. The study provides new insights into how DES-water interactions influence nanoparticle functionality, offering a blueprint for tailoring material properties through green chemistry. Its findings also contribute to addressing global challenges of antimicrobial resistance while advancing multifunctional nanomaterials. Future work could explore the scalability and integration of these materials into practical devices and coatings.

Conflict of Interest

The authors declare no conflict of interest.

References

1. O. Ejeromedoghene, et al. Transparent and photochromic poly(hydroxyethyl acrylate–acrylamide)/WO_3 hydrogel with antibacterial properties against bacterial keratitis in contact lens. *Journal of Applied Polymer Science*, **2021**, *139*, 51815.
2. B. Cui, et al. Photochromic performance of hydrogel based on deep eutectic solvent induced water soluble Cu-doped WO3 hybrids with antibacterial property. *Journal of Photochemistry and Photobiology A: Chemistry*, **2023**, *435*, 114320.
3. Y.-H. Lu, et al. A facile green antisolvent approach to Cu²⁺-doped ZnO nanocrystals with visible-light-responsive photoactivities. *Nanoscale*, **2014**, *6*, 8796.
4. Y. Song, et al. Aqueous synthesis and photochromic study of Mo/W oxide hollow microspheres. *RSC Advances*, **2016**, *6*, 99898.
5. O.L. Pop, et al. Cerium Oxide Nanoparticles and Their Efficient Antibacterial Application In Vitro against Gram-Positive and Gram-Negative Pathogens. *Nanomaterials*, **2020**, *10*, 1614.
6. Y. Yao, et al. A Review on the Properties and Applications of WO3 Nanostructure−Based Optical and Electronic Devices. *Nanomaterials*, **2021**, *11*, 2136.
7. A. Salim and S. Sadhasivam. Biofabricated MoO3 nanoparticles for biomedical applications: Antibacterial efficacy, hemocompatibility, and wound healing properties. *Nano and Medical Materials*, **2023**, *3*, 73.
8. P.P. Tumkur, et al. Cerium Oxide Nanoparticles: Synthesis and Characterization for Biosafe Applications. *Nanomanufacturing*, **2021**, *1*, 176.
9. M. Nyoka, et al. Synthesis of Cerium Oxide Nanoparticles Using Various Methods: Implications for Biomedical Applications. *Nanomaterials*, **2020**, *10*, 242.
10. J. Gutpa, et al. PVD techniques proffering avenues for fabrication of porous tungsten oxide (WO3) thin films: A review. *Materials Science in Semiconductor Processing*, **2022**, *143*, 106534.
11. M. Aryafard, et al. Experimental and theoretical investigation of solvatochromic properties and ion solvation structure in DESs of reline, glyceline, ethaline and their mixtures with PEG 400. *Journal of Molecular Liquids*, **2019**, *284*, 59.
12. O. Oderinde, et al. Facile synthesis and study of the photochromic properties of deep eutectic solvent-templated cuboctahedral-WO3/MoO3 nanocomposites. *Superlattices and Microstructures*, **2019**, *125*, 103.
13. J. Gomez-Hermoso-de-Mendoza, et al. Flexible photochromic cellulose triacetate based bionanocomposites modified with sol-gel synthesized V2O5 nanoparticles. *Carbohydrate Polymers*, **2019**, *208*, 50.
14. Y. Chen, et al. Core-shell structured CsxWO3@ZnO with excellent stability and high performance on near-infrared shielding. *Ceramics International*, **2018**, *44*, 2738.
15. C. Dong, et al. A review on WO3 based gas sensors: Morphology control and enhanced sensing properties. *Journal of Alloys and Compounds*, **2020**, *820*, 153194.
16. L. Pan, Y. Shen, and Z. Li. Hydrothermal synthesis of WO3 films on the TiO2 substrates and their photochromic properties. *Materials Science in Semiconductor Processing*, **2015**, *40*, 479.
17. T.J. DeJournett and J.B. Spicer. The influence of oxygen on the microstructural, optical and photochromic properties of polymer-matrix, tungsten-oxide nanocomposite films. *Solar Energy Materials and Solar Cells*, **2014**, *120*, 102.
18. Y. Zhang, et al. Template-free to fabricate highly sensitive and selective acetone gas sensor based on WO3 microspheres. *Vacuum*, **2013**, *95*, 30.
19. V.S. Kavitha, et al. High quality, highly transparent Cu incorporated WO3 thin films suitable for blue LED application. *Vacuum*, **2020**, *172*, 109044.

© 2025 The Authors. This article is licensed under a Creative Commons Attribution 4.0 International License.

20. V. Gopal, et al. Visible light photocatalytic decomposition of organic dye and biodegradation-resistant antibiotic pollutants using cerium-doped tungsten trioxide nanoparticles. *Research on Chemical Intermediates*, **2024**, *50*, 5097.

21. Y. Dai, et al. Application of natural deep eutectic solvents to the extraction of anthocyanins from Catharanthus roseus with high extractability and stability replacing conventional organic solvents. *Journal of Chromatography A*, **2016**, *1434*, 50.

22. A. Sharma, et al. Methods of preparation of metal-doped and hybrid tungsten oxide nanoparticles for anticancer, antibacterial, and biosensing applications. *Surfaces and Interfaces*, **2022**, *28*, 101641.

© 2025 The Authors. This article is licensed under a Creative Commons Attribution 4.0 BY International License.

© 2025 The Authors. This article is licensed under a Creative Commons Attribution 4.0 International License.

Evaluation of *Phytolacca americana* L. extract as green corrosion inhibitor for mild steel: a study of the solution phase

Milad Sheydaei *

Department of Chemical and Polymer Engineering, University of Garmsar, Garmsar, Iran

Editor's note: Green corrosion inhibitors are gaining popularity, particularly those derived from plants, due to their non-toxic nature, affordability, and accessibility. Sheydaei conducted a study on the extract of *Phytolacca americana* L. (also known as American pokeweed), assessing its effectiveness in preventing mild steel corrosion. The findings indicated that the plant extract successfully inhibited corrosion, as it contains compounds such as betacyanins, flavonoids, and polyphenols.

doi: 10.22034/jams.2025.210153

How to cite: M. Sheydaei, *Journal of Applied Material Science*, **2025**, *1*, 210153.

JOURNAL OF
APPLIED
MATERIAL
SCIENCE
jams.hsu.ac.ir

© 2025 *J. Appl. Mater. Sci.* This material is licensed under a Creative Commons Attribution 4.0 International License.

Journal of Applied Material Science **2025**, *1*, 210153
How to cite: M. Sheydaei, *Journal of Applied Material Science*, **2025**, *1*, 210153.
Journal homepage: **jams.hsu.ac.ir**

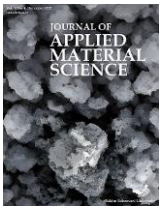

Communication

Evaluation of *Phytolacca americana* L. extract as green corrosion inhibitor for mild steel: a study of the solution phase

Milad Sheydaei *

Department of Chemical and Polymer Engineering, Faculty of Engineering, University of Garmsar, Garmsar, Iran

Abstract

Corrosion is undoubtedly the most serious threat to metals. The behavior of this phenomenon is silent and slow, yet continuous, causing the destruction of metal structures and resulting in huge financial losses, as well as environmental pollution. This process is often regarded as a slow behavior, but in environments like oceans, it can be extremely violent and rapid. Researchers are continually seeking solutions to prevent and delay this process. It can be said that in the past decades, chemical corrosion inhibitors have been very popular among researchers and many industries. However, it must be admitted that many of them are toxic and cause great damage to the environment. In recent years, green corrosion inhibitors have been widely studied, and among them, plant-based ones are perhaps the most popular. In this study, *Phytolacca americana* L. extract was prepared, and its inhibition corrosion efficiency on mild steel was evaluated. For this evaluation, electrochemical impedance spectroscopy (EIS) and polarization test were used. The results showed that the extract is effective in inhibiting corrosion. The results showed that the charge transfer resistance (R_{ct}) for mild steel decreased significantly with increasing immersion time, but in the presence of the extract, this decrease was surprisingly less.

Keywords: Green chemistry; Inhibition efficiency; Protection.

1. Introduction

Polymer coatings can always be considered a suitable candidate for corrosion prevention [1]. To improve the performance of these coatings, chemical inhibitors as well as nanomaterials can be used [2, 3]. The use of nanomaterials often increases the cost of coatings, but chemical inhibitors still have their own fans based on their amazing performance [4]. However, chemical inhibitors cause serious problems for the environment because most of them are very toxic [5]. In recent years, research on the use of green corrosion inhibitors has become very popular, and plants are one of the candidates being studied because, in addition to being non-toxic, they are very cheap and available [6]. Some literature has reported inhibition efficiency of up to 99% for some plants [7, 8]. In general, it can be said that the inhibition efficiency depends on many parameters, such as the active phytochemical compounds of the plant, the solvent, the temperature, and the corrosive medium [9].

* Corresponding author.
Email address: md.sheydaei@fmgarmsar.ac.ir (M. Sheydaei)

Received 12 October 2025
Revised 19 November 2025
Accepted 27 November 2025
Available online 4 December 2025

https://doi.org/10.22034/jams.2025.210153
© 2025 The Authors. This article is licensed under a Creative Commons Attribution 4.0 International License.

Among plants, *Phytolacca americana* L. (Figure 1) is a well-known tropical plant native to North and South America but also distributed in Africa, Europe, and Asia [10]. This plant is used in traditional medicine in South and Central America for its antimicrobial and anti-inflammatory effects [11]. This plant also has the capacity to accumulate the heavy metal cadmium (10,700 mg/kg), which can be hazardous, as this plant will contain high levels of cadmium if grown in cadmium-contaminated soils [12]. Therefore, before using plants, one must make sure that they are not contaminated, because otherwise there is a possibility of contaminating the environment and causing many diseases, such as cancer and kidney damage, through heavy metals [13-16]. In this study, *Phytolacca americana* L. extract was prepared using ethanol, and its inhibitory efficacy in a saline medium was evaluated for mild steel.

Figure 1. *Phytolacca americana* L. plant.

2. Experimental

2.1. Materials

Sodium chloride and mild steel were obtained from Merck and Mobarakeh Steel Company, respectively. The *Phytolacca americana* L. plant was obtained from a local farm (Chalus city, Mazandaran province, Iran).

2.2. Preparation of extract, mild steel substrate, and electrochemical tests

The *Phytolacca americana* L. fruits were washed with distilled water. Then, the fruits were added to ethanol and heated for 30 min at 50°C. The extract was then separated by filtration and cooled to ambient temperature. Surface images were obtained using a Zitazy digital microscope (Insight Pro). A potentiostat-galvanostat (CorrTest CS350) was used to evaluate EIS and the polarization test. The substrates were coated with a mixture of Beeswax melt and colophony resin, and only a 1×1 cm² area was selected to contact the sodium chloride solution. 100 mL of *Phytolacca americana* L. extract was mixed with 1 L of sodium chloride solution (3.5 wt.%) under magnetic stirring, and then the substrates were immersed in it. Also, a sodium chloride solution (3.5 wt.%) was used as a reference solution. The inhibition efficiency (η) for the EIS test was obtained using equation (1) [17]. The polarization test was performed after 24 h of immersion of the substrate in the solution at a scan rate of 0.5 mV/s and within the range of ±200 mV. The percentage Inhibition efficiency (IE%) was calculated, with I_{corr} as the corrosion current density, using equation (2) [18, 19]:

$$\eta\,(\%) = 100 \times \left(1 - \frac{R_{ct\ without\ extract}}{R_{ct\ with\ extract}}\right) \quad (1)$$

$$IE(\%) = \frac{I_{corr\ (without\ extract)} - I_{corr\ (with\ extract)}}{I_{corr\ (without\ extract)}} \times 100 \quad (2)$$

3. Results and discussion

The corrosion inhibition of the extract was evaluated by electrochemical impedance spectroscopy test results, as shown in Figure 2 and Table 1. Figure 2 shows the Nyquist plots of the samples at different immersion times, indicating that mild steel is degrading in the absence of the extract, as evidenced by the changes in the diameter of the plots. In fact, the diameter of the curve shows that the Rct decreases with increasing immersion time [17]. This decrease in diameter indicates that the corrosive species penetrate the mild steel with increasing immersion time. On the other hand, the Bode plots (see Figure 2d) also show a decreasing trend with increasing immersion time. However, in the presence of the extract, the results are quite different (see Figure 2 b and d). As can be seen in the results, there is an increase in the diameter of the Nyquist plots, as well as a significant increase in the Bode plots.

© 2025 The Authors. This article is licensed under a Creative Commons Attribution 4.0 International License.

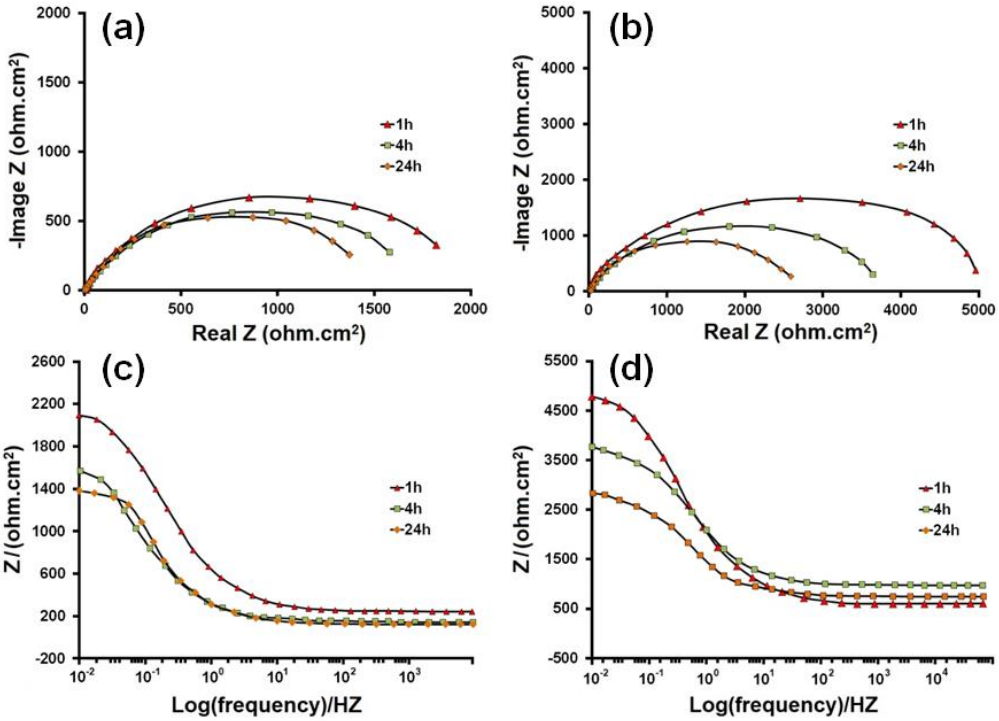

Figure 2. Nyquist plots (a and b) and Bode plots (c and d) of mild steel at different immersion times: in the absence of extract (a and c) and in the presence of extract (b and d).

Although there is a decreasing trend in both Nyquist and Bad plots with time. But the sample containing the extract shows better resistance even after 24 h than the sample in the absence of the extract after 1 h. Although these types of inhibitors are very popular, their effectiveness decreases significantly with increasing immersion time, a concern that can be largely addressed by encapsulation [4, 17, 20].

Phytolacca americana L. contains betacyanins, flavonoids, phenolic acids, phytosterols, esculentosides A and B, saponins, and polyphenolic compounds [10, 21]. These compounds in *Phytolacca americana* L. can adsorb onto metal surfaces. In fact, this ability is related to the π-electron transfer between oxygen atoms and aromatic rings of compounds with vacant d-orbitals on the surface [4, 17, 20]. This process causes the anodic regions to be blocked and a protective layer to form [17, 20]. In fact, it can be said that the surface is passivated, which is why the Bode plots increase in the presence of the extract [4, 17, 20].

Figure 3a shows the equivalent circuit that best matches the impedance results. Also, Figure 3b shows the potentiodynamic polarization test curves, and various parameters calculated from these curves are reported in Table 2. The results show that the effect of adding the extract to the solution on the anodic half-reaction is greater and ultimately causes E_{corr} to shift towards positive values. In fact, this change indicates the

Table 1. Parameters obtained from electrochemical impedance spectroscopy results

Samples	Time (h)	R_{ct} (ohm.cm²)	R_s (ohm.cm²)	log |z| (ohm.cm²)	η (%)
Without extract	1	1807.27	6.9	1911.17	-
	4	1597.07	7.6	1503.24	-
	24	1372.19	7.4	1318.16	-
With Extract	1	4960.79	11	4727.56	64
	4	3644.86	13	3348.71	56
	24	2592.76	12	2294.32	47

© 2025 The Authors. This article is licensed under a Creative Commons Attribution 4.0 International License.

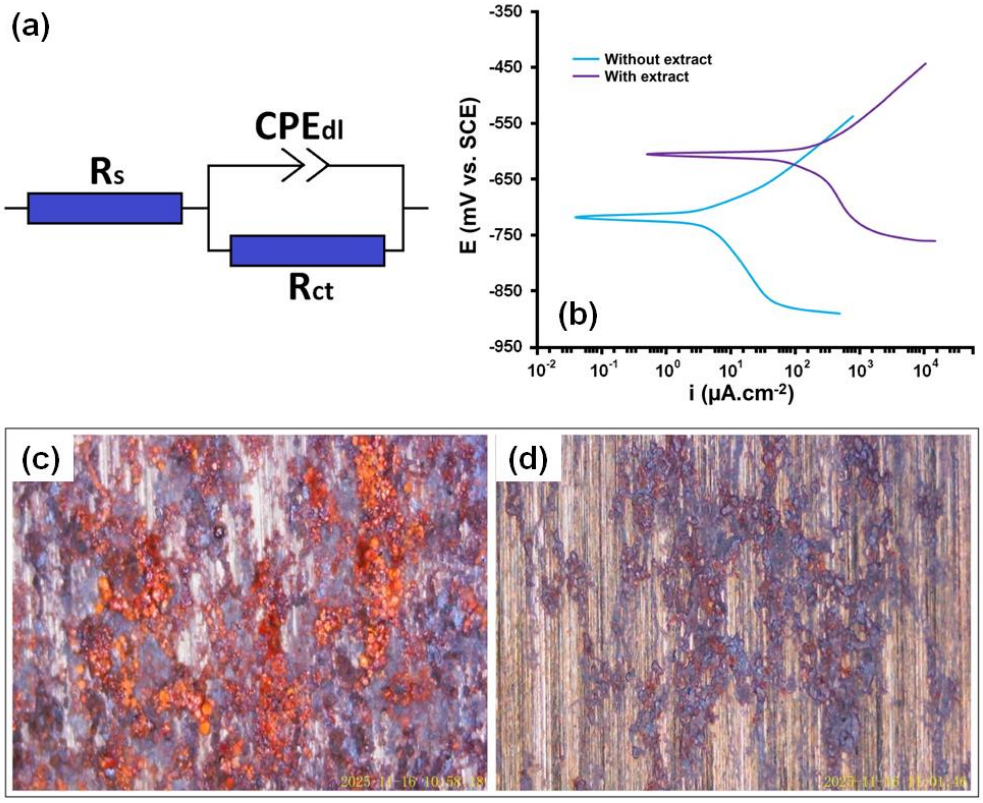

Figure 3. Equivalent circuit to describe the results (a), The polarization curves of samples immersed for 24 h (b), and images of the mild steel surface immersed in the saline solution, without extract (c), and with extract (d).

formation of a protective layer on the substrate surface that provides protection. It can be said that due to the overall E_{corr} shift of more than +85 mV, this extract can be classified in the group of anodic inhibitors. The addition of the extract also caused a significant decrease in i_{corr}, indicating better corrosion behavior [17-19].

Figure 3 also shows images of the mild steel surface after 24 h of immersion (panels c and d). The images show that the entire surface of the blank sample is filled with rust and corrosion products, but the surface of the sample that used the extract as an inhibitor contains far fewer corrosion products. In the blank sample, corrosion has caused the formation of numerous grooves and pores on the surface, and the presence of irregular and porous deposits on the steel surface indicates the formation and deposition of corrosion products on the surface, but the surface of the sample that used the extract as an inhibitor had far fewer roughness and pores. These images show the inhibitory role of the compounds in the extract, which prevents surface degradation by creating a protective layer with low permeability against corrosive ions.

4. Conclusions

In summary, a corrosion inhibitor was prepared using *Phytolacca americana* L. extract and ethanol. This plant

Table 2. Electrochemical parameters obtained from the polarization test on mild steel immersed in the saline solution after 24 h

Samples	Ecorr vs. SCE (mV)	icorr (A/cm²)	βα (V/dec)	βc (V/dec)	IE (%)
Without extract	-715	2.561×10^{-6}	0.07	0.322	-
With extract	-605	9.76×10^{-7}	0.067	0.179	61.88

Note: Corrosion potential (E_{corr}), the anodic Tafel slope (βα), and the cathodic Tafel slope (βc).

© 2025 The Authors. This article is licensed under a Creative Commons Attribution 4.0 International License.

contains compounds such as betacyanins, flavonoids, and polyphenolic compounds, which are responsible for the corrosion inhibition potential of this extract because these compounds can adsorb onto the metal surface. Plant-based inhibitors are always very tempting due to their low cost, but it should be kept in mind that their effectiveness decreases with increasing temperature and immersion time, although this problem can be largely solved with solutions such as encapsulation.

Conflict of Interest

The author declares no conflict of interest.

References

1. G.P.V. Dalmora, et al. Methods of corrosion prevention for steel in marine environments: A review. *Results in Surfaces and Interfaces*, **2025**, *18*, 100430.
2. A. Yadav, S. Panjikar, and R.K. Singh Raman. Graphene-Based Impregnation into Polymeric Coating for Corrosion Resistance. *Nanomaterials*, **2025**, *15*, 486.
3. F. Alasmari, et al. A review on the application of various nanotechnologies for corrosion prevention. *Nanotechnology for Environmental Engineering*, **2024**, *10*, 3.
4. M. Sheydaei, M. Edraki, and F.S.-J. Abad. Matcha-modified clay polyurethane coating: improving thermal, mechanical, antimicrobial, and anticorrosion performance. *Iranian Polymer Journal*, **2023**, *32*, 1643.
5. M. Yeganeh, et al. Corrosion Inhibitor of API Pipeline Steels: A Review. *Journal of Bio- and Tribo-Corrosion*, **2025**, *11*, 44.
6. M. Talha. Biomacromolecules as green corrosion inhibitors: a review based on mild steel corrosion in acidic media. *Corrosion Reviews*, **2024**, *43*, 409.
7. H. Li, S. Zhang, and Y. Qiang. Corrosion retardation effect of a green cauliflower extract on copper in H2SO4 solution: Electrochemical and theoretical explorations. *Journal of Molecular Liquids*, **2021**, *321*, 114450.
8. Q. Liu, et al. A novel green reinforcement corrosion inhibitor extracted from waste Platanus acerifolia leaves. *Construction and Building Materials*, **2020**, *260*, 119695.
9. C.A. Barbu, et al. Critical Review Regarding the Application of Plant Extracts as Eco-Friendly Corrosion Inhibitors—A Sustainable Interdisciplinary Approach. *Molecules*, **2025**, *30*, 3722.
10. I.D. Veleşcu, et al. Valorization of Betalain Pigments Extracted from Phytolacca americana L. Berries as Natural Colorant in Cheese Formulation. *Agriculture*, **2025**, *15*, 86.
11. J.K. Patra, et al. Antibacterial effect of crude extract and metabolites of Phytolacca americana on pathogens responsible for periodontal inflammatory diseases and dental caries. *BMC Complementary and Alternative Medicine*, **2014**, *14*, 343.
12. M. Sheydaei. Investigation of Heavy Metals Pollution and Their Removal Methods: A Review. *Geomicrobiology Journal*, **2024**, *41*, 213.
13. M. Sheydaei. Heavy Metals Contamination in Soil and Rice and their Removal Processes: A Brief Review. *Geomicrobiology Journal*, **2024**, *41*, 721.
14. M. Sheydaei. Cancer and Polymeric-Carriers. *Biomedical Journal of Scientific & Technical Research*, **2020**, *31*, 24107.
15. M. Sheydaei. Breast Cancer and the Role of Polymer-Carriers in Treatment. *Biomedical Journal of Scientific & Technical Research*, **2021**, *34*, 27057.
16. M. Sheydaei and E. Alinia Ahandani. Cancer and the role of polymeric-carriers in diagnosis and treatment. *Journal of Advanced Biomedical Sciences*, **2020**, *10*, 2408.
17. M. Edraki and M. Sheydaei. Investigation of date seed powder as green corrosion inhibitor for mild steel: A study of solution and coating phases. *Hybrid Advances*, **2024**, *6*, 100238.
18. M. Edraki, et al. Enhanced mechanical, anticorrosion, and antimicrobial properties of epoxy coating via pine pollen modified clay incorporation. *Iranian Journal of Chemistry and Chemical Engineering*, **2023**, *42*, 2775.
19. M. Edraki and M. Sheydaei. Investigation of the Dual Active/Barrier Corrosion Protection, Mechanical and Thermal Properties of a Vinyl Ester Coating Doped with Ginger Modified Clay Nanoparticles. *Russian Journal of Applied Chemistry*, **2022**, *95*, 1481.
20. E. Milad, et al. Protective Nanocomposite Coating Based on Ginger Modified Clay and Polyurethane: Preparation, Characterization and Evaluation Anti-Corrosion and Mechanical Properties. *Polymer Science, Series B*, **2022**, *64*, 756.
21. N.M. Fahmy, et al. Chemical exploration of different extracts from Phytolacca americana leaves and their potential utilization for global health problems: in silico and network pharmacology validation. *Journal of Biomolecular Structure and Dynamics*, **2024**, *43*, 5178.

© 2025 The Authors. Authors retain the copyright and full publishing rights. This article is licensed under a Creative Commons Attribution 4.0 BY International License.

© 2025 The Authors. This article is licensed under a Creative Commons Attribution 4.0 International License.

Preparation and Characterization of a Ni-Co-Ce Coordination Framework Coated Nickel Foam Electrode for Supercapacitor Applications

Yasin Borhani [a], Zeinab Jarrahi [a,*], Ashkan Abareshi [b]

[a] *Department of Polymer Engineering, Hakim Sabzevari University, Sabzevar, Iran*

[b] *Faculty of Materials Science and Engineering, Sharif University of Technology, Tehran, Iran*

Editor's note: The performance of supercapacitors is heavily influenced by the electrode materials used. These materials should exhibit excellent electrical conductivity, a large surface area, and a high number of electroactive sites. Borhani et al. reported the synthesis of a trimetallic Ni-Co-Ce coordination compound using a hydrothermal synthesis method, which serves as a coating for nickel foam-based electrodes in supercapacitors. This new coating demonstrated stable electrochemical performance, achieving an increase in specific capacitance from 0.74 F/g to 2.6 F/g over multiple cycles.

doi: 10.22034/jams.2025.210154

How to cite: Y. Borhani et al. *Journal of Applied Material Science*, **2025**, *1*, 210154.

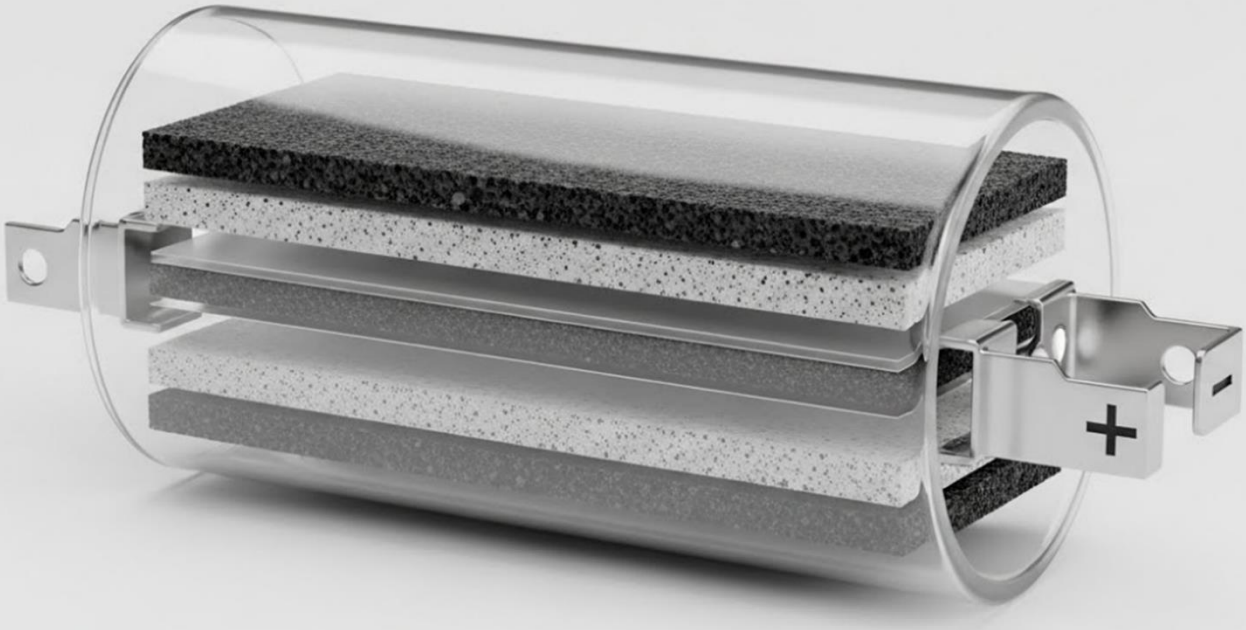

JOURNAL OF
APPLIED
MATERIAL
SCIENCE
jams.hsu.ac.ir

© 2025 *J. Appl. Mater. Sci.* This material is licensed under a Creative Commons Attribution 4.0 International License.

Journal of Applied Material Science **2025**, *1*, 210154
How to cite: Y. Borhani et al., *Journal of Applied Material Science*, **2025**, *1*, 210154.
Journal homepage: **jams.hsu.ac.ir**

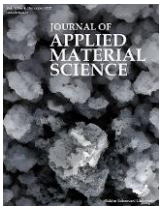

Original Research

Preparation and Characterization of a Ni-Co-Ce Coordination Framework Coated Nickel Foam Electrode for Supercapacitor Applications

Yasin Borhani [a], Zeinab Jarrahi [a,*], Ashkan Abareshi [b]

[a] *Department of Polymer Engineering, Hakim Sabzevari University, Sabzevar, Iran*

[b] *Faculty of Materials Science and Engineering, Sharif University of Technology, Tehran, Iran*

Abstract

The rapid development of portable electronics, electric vehicles, and renewable energy systems has heightened the demand for high-performance energy storage devices. In this study, a trimetallic Ni–Co–Ce coordination framework (CF) was successfully synthesized via a simple hydrothermal method and directly deposited onto nickel foam as an electrode for supercapacitor applications. Structural and morphological characterization revealed a hierarchical architecture of oval-shaped microcrystals decorated with chestnut-like protrusions, providing abundant electroactive sites and facilitating efficient ion transport. Electrochemical measurements, including cyclic voltammetry and galvanostatic charge-discharge tests, demonstrated moderate capacitive behavior with specific capacitances increasing from 0.74 F/g to 2.6 F/g over successive cycles. Although Coulombic efficiency decreased from 23.5% to 11.6%, the incorporation of Ce enhanced structural stability and improved electron transport within the framework. These results suggest that Ni-Co-Ce coordination frameworks are promising candidates for supercapacitor applications, and further optimization of material composition and cycling conditions may lead to improved energy storage performance.

Keywords: Coordination Frameworks; Coordination Polymers; Nickel Foam Electrodes; Supercapacitors; Hydrothermal Synthesis.

1. Introduction

The rapid growth of portable electronics, electric vehicles, and renewable energy technologies has created an increasing demand for high-performance energy storage devices [1]. Supercapacitors, also known as electrochemical capacitors, have attracted significant attention due to their high-power density, long cycle life, and fast charge–discharge capability [2]. Unlike batteries, which store energy through slow faradaic reactions, supercapacitors combine electrostatic and

* Corresponding author.
Email address: jarrahiz@yahoo.com (Z. Jarrahi)

Received 24 October 2025
Revised 12 December 2025
Accepted 14 December 2025
Available online 18 December 2025

https://doi.org/10.22034/jams.2025.210154
© 2025 The Authors. This article is licensed under a Creative Commons Attribution 4.0 International License.

faradaic charge storage mechanisms, offering rapid energy delivery and excellent cycling stability [3]. The performance of supercapacitors is highly dependent on the electrode materials, which must exhibit high electrical conductivity, large surface area, and abundant electroactive sites [4].

Coordination frameworks (CFs), a broader class that includes coordination frameworks (CFs), have emerged as promising materials for energy storage applications due to their tunable porosity, structural diversity, and the possibility to incorporate multiple metal centers [5]. Among transition-metal-based systems, Ni-Co coordination frameworks have demonstrated outstanding electrochemical properties owing to the synergistic redox activity of nickel and cobalt ions [6]. The introduction of a third metal, such as cerium (Ce), into the Ni-Co coordination network can further enhance structural stability, facilitate electron transfer, and improve specific capacitance.

Recent studies have shown that Ni-Co-based coordination frameworks (CFs) exhibit high capacitance, good rate capability, and long-term cycling stability [7]. However, despite their promising electrochemical properties, these materials often suffer from low intrinsic electrical conductivity and limited structural stability during repeated charge-discharge cycling, which can restrict their practical applicability [8]. Incorporating Ce into the Ni-Co coordination network can alleviate these limitations by enhancing electron transport pathways and reinforcing the structural integrity of the framework through continuous and repeated cycling [9].

In this study, a trimetallic Ni-Co-Ce CF was synthesized via a simple hydrothermal method and deposited onto nickel foam as an electrode for supercapacitor applications. The structural, morphological, and electrochemical properties of the material were systematically investigated using FTIR, Raman, TEM, EDX, and electrochemical measurements, including charge-discharge cycling and specific capacitance tests.

2. Experimental

2.1. Materials

Nickel nitrate ($Ni(NO_3)_2 \cdot 6H_2O$), cobalt nitrate ($Co(NO_3)_2 \cdot 6H_2O$), cerium nitrate ($Ce(NO_3)_3 \cdot 6H_2O$), 1,3,5-benzenetricarboxylic acid (PTA, trimesic acid) as the organic linker, dimethylformamide (DMF), and sodium hydroxide (NaOH, 0.4 M) were purchased from commercial suppliers and used without further purification. Nickel foam (1 × 3 cm pieces) used as the substrate for electrode preparation was obtained from Redox Company. Polyvinylidene fluoride (PVDF) and N-methyl-2-pyrrolidone (NMP) were used as binder and solvent, respectively. Ethanol and deionized water were used for washing and cleaning purposes.

2.2. Hydrothermal Synthesis of Ni-Co-Ce Coordination Framework

The trimetallic Ni-Co-Ce CF was synthesized using a hydrothermal route. In a typical procedure, 0.083 g of PTA (1,3,5-benzenetricarboxylic acid, trimesic acid) as the organic linker, 0.0170 g of $Ni(NO_3)_2 \cdot 6H_2O$, 0.0210 g of $Co(NO_3)_2 \cdot 6H_2O$, and 0.0094 g of $Ce(NO_3)_3 \cdot 6H_2O$ were added to 10 mL of DMF under magnetic stirring for 30 minutes. During stirring, 1 mL of 0.4 M NaOH solution was added dropwise to the mixture. After complete mixing, the resulting solution was transferred into a Teflon-lined stainless-steel autoclave and maintained at 100°C for 12 hours. The product was then divided into three Falcon tubes and washed four times with a water–ethanol mixture, followed by three washes with deionized water under ultrasonication. Finally, the collected precipitate was dried in a watch glass at 50°C for 6 hours in an oven before further use.

2.3. Preparation of Ni-Co-Ce CF-Based Electrode

Nickel foam was used as a conductive substrate for the deposition of the synthesized Ni–Co–Ce CF. Prior to coating, the nickel foam pieces (1 × 3 cm) were thoroughly cleaned to remove surface impurities and enhance adhesion. The cleaning procedure involved ultrasonic washing in acetone for 15 minutes, immersion in a solution of 10 mL distilled water and 1 mL HCl for 15 minutes, followed by ultrasonic cleaning in an ethanol–water mixture for another 15 minutes. Finally, the foams were dried in an oven at 50–60°C for 30 minutes.

The electrode paste was prepared by mixing 80 wt% of the Ni-Co-Ce CF as the active material, 10 wt% polyvinylidene fluoride (PVDF) as the binder, and 10 wt% conductive carbon black. The binder solution was obtained by dissolving PVDF in N-methyl-2-pyrrolidone (NMP) with a weight ratio of 1.25% PVDF to 98.75% NMP. The components were thoroughly

© 2025 The Authors. This article is licensed under a Creative Commons Attribution 4.0 International License.

mixed to form a uniform and viscous paste suitable for coating.

The prepared paste was uniformly applied onto both sides of the cleaned nickel foam using tweezers to ensure good coverage and electrical contact. The coated samples were then dried in an oven at 50°C for 3 hours to remove residual solvent and achieve firm adhesion. The resulting Ni-Co-Ce CF-based nickel foam electrodes were directly employed for structural and electrochemical characterizations.

2.4. Measurements

The morphological and compositional properties of the synthesized Ni-Co-Ce CF were systematically investigated. Scanning electron microscopy (SEM, MIRA3-TESCAN) was employed to observe the surface morphology, particle size, and uniformity of the CF coating on the nickel foam substrate. Energy-dispersive X-ray spectroscopy (EDX, TESCAN MIRA 3 LMU) was used to determine the elemental composition and to confirm the successful incorporation and homogeneous distribution of Ni, Co, and Ce elements within the framework. Furthermore, the electrochemical performance of the prepared electrodes was evaluated through galvanostatic charge-discharge (GCD) tests and specific capacitance measurements, using a RADSTAT 30, which provided insight into the charge storage capability, reversibility, and stability of the Ni–Co–Ce CF electrodes for potential applications in supercapacitors. Electrochemical measurements were carried out in a three-electrode system using 1 M KOH as the electrolyte. A Ni-Co-Ce CF-coated nickel foam served as the working electrode, with graphite as the reference electrode and platinum as the counter electrode. Cyclic voltammetry (CV) was performed within a potential window of 0-0.5 V at scan rates ranging from 5 to 50 mV s^{-1}, while galvanostatic charge-discharge (GCD) tests were conducted at current densities of 0.05-2 mA g^{-1}. These conditions ensure reproducibility and consistent evaluation of the electrode's electrochemical performance.

3. Results and discussion

3.1. Structural Characterization via X-ray Diffraction (XRD)

The crystalline structure of the synthesized Ni-Co-Ce CF was analyzed using XRD, and the diffraction pattern is presented in Figure 1. The main characteristic peaks are observed at 2θ values of 22.3°, 28.7°, 33.2°, 47.9°, 53.3°, and 56.5°. These sharp and well-defined peaks confirm the successful formation of a highly crystalline trimetallic Ni-Co-Ce CF framework. The presence of six main reflections indicates a well-ordered crystalline structure, reflecting the uniform incorporation of Ni, Co,

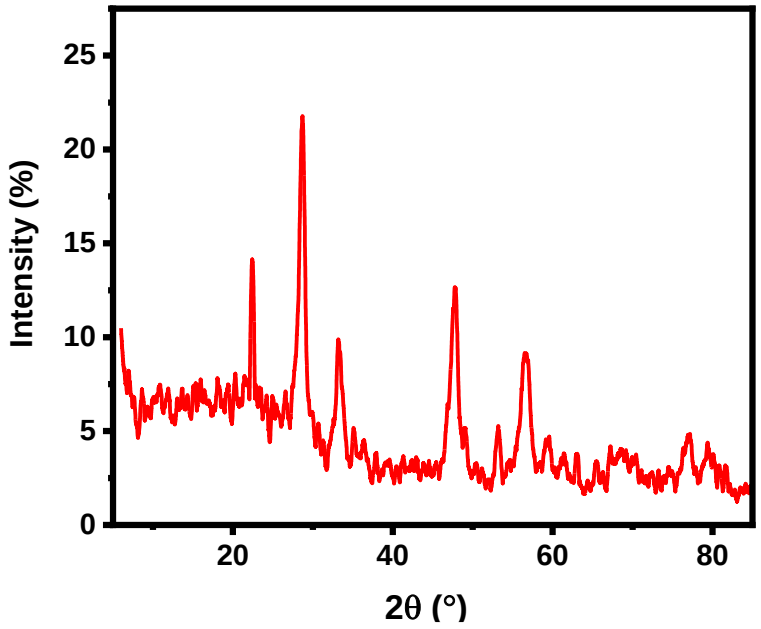

Figure 1. XRD pattern of the as-synthesized Ni-Co-Ce CF, confirming its crystalline structure.

© 2025 The Authors. This article is licensed under a Creative Commons Attribution 4.0 International License.

and Ce within the CF. It is noteworthy that the formation of CF alters the local coordination environment of the metal ions compared to their pure metal or oxide forms. Coordination with organic linkers results in the observed diffraction pattern, which is consistent with reported Ni-Co-based CFs and the expected contribution of Ce. The absence of peak broadening suggests a high degree of crystallinity, which supports the structural stability of the synthesized CF. Overall, the XRD analysis confirms that the synthesized Ni-Co-Ce CF possesses a stable and highly crystalline framework, suitable for application as an electrode material in supercapacitors.

3.2. Morphological and Elemental Analysis

The surface morphology of the synthesized Ni-Co-Ce CF was examined using SEM to gain insight into its structural characteristics relevant to electrochemical performance. As shown in Figure 2, the material exhibits a dual hierarchical morphology. The primary structure consists of relatively large, well-defined oval-shaped crystals with smooth and dense surfaces, typically in the range of 1-3 µm. This morphology reflects controlled crystal growth and strong coordination interactions between the metal centers and the organic linker during hydrothermal synthesis. In addition, the surfaces of these oval crystals are partially decorated with secondary chestnut-like protrusions, which are significantly smaller, typically 200-800 nm in size. These spiky nano-features increase the overall surface roughness and create a more open and interconnected architecture, which is beneficial for electrolyte penetration and ion transport. The presence of this hierarchical arrangement enables a greater number of electrochemically active sites while facilitating rapid

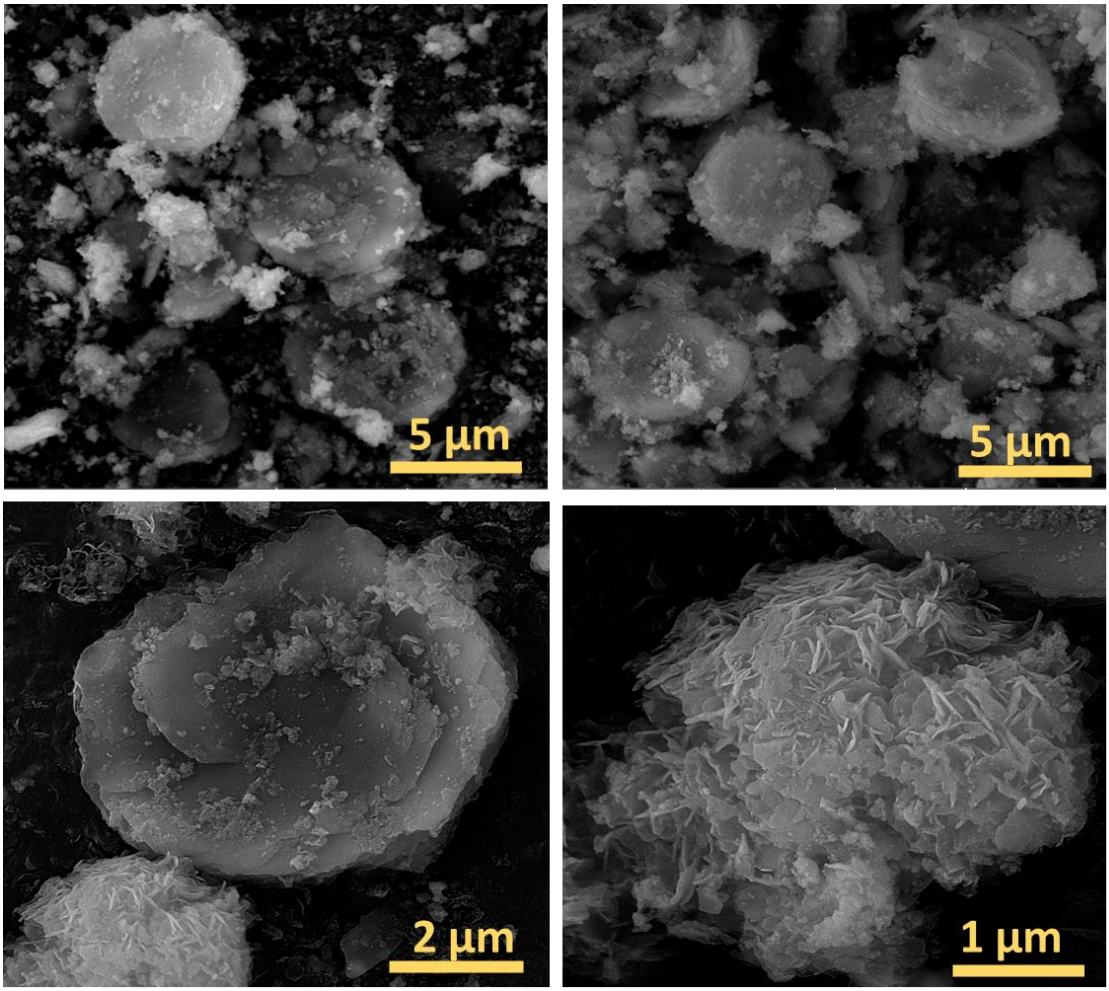

Figure 2. SEM images of the synthesized Ni-Co-Ce CF at different magnifications.

© 2025 The Authors. This article is licensed under a Creative Commons Attribution 4.0 International License.

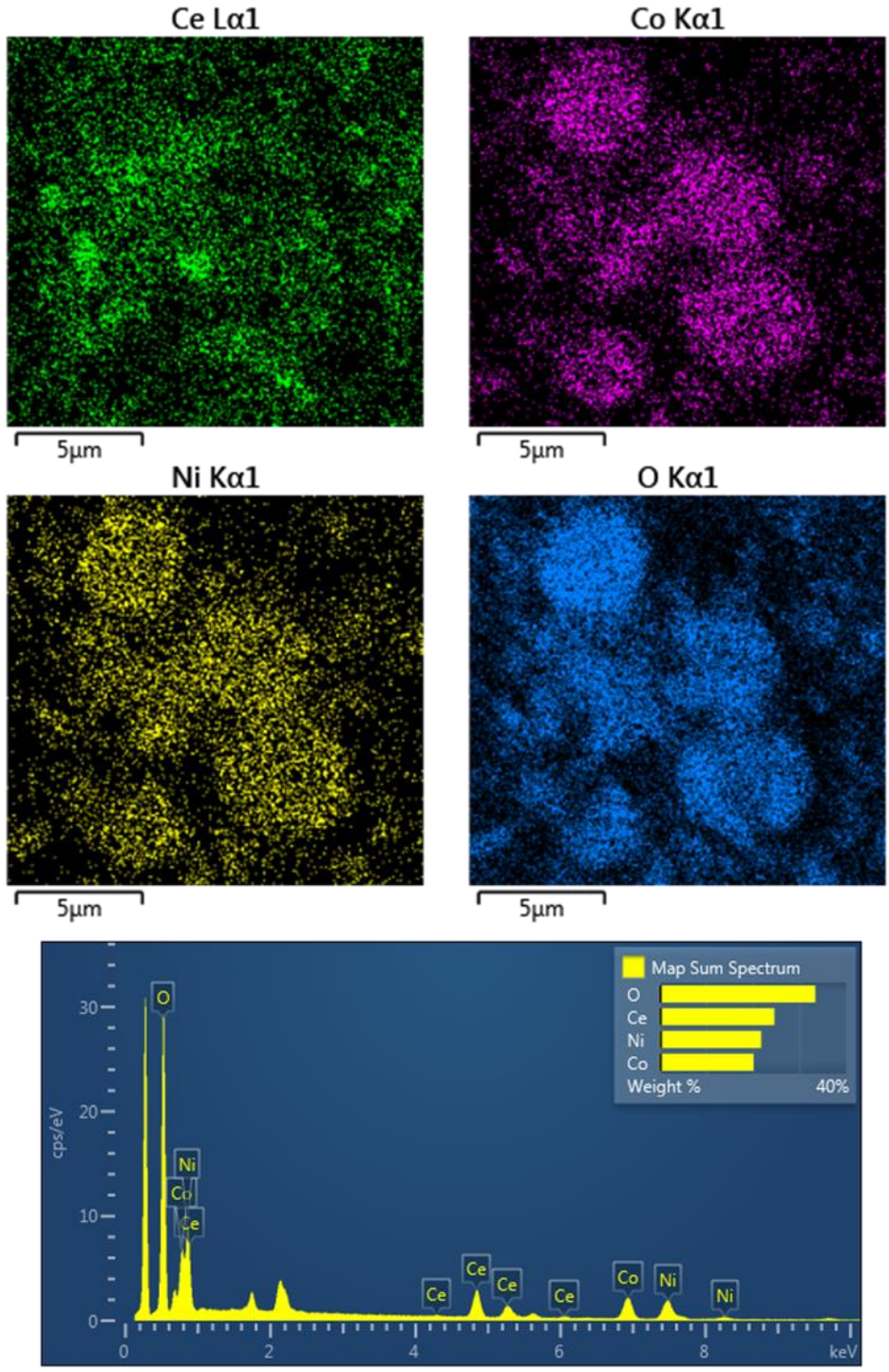

Figure 3. EDX spectrum and elemental mapping of Ni-Co-Ce CF, showing uniform distribution of Ni, Co, Ce, and O, confirming successful Ce incorporation and a hierarchical structure with abundant electroactive.

electrolyte ion diffusion and efficient charge transfer pathways throughout the structure. This morphology was previously reported for bimetallic Ni-Co metal organic frameworks by Jihwa Hong et al [10]. However,

© 2025 The Authors. This article is licensed under a Creative Commons Attribution 4.0 International License.

the introduction of Ce into the Ni-Co metal node configuration results in noticeable modifications to crystal evolution. The Ce^{3+}/Ce^{4+} redox couple promotes defect formation and heterogeneous nucleation, which enhances the density and distribution of the spiky surface features. This contributes to a larger exposed electroactive area and improves charge transport pathways within the electrode.

The elemental composition of the synthesized Ni-Co-Ce CF was analyzed using EDX, and the results are presented in Figure 3. The spectrum confirms the presence of Ni, Co, Ce, and O, in addition to C from the organic linker, verifying the successful incorporation of Ce into the Ni-Co CF framework. Quantitatively, the weight percentages are 21.82% Ni, 20.15% Co, 24.62% Ce, and 33.40% O. The high atomic fraction of oxygen is consistent with the presence of the organic ligands. Elemental mapping further reveals a uniform distribution of Ni, Co, and Ce throughout the CF structure, consistent with SEM observations of homogeneous oval-shaped microcrystals decorated with chestnut-like protrusions. The even dispersion of these metal components, combined with the hierarchical morphology, ensures a high density of electrochemically active sites. The incorporation of Ce not only contributes additional redox-active centers but also appears to stabilize the CF framework, supporting structural integrity and providing an open architecture favorable for supercapacitor applications.

3.3. Electrochemical Analysis of the Ni-Co-Ce CF Electrode

The electrochemical performance of the synthesized Ni-Co-Ce CF electrodes was systematically evaluated using cyclic voltammetry (CV) and galvanostatic charge-discharge (GCD) measurements. The CV curves (Figure 4) exhibit distinct redox peaks, indicating reversible faradaic reactions associated with the Ni and Co species in the electrode. The CV curves of the Ni-Co-Ce CF electrode exhibit quasi-rectangular shapes with broad redox peaks, indicating a combination of electric double-layer capacitance and pseudocapacitive behavior. Scans 1 and 2 show relatively lower peak currents, suggesting that the electrode requires additional cycles to reach its maximum electrochemical activity. In contrast, Scans 3 and 4 display higher current densities and more pronounced redox peaks, reflecting enhanced charge storage resulting from improved ion accessibility and an optimized electrode structure. Among the four scans, Scan 4 demonstrates the highest current response, reaching peak currents of approximately 1.64 mA, significantly higher than those observed in Scans 1–3. This enhancement indicates more efficient charge storage capability and improved electrochemical activity for this particular sample. The gradual increase in peak current with successive scans suggests favorable kinetics and enhanced ion transport within the CF structure.

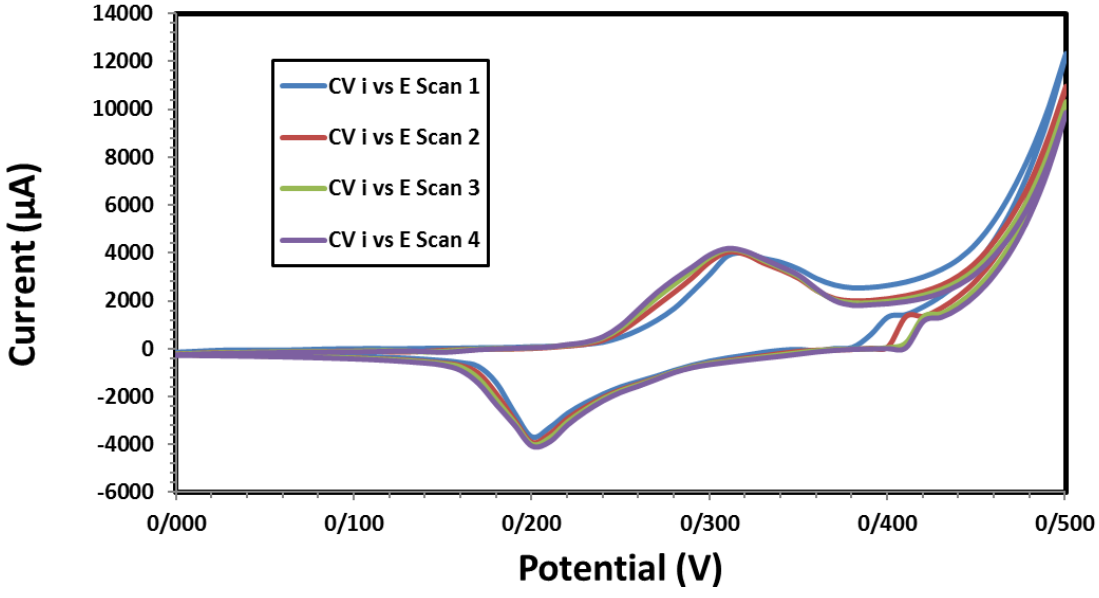

Figure 4. Cyclic voltammetry (CV) curves of the Ni-Co-Ce CF electrode at four successive scans.

© 2025 The Authors. This article is licensed under a Creative Commons Attribution 4.0 International License.

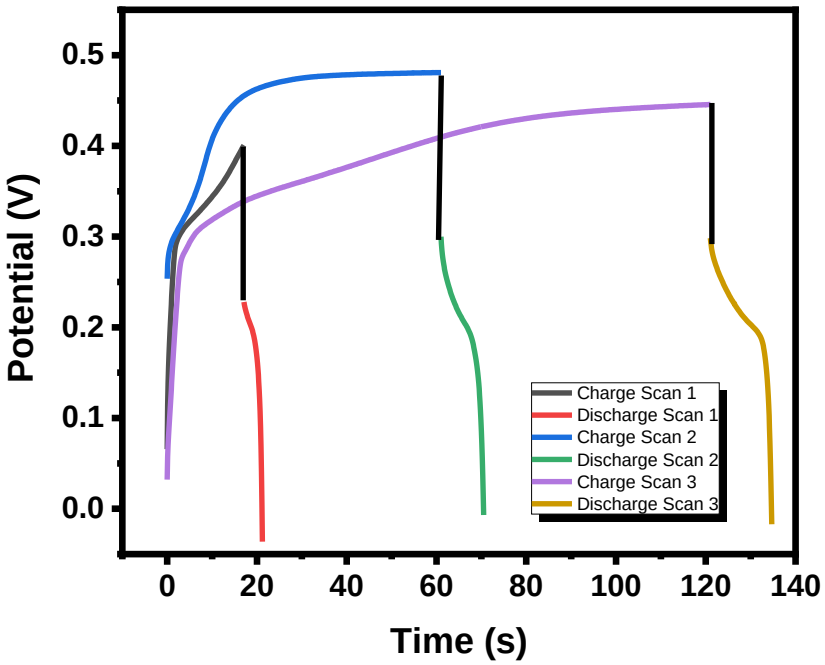

Figure 5. Galvanostatic charge-discharge (GCD) curves of the synthesized Ni-Co-Ce CF-based supercapacitor at three different scan rates.

The galvanostatic charge-discharge (GCD) results of the Ni-Co-Ce CF electrode are presented in Figure 5, with the corresponding specific capacitance and Coulombic efficiency summarized in Table 1. The charge-discharge curves were used to evaluate the electrode's specific capacitance and energy storage efficiency, considering an active material mass of 0.15 g.

The specific capacitance (C_S) was calculated using the equation:

$$C_S = \frac{I.\Delta t}{m.\Delta V} \quad (1)$$

where I is the discharge current (A), Δt is the discharge time (s), m = 0.015 g is the mass of the active material, and $\Delta V \approx$ 0.5 V is the voltage window.

The charge-discharge analysis of the electrode demonstrates a progressive increase in both charge and discharge times across the three scans. Specifically, the discharge time increases from 4 s in Scan 1 to 14 s in Scan 3, indicating a gradual enhancement in the electrode's ability to store charge. Correspondingly, the specific capacitance (Cs) rises from 0.74 F/g to 2.6 F/g, reflecting improved charge storage with longer cycling.

However, the Coulombic efficiency shows a decreasing trend, dropping from 23.5% in Scan 1 to 11.6% in Scan 3. This decline suggests that although the electrode can store more charge at longer charge-discharge durations, energy losses during cycling increase, possibly due to resistive losses or side reactions. Overall, these results indicate that the electrode exhibits moderate capacitive behavior with relatively low efficiency, and optimization of the electrode material or electrolyte may be necessary to enhance reversibility and energy retention.

Table 1. Charge-discharge data, specific capacitance, and Coulombic efficiency of the Ni-Co-Ce CF electrode over three successive scans

Scan	Charge Time (s)	Discharge Time (s)	Specific Capacitance Cs (F/g)	Coulombic Efficiency (%)
1	17	4	0.74	23.5
2	61	9.5	1.76	15.6
3	121	14	2.6	11.6

© 2025 The Authors. This article is licensed under a Creative Commons Attribution 4.0 International License.

4. Conclusions

In summary, a trimetallic Ni-Co-Ce CF was successfully synthesized and employed as an electrode for supercapacitor applications. SEM and EDX analyses confirmed a hierarchical micro/nano-structured morphology with uniform distribution of Ni, Co, and Ce, providing numerous electroactive sites and favorable pathways for ion diffusion. Electrochemical studies revealed that the electrode exhibits increasing specific capacitance with prolonged cycling, reaching 0.28 F/g, though Coulombic efficiency decreased, indicating energy losses during charge–discharge cycles. The introduction of Ce contributed to enhanced structural stability and electron transport, mitigating some limitations of conventional Ni-Co CFs. Overall, the study demonstrates the potential of trimetallic CF electrodes for high-performance supercapacitors and provides a foundation for further optimization to achieve higher efficiency and long-term stability.

Conflict of Interest

The authors declare no conflict of interest.

References

1. A. Aghmadi and O.A. Mohammed. Energy storage systems: technologies and high-power applications. *Batteries*, **2024**, *10*, 141.
2. Y.M. Volfkovich. Electrochemical supercapacitors (a review). *Russian Journal of Electrochemistry*, **2021**, *57*, 311.
3. S.Y. Attia, et al. Supercapacitor electrode materials: addressing challenges in mechanism and charge storage. *Reviews in Inorganic Chemistry*, **2022**, *42*, 53.
4. P. Forouzandeh, V. Kumaravel, and S.C. Pillai. Electrode materials for supercapacitors: a review of recent advances. *Catalysts*, **2020**, *10*, 969.
5. H. Laeim, et al. Porosity tunable metal-organic framework (MOF)-based composites for energy storage applications: recent progress. *Polymers*, **2025**, *17*, 130.
6. S. Li, et al. Transition metal-based bimetallic MOFs and MOF-derived catalysts for electrochemical oxygen evolution reaction. *Energy & Environmental Science*, **2021**, *14*, 1897.
7. X. Hang, et al. From Co-MOF to CoNi-MOF to Ni-MOF: a facile synthesis of 1D micro-/nanomaterials. *Inorganic chemistry*, **2021**, *60*, 13168.
8. G. Xu, C. Zhu, and G. Gao. Recent progress of advanced conductive metal–organic frameworks: precise synthesis, electrochemical energy storage applications, and future challenges. *Small*, **2022**, *18*, 2203140.
9. Z. Hu, Y. Wang, and D. Zhao. The chemistry and applications of hafnium and cerium (IV) metal–organic frameworks. *Chemical Society Reviews*, **2021**, *50*, 4629.
10. J. Hong, S.-J. Park, and S. Kim. Synthesis and electrochemical characterization of nanostructured Ni-Co-MOF/graphene oxide composites as capacitor electrodes. *Electrochimica Acta*, **2019**, *311*, 62.

© 2025 The Authors. Authors retain the copyright and full publishing rights. This article is licensed under a Creative Commons Attribution 4.0 BY International License.

© 2025 The Authors. This article is licensed under a Creative Commons Attribution 4.0 International License.

Fabrication, Testing, and Optimization of MWCNT Epoxy Polymer Nanocomposites Through Taguchi, TOPSIS, and Response Surface Techniques

Dauson Nyonyi [a,b,*], V.V.S. Prasad [a], P. Swapna [c], M.V. Naga Sankaram [a]

[a] *Department of Marine Engineering, College of Engineering, Andhra University, Visakhapatnam, India*

[b] *Department of Marine, Oil and Gas Engineering, National Institute of Transport, Dar es Salaam, Tanzania*

[c] *Department of Instrument Technology, College of Engineering, Andhra University, Visakhapatnam, India*

Editor's note: The optimization of nanocomposites with different volume fractions of nanofillers is a classic multi-criteria decision-making challenge. Nyonyi et al. introduced a hybrid decision-making approach that combines Taguchi methods, TOPSIS, and Response Surface Methodology (RSM) to identify the most effective nanocomposite. This innovative approach successfully improved the mechanical properties of epoxy-E-fiberglass nanocomposites reinforced with multi-walled carbon nanotubes (MWCNTs). The optimization results confirmed that the content ratios of MWCNTs and other components in the system significantly affect both tensile and flexural strength.

doi: 10.22034/jams.2025.210155

How to cite: D. Nyonyi et al. *Journal of Applied Material Science*, **2025**, *1*, 210155.

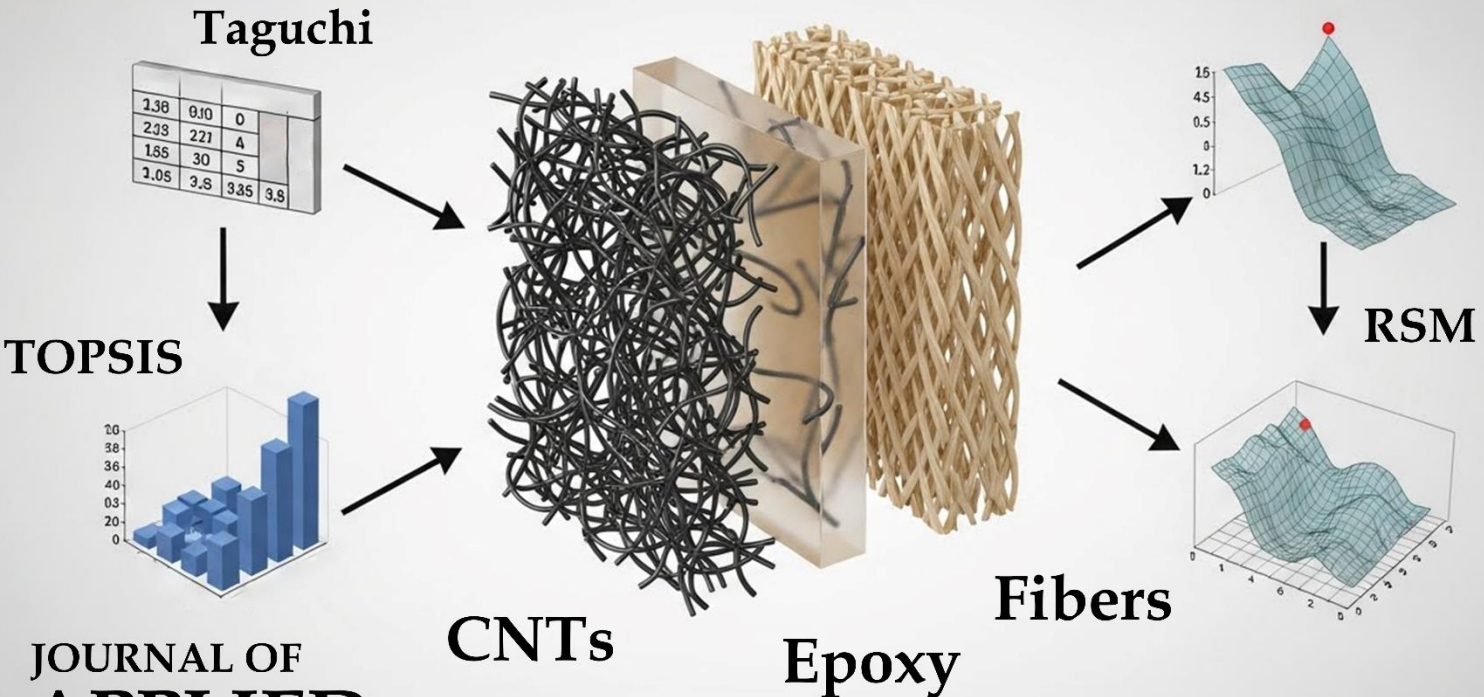

JOURNAL OF
APPLIED
MATERIAL
SCIENCE
jams.hsu.ac.ir

© 2025 *J. Appl. Mater. Sci.* This material is licensed under a Creative Commons Attribution 4.0 International License.

Journal of Applied Material Science **2025**, *1*, 210155
How to cite: D. Nyonyi et al., *Journal of Applied Material Science*, **2025**, *1*, 210155.
Journal homepage: **jams.hsu.ac.ir**

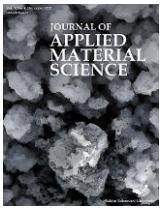

Original Research

Fabrication, Testing, and Optimization of MWCNT Epoxy Polymer Nanocomposites Through Taguchi, TOPSIS, and Response Surface Techniques

Dauson Nyonyi [a,b,*], V.V.S. Prasad [a], P. Swapna [c], M.V. Naga Sankaram [a]

[a] *Department of Marine Engineering, College of Engineering, Andhra University, Visakhapatnam, India*

[b] *Department of Marine, Oil and Gas Engineering, National Institute of Transport, Dar es Salaam, Tanzania*

[c] *Department of Instrument Technology, College of Engineering, Andhra University, Visakhapatnam, India*

Abstract

The mechanical optimization of nanocomposites, which involves different nanofillers and varying nanofiller volume fractions, represents a classic, multi-criteria decision challenge. In practical scenarios, the values of attributes and their corresponding weights frequently exhibit uncertainty, leading to certain constraints. This study presents a novel hybrid decision-making approach that integrates Taguchi, Technique for Order Preference by Similarity to Ideal Solution (TOPSIS), and Response Surface Methodology (RSM) to identify the nanocomposite with optimal mechanical properties. This study explores the enhanced mechanical properties of nanocomposites reinforced with multi-walled carbon nanotubes (MWCNTs) and epoxy-E-fiberglass. The parameters assessed consist of tensile strength, tensile modulus, tensile strain at break, flexural strength, flexural modulus, and flexural strain at break. The input variables used to improve the mechanical properties of the nanocomposite samples include MWCNT (vol%) nanofiller, e-glass fiber, and epoxy polymer. The Taguchi method was applied to design an experiment that studied the interaction of the process on the response variables of the samples. The TOPSIS technique and response surface methodology (RSM) analyses were employed for the simultaneous optimization and ranking of multiple responses. After determining the optimal settings for the control factors, confirmation experiments were conducted to validate the results. The TOPSIS analysis ranked the experiments, with experiment code A22 identified as having the most significant effect, followed by A88, A11, and A55, in that order. Taguchi and RSM indicated that experiment code A44 achieved optimal mechanical properties. Therefore, the results demonstrate that the mechanical properties of MWCNT nanocomposites have been optimized.

Keywords: Optimization; Taguchi; Surface Response; Mechanical Strength; Nanocomposites.

* Corresponding author.
Email address: dnyonyi.rs@andhrauniversity.edu.in (D. Nyonyi)

Received 3 December 2025
Revised 16 December 2025
Accepted 19 December 2025
Available online 20 December 2025

https://doi.org/10.22034/jams.2025.210155
© 2025 The Authors. This article is licensed under a Creative Commons Attribution 4.0 International License.

1. Introduction

The use of nanocomposite materials has come about because of improvements in transportation and infrastructure. To make nanocomposites, you have to mix nanotubes or nanoparticles into a composite matrix. This combines the ideas of composites with the nanometer-scale range, which is from 1 nm to 100 nm [1]. The goal is to change the composite structure at the atomic, molecular, and supramolecular levels to make it more stable, better at conducting electricity, and better at holding together, while keeping the interface stable so that materials can be made [2]. The small size of the nanofillers and the chemical interactions that happen at the interface of nanoparticle/nanotube-matrix provide nanocomposites with unique and better properties [3].

Carbon nanotubes (CNTs) are viewed as promising for enhancing polymer matrices because of their exceptional strength, stiffness, lightweight nature, high flexibility, diameter-dependent specific surface area, high aspect ratio, excellent thermal conductivity, and electrical properties, including moderate electrostatic discharge capabilities [1, 4, 5]. Their outstanding mechanical and thermal attributes make CNTs highly appealing nanofiller materials, making them suitable for manufacturing multifunctional polymer nanocomposites. Besides the type and surface functionalization of CNTs, the properties of the polymer matrix, stabilization additives, and production processes significantly influence the maximum CNT load and the resulting composite properties [2, 6].

The literature examines diverse methodologies for the design and fabrication of nanocomposites, leading to varying degrees of interfacial contact and mechanical strength characteristics. The investigation carried out by Miraidin et al used dispersion and surface modification methods to make MWCNT/epoxy composites work better mechanically by aligning the MWCNTs in the polymer resin [7]. This made it easier for the MWCNTs to stick to the epoxy polymer matrix. It is essential to improve mechanical strength and deal with the problems that come up during synthesis and the clumps that intermolecular Van der Waals forces cause. The suggested solutions are meant to stop agglomerations and voids from forming in the composite. This will make the MWCNTs spread out better in the polymer matrix and make the nanocomposite's mechanical qualities better [8]. Some researchers, however, consider the formation of agglomeration in the nanocomposite this be an essential issue that hasn't been answered, in addition to the problems with the surface functionalization of MWCNTs nanomaterials [7].

The research conducted by Sharma. S et al. underscores the persistent obstacles related to morphological structures that could affect the structural stability and lead to fracture formation; these issues were substantially alleviated with the implementation of bulk polymerization and sonication during the MWCNT dispersion process [9]. However, the improvement of mechanical qualities has not yet been accomplished. Some writers say that ball milling or chemical treatment can change the surface of MWCNTs. [8]. Chemical functionalization methods, including amino functionalization, oxidation, fluorination, and surface modification, can make the dispersion process faster, improve processing efficiency, and make MWCNTs work better with polymers. This procedure cannot improve the strength and modulus of the polymer nanocomposites [10]. The current literature suggests a need for more research into the enhancement of MWCNT nanocomposite optimization techniques.

There are various types of optimization techniques used to fine-tune parameters in nanocomposite manufacturing with multiple quality features, which often depend on the researcher's judgment and experience [11]. Since different quality characteristics may require unique optimal parameter sets, these must be combined to determine the final parameter combination for product design or system and process optimization [12]. The nanocomposite fabrication study, conducted using the Taguchi method, aimed to optimize a single quality by varying process parameters, including carbon nanotube powder and resin adhesive. These results were then combined with Response Surface Methods and TOPSIS for multi-quality optimization to identify the best parameter set for the fabric [13-15]. The approach also included response analysis to evaluate how each factor influenced different quality characteristics.

This research examines three additional techniques to augment the mechanical strength of nanocomposites, which encompass the interaction of three elements: a certain volume fraction of MWCNTs, e-fiberglass, and an epoxy polymer matrix (comprising resin and hardener). The study employs several Taguchi methodologies for experimental design, response surface methodology (RSM) utilizing Minitab software, and TOPSIS analysis to optimize and evaluate the performance of the nanocomposite.

© 2025 The Authors. This article is licensed under a Creative Commons Attribution 4.0 International License.

2. Experimental

2.1. Materials

The polymer matrix consisted of a 600 g E-glass fiberglass woven roving mat (density 2.5 g/cm^3) and epoxy resin (LY556), along with a hardener (HY951). Multi-walled carbon nanotubes (MWCNT) had a purity exceeding 98% (information taken from the supplier's data sheet). The vacuum bagging kit system and the vacuum pump system were all sourced from local Indian suppliers.

2.2. Taguchi Experimental Design (TED) Set-Up

Three experiments were conducted employing the Taguchi design of experiments (DOE) methodology, one for each factorial experiment listed in Table 1. The experiment was structured to incorporate three input variables: the MWNT (vol%) nanofiller, epoxy polymer (resin (LY551) and hardener (HY956)), and E-glass fiber [5]. These methods employ analysis of variance (ANOVA) and the signal-to-noise ratio (S/N) to examine the results and the interactions among various parameters. These methods effectively distinguish the critical factors influencing the reaction from the less significant ones, ensuring the optimal settings are identified to get superior results. Minitab was employed to design the experiments and analyze the outcomes.

Table 1. Input parameter and variation level

Parameter input Factors	Level		
	1	2	3
MWCNT content (Vol%)	1.0	1.5	2
Epoxy polymer matrix (Vol)	56	64	72
E-glass Fiber(gm)	60	70	80

2.3. Sample Preparation and Fabrication

The different laminate specimens were manufactured using vacuum bagging techniques (VBT). The fabrication sequence was based on an orthogonal array of designed experiments, as shown in Table 2. The protocol for the fabrication process was kept constant for all fabricated samples. After MWCNT surface modification and proper dispersion mixing, the epoxy polymer with MWCNT was stirred using a magnetic stirrer for 10 minutes, followed by probe sonication for 5 minutes under control of the exothermal temperature. The hand layup technique was used to apply an MWCNT-epoxy polymer matrix (a mix of resin and hardener) to each layer of the E-glass fiber mat, thereby forming a laminate. This laminate instant was transferred to a vacuum bagging-enclosed system and cured under an atmospheric pressure of 700 bar and room temperature for 24 hours [16, 17].

The manufacturing of E-glass fiber polymer nanocomposites involves adding a small volume fraction of multi-walled carbon nanotubes (MWCNTs) to various amounts of the polymer matrices, as shown in Table 2. The main goal is to evenly distribute the MWCNTs and achieve uniform dispersion within the bonding mechanisms of the polymer matrices—novel approaches for creating high-strength MWCNT E-glass fiber nanocomposite materials.

Table 2. Taguchi design experiments array

Exp. run	Exp. Code	E-Glass Fiber (gm)	Epoxy matrix (Resin Hardener)	MWCNT (Vol%)
1	A11	56	60	1.0
2	A22	56	70	1.5
3	A33	56	80	2.0
4	A44	64	60	1.5
5	A55	64	70	2.0
6	A66	64	80	1.0
7	A77	72	60	2.0
8	A88	72	70	1.0
9	A99	72	80	1.5

2.4. Response Surface Methodology

The response surface method (RMS) focuses on assessing the relationship between essential factors and the recorded response output. The principal benefit of employing RSM is that it enables the selective reduction of factors in a design of experiment, thereby effectively illustrating all potential influences on a system's response and optimizing it [18]. The mechanical testing results represent the proper response of a processing method, which is contingent upon critical factors related to the mechanical properties of the nanocomposite. The Minitab software tool will be employed to finalize the optimizations.

2.5. TOPSIS

The technique for order preference by similarity to ideal solution (TOPSIS) is a fundamental theory in ranking methods, determining the optimal choice as the one closest to the ideal solution and furthest from the

© 2025 The Authors. This article is licensed under a Creative Commons Attribution 4.0 International License.

least desirable option [19]. The assessment and ranking of the mechanical properties of the MWCNTs are performed using a detailed index that quantifies their deviation from the ideal solutions [14, 19]. The evaluation and categorization of the mechanical properties of the MWCNT results are conducted through a detailed index that considers their variances from the ideal solutions. The process involves several stages and numerical evaluations of TOPSIS, beginning with the ranking phase.

2.6. Measurements

The mechanical properties of the samples were tested under tensile, compression, bending, and impact loads. Tensile tests followed the ASTM D3039 standard at a crosshead speed of 1 mm/min using a Universal Testing Machine (UTM). The specimens were cut from a single laminate, measuring 20 mm in width, 2.5 mm in thickness, and 240 mm in length [20]. The gauge length was 100 mm, with a clamping length of 50 mm. Three specimens from each sample were tested. Flexural tests under three-point bending were also conducted on the UTM following ASTM D790 standards to determine flexural strength and modulus [20]. The crosshead moved at a steady speed of 2.0 mm/min, with a span-to-depth ratio of 16:1. Flexural strength was measured as the maximum stress at failure on the tensile side, averaged over three specimens. To achieve the objectives of optimization and prioritization, Taguchi, RSM, and TOPSIS were used to analyze the results of the extensive testing conducted [14, 15, 19].

The composite's crystal structures were analyzed using an X-ray diffractometer (XRD) with Cu-Kα radiation. A Shimadzu FTIR spectrometer was used for Fourier transform infrared spectroscopy to examine the interfacial interaction between the MWCNT and epoxy matrix in the specimen [21]. The morphological analysis of the MWCNT composites was conducted with an SEM (Tescan model MAIA3 XMH), and the results were gathered and analyzed to discover research insights.

3. Results and discussion

3.1. X-Ray Diffraction Analysis

XRD graphs of the MWCNT phase peak were obtained, confirming the presence of its components. The phase angle purity of MWCNT was analyzed using an XRD equipment through Cu Ka radiation constant (k = 1.542 Å). The MWCNT specimens, along with their composites (MWCNT/epoxy), were compacted into suitable glass molds equipped with pits for XRD analysis techniques [7]. The XRD diffraction phase

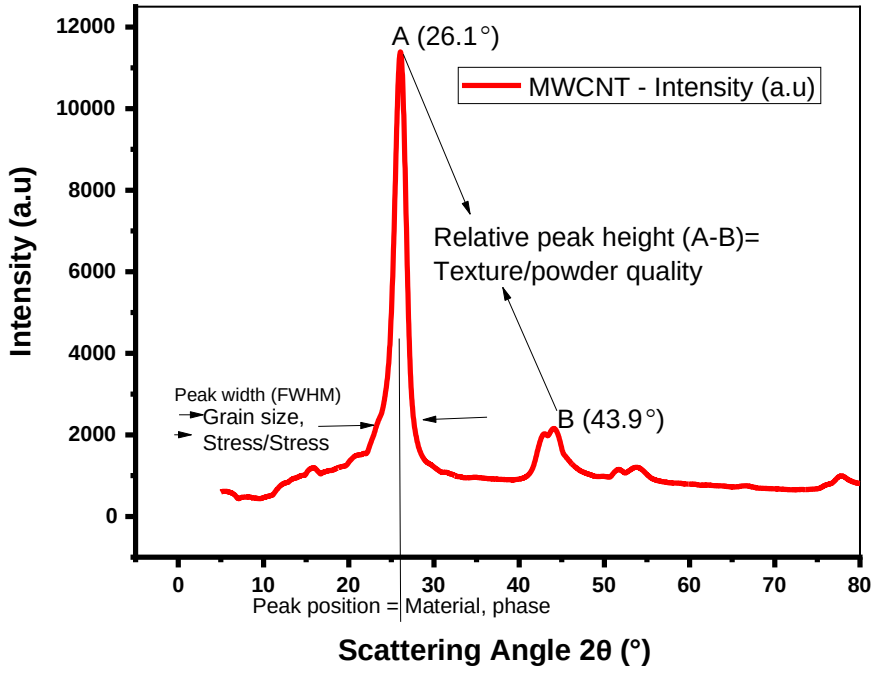

Figure 1. XRD Surface phase plot analysis.

© 2025 The Authors. This article is licensed under a Creative Commons Attribution 4.0 International License.

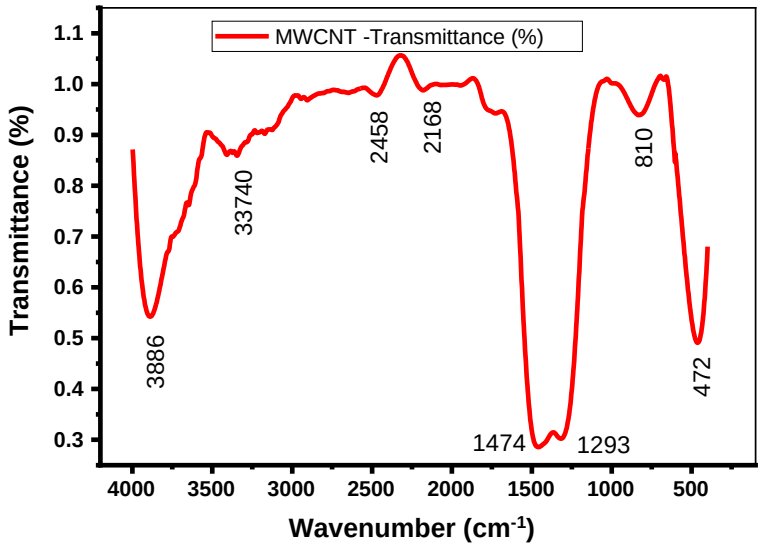

Figure 2. FTIR Sample Bond Plot.

sample plot (Figure 1) displays clear, high-pitched peaks that correspond to the crystal lattice parameters of (002) and (100) at a diffraction angle 2θ of 26.1° and 43.9 °. The size (d-spacing) of MWCNT was determined using the mathematical Debye-Scherrer formula (Equation 1):

$$d = k\frac{\lambda}{\beta \cos\phi} \quad (1)$$

where **d** is the average diameter of the crystallite, λ is the radioactivity wavelength (1.542 Å), β is the full width at half maxima, ∅ and β is Bragg's angle of corresponding peaks, shape constant k=0.9. The Crystallinity and crystal size of MWCNT were calculated to be 95.9% and 2.4 Å.

3.2. FTIR analysis

Figure 2 displays the FTIR spectrum, which provides information about the chemical composition, structure, and bonding of the MWCNT samples. The study is conducted at a resolution of 4 cm^{-1}, with an incident angle of 30°, and the wavenumber range from 200 to 800 cm^{-1} [21]. The presence of the unique band at 3374 cm^{-1}, which corresponds to the O–H stretch of terminal carboxyl groups, suggests the incorporation of polar functional groups, like (OH), on the surface of MWNT. The wavenumber maxima at 2458 cm^{-1} and 2168 cm^{-1} show the –C≡C– stretch, while the value at 1474 cm^{-1} shows the C-H bond. The fingerprint region, ranging from 1400 to 400 cm^{-1}, features peaks at 1293 cm^{-1}, 810 cm^{-1}, and 472 cm^{-1}, which signify the C-C stretching of the ring bond. The presence of these functional groups has been shown to improve the interfacial contact between MWNT and epoxy polymer.

3.3. Scanning Electron Microscopy (SEM) Analysis

The TESCAN model MAIA3 XMH, utilizing scanning electron microscopy, was used to examine the morphology and structure of MWCNT nanocomposites, yielding high-resolution images and comprehensive details regarding their surface structure [8]. The SEM analysis uncovers characteristics of the MWCNT nanocomposite, such as particle size, shape, lamination behavior, and arrangement, subsequent to mechanical testing. The examined surface characteristics included cracks, pores, and agglomeration [7, 8, 21]. Figure 3a displays SEM images that depict the failure of the specimen attributed to tensile stress, which arises from cracks within the MWCNT/epoxy matrix. Figure 3b illustrates the delineation between the MWCNT epoxy matrix and the E-glass fiber, in addition to instances of fiber fracture.

The micrographs of the MWCNT nanocomposite display significant clusters of resin, suggesting robust adhesion between the MWCNT/epoxy matrix and the fibers. Following the fracture, only slight debonding is observed between the glass fibers and the epoxy matrix, indicating a strong bond at the fiber-matrix interface. This feature is linked to the inclusion of MWCNT in the nanocomposite. Furthermore, the incorporation of

© 2025 The Authors. This article is licensed under a Creative Commons Attribution 4.0 International License.

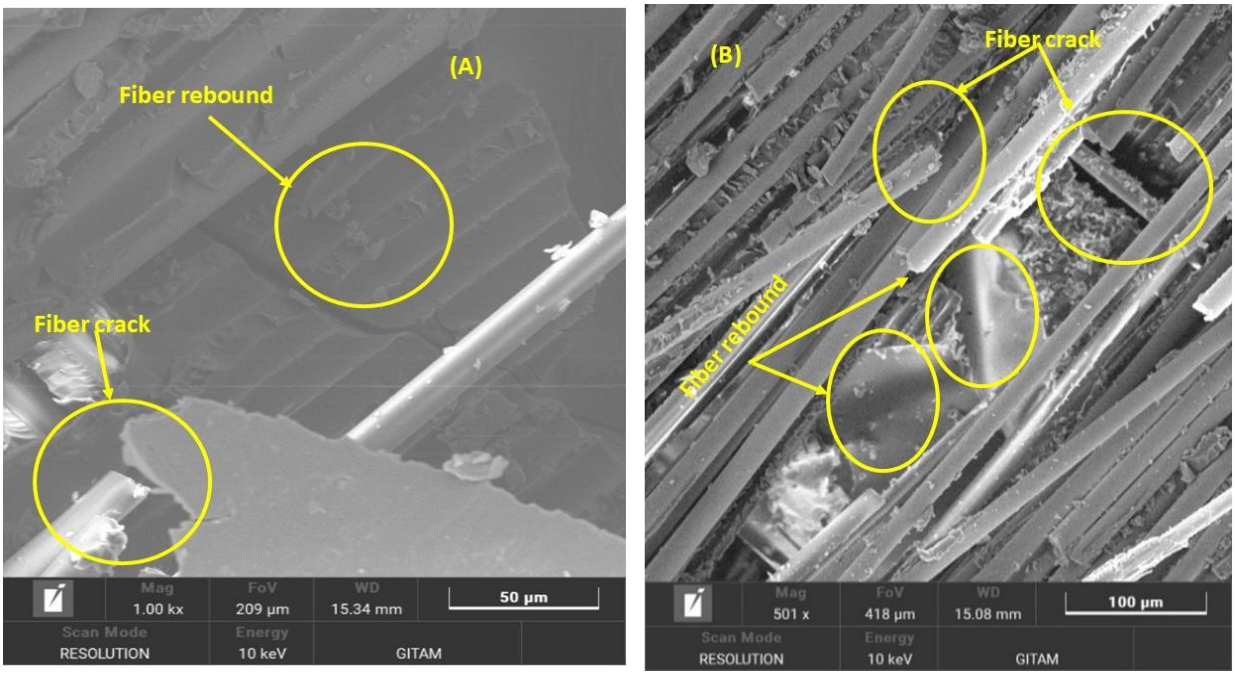

Figure 3. SEM images of the fracture surface of the MWCNT nanocomposite.

MWCNT nanofillers contributes to the mitigation of cracks and redirects crack propagation within the glass fiber-epoxy-MWCNT reinforced nanocomposites.

3.4. Mechanical Properties and TOPSIS Analysis

The fabricated samples of MWCNT nanocomposites underwent mechanical testing to evaluate their tensile properties, modulus of elasticity, flexural strength, and strain at break, following ASTM code standards. The tensile and flexural tests were performed using an Instron servo-hydraulic Universal Testing Machine model 8801 [17, 22]. The tensile test specifications are detailed in ASTM D3039, while the flexural testing guidelines are specified in ASTM D790, which employs a 3-point loading condition. This analysis encompassed a thorough application of the TOPSIS method to determine the rankings of alternative experiments based on their optimal mechanical performance.

The UTM tests performed in accordance with ASTM Standards for the mechanical properties of the MWCNT nanocomposite samples produced the following parameters: tensile strength, flexural strength, modulus of elasticity, and strain at break [22, 23]. The matrix result was normalized following the specified equation. Figure 4 presents the normalized decision matrix, where a weight value of 1.0 is uniformly applied across all parameters to demonstrate the mechanical properties of the nanocomposite.

$$r_{ij} = \frac{x_{ij}}{\sqrt{\sum_{i=1}^{n} x_{ij}}} \quad (2)$$

where r_{ij} is a normalized value, x_{ij} are the criterion values (i=1, 2, 3, …, n and j=1,2, 3, …, m).

$$D_i^{+} = \sqrt{\sum_{i=1}^{n} \left(y_{i_j}^{+} - y_{ij}\right)^2} \quad (3a)$$

$$D_i^{-} = \sqrt{\sum_{i=1}^{n} \left(y_{i_j}^{-} - y_{ij}\right)^2} \quad (3b)$$

where y_{ij}^{+} and y_{ij}^{-} are positive and negative ideal values selected from the normalized weighted matrix (V), D^{+} and D^{-} are the positive and Negative profit selection perspectives.

$$V_i = \frac{D_i^{-}}{D_i^{+} + D_i^{-}} \quad (4)$$

where V_i are the Euclidean distance values.

For both positive (+) and negative (-) ideal solutions, the Euclidean distance (D) was computed by applying the following equation (3). The results of this calculation are depicted in Figure 5. The rank, the preference value

© 2025 The Authors. This article is licensed under a Creative Commons Attribution 4.0 International License.

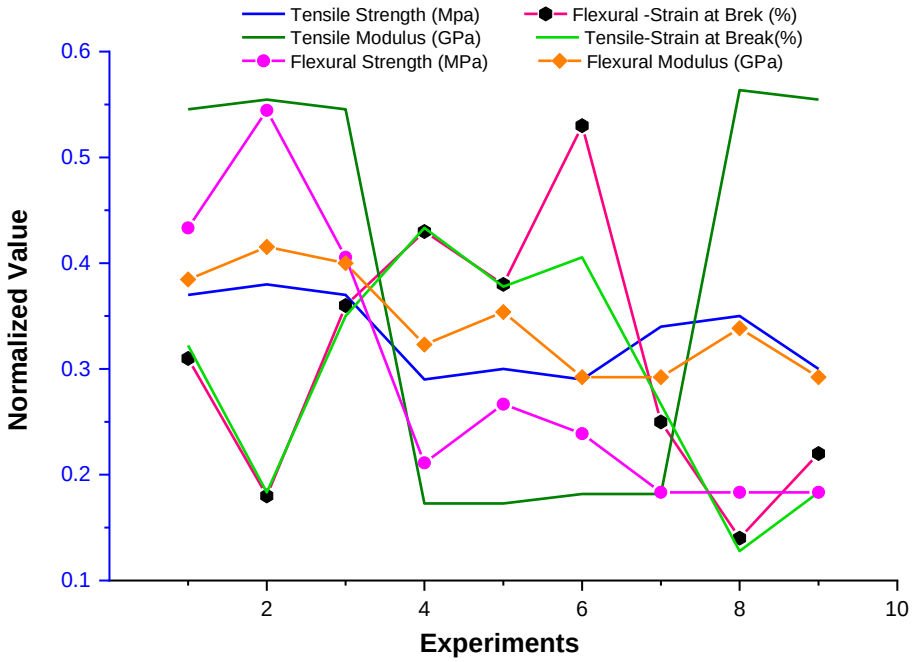

Figure 4. Normalized Decision Matrix.

(relative closeness), and the separation measure are all determined with the help of Equation 4, and the results are displayed in Figure 5. The ranking is determined by the preference value, with the highest possible closeness resulting in the highest possible rank [14, 19].

It was determined that experiment code A22, which was referred to in Table 2, was the most suitable alternative among the many MWCNT epoxy e-glass fiber-reinforced nanocomposite possibilities. This particular experiment had a constituent nanofiller concentration of 1.5 vol% MWCNT, 70 vol% epoxy polymer, and 72 g of E-glass fiber. In terms of mechanical performance, the experiment code A55 has been ranked the lowest, which indicates that it has the worst overall performance. For this experiment, the MWCNT concentration was set at 2 vol%, the epoxy polymer was set at 70 vol%, and the E-glass fiber was 64 g.

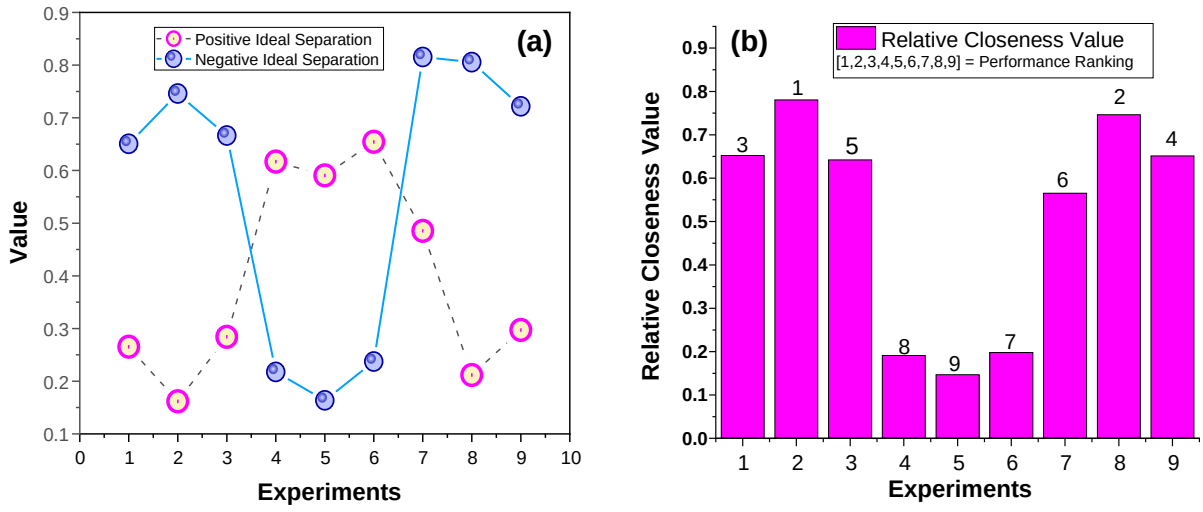

Figure 5. (a) Ideal Separation Distance. (b) Mechanical Performance Ranking.

© 2025 The Authors. This article is licensed under a Creative Commons Attribution 4.0 International License.

3.5. Determination of the Optimum Using the Taguchi Techniques.

The experiment's optimal design was evaluated through the analysis of a signal-to-noise (S/N) ratio to enhance mechanical strength properties. [24]. The objective evaluation of mechanical strength, including tensile, modulus, and flexural data, employed the "the larger is better" function. Conversely, the strain at break was assessed through the "nominal is better" function [25]. Figure 6 illustrates the impact of each parameter on tensile strength, flexural strength, modulus of elasticity, and strain. The ideal parameters for attaining maximum strength, as illustrated in Figure 6a, include an E-glass fiber content of 64 g, an epoxy polymer content of 60 vol%, and a MWCNT content of 1.5 vol%. This combination may yield the highest possible tensile strength, flexural strength, and Young's modulus [26].

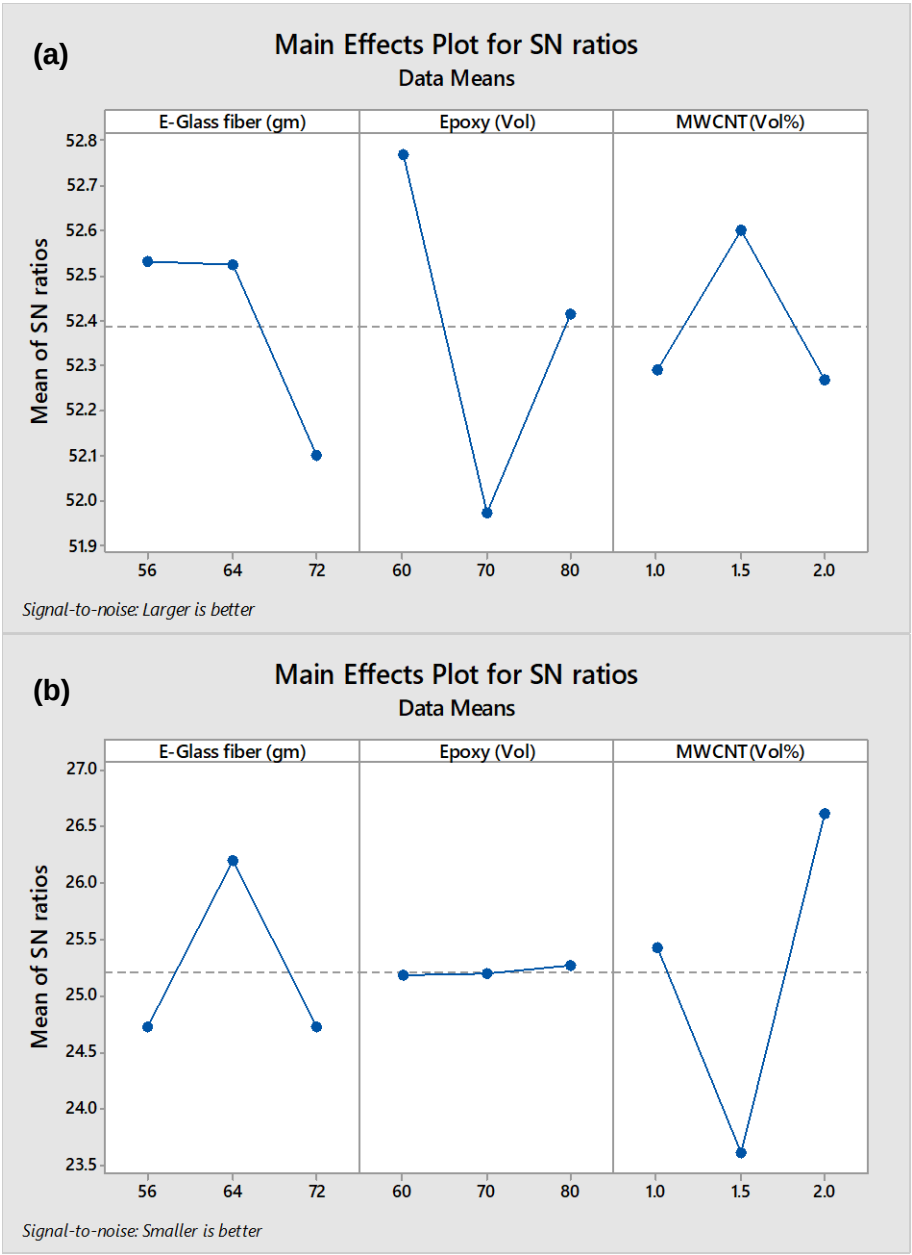

Figure 6. Taguchi Analysis: (a) Tensile-Strain, Flexural-Strain, and Modulus versus E-Glass fiber, Epoxy (Vol%), MWCNT(Vol%); (b) Tensile-Strain, Flexural-Strain at the break versus E-Glass fiber, Epoxy polymer (Vol%), and MWCNT(Vol%).

© 2025 The Authors. This article is licensed under a Creative Commons Attribution 4.0 International License.

The combination of 56 g E-glass fiber, an epoxy polymer comprising 60 vol% content, and a MWCNT content of 1.5 vol% yields the optimal minimum strain in both tensile and flexural properties.

3.6. Response Surface Method (RSM) Analysis

This analysis phase aims to extract significant insights from the completed experiment and assess the observed quality or improvement level. At this stage, we subject the data from each experimental run to comprehensive analysis and evaluation [15]. This study seeks to identify combinatory factors, including the concepts of larger being preferable and smaller being advantageous, for improvement purposes [27]. Due to the multiple samples evaluated in each experimental run, various analytical techniques were employed. The RSM was employed to predict the relationships between specific

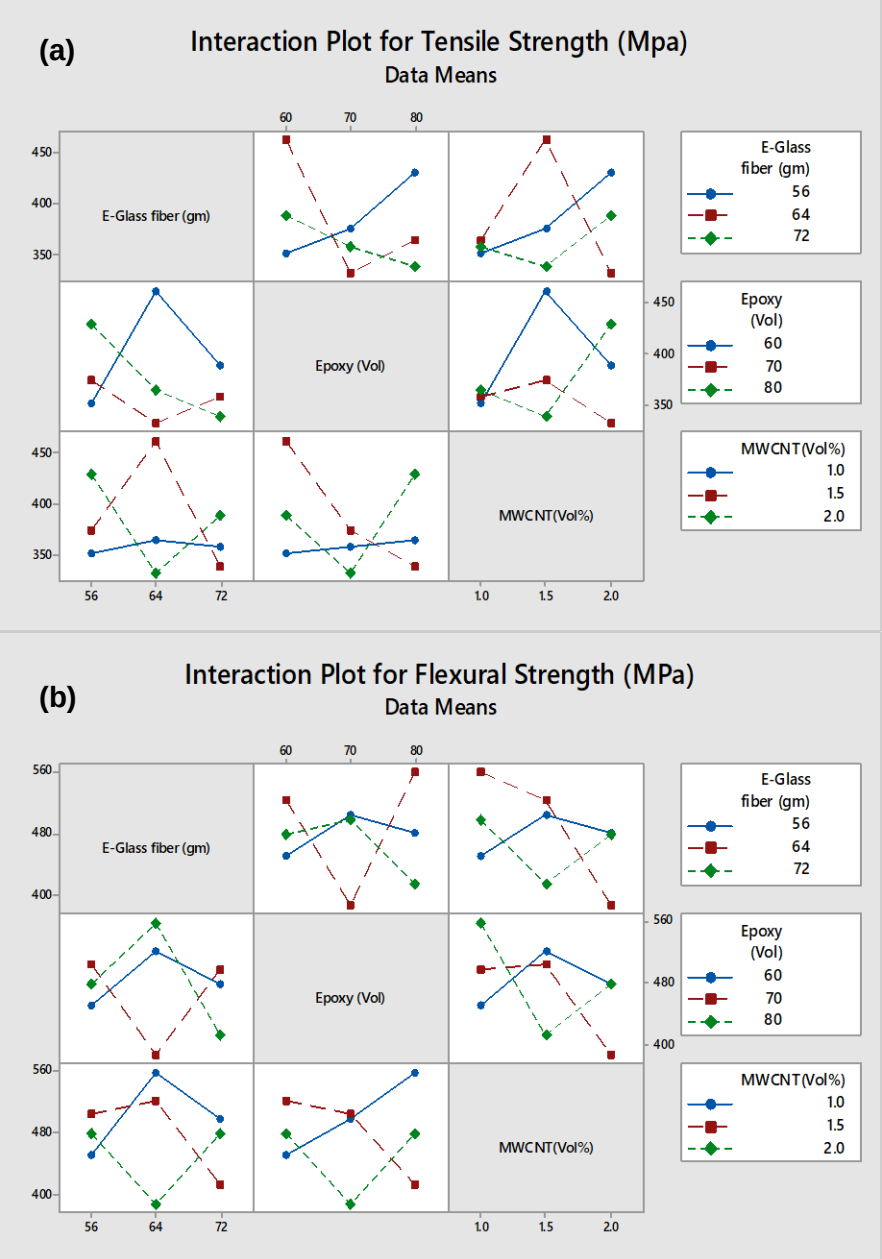

Figure 7. Interaction of E-Glass fiber, Epoxy, and MWCNT effects on (a) Tensile Strength, (b) Flexural Strength.

© 2025 The Authors. This article is licensed under a Creative Commons Attribution 4.0 International License.

measurable response variables and various experimental conditions that may affect those responses, as shown in Figure 7.

3.7. Prediction Mathematical Modelling

Experiments are repeated several times to achieve better results, which costs a lot of money and takes a lot of time. We use Response Surface Methodology (RSM) to solve this problem[15]. This method uses math and statistics to determine the best values for different process parameters and verify how well they work [24]. This study utilizes the Minitab software suite for modeling and optimization purposes. This software application creates a mathematical model of the second order. Figure 6 shows how to choose a characteristic. It shows that "Larger" is better, but "Smaller" also has certain advantages. Better signal-to-noise ratios are linked to better mechanical performance and lower levels of vibration. A lower signal-to-noise ratio means that the quality or performance of the machine has gotten worse [18]. In this case, S stands for the continuous beneficial change, whereas N stands for the unpredictable small change. The study utilized the larger-the-better criterion for tensile strength, flexural strength, and modulus, as delineated in Equation (5), while the smaller-the-better criterion was applied for tensile strain and flexural strain, as described in Equation (6).

$$\frac{S}{N} = -10\log_{10}\left[\frac{1}{n}\sum_{i=1}^{n}\frac{1}{X_i^{\,2}}\right] \quad (5)$$

$$\frac{S}{N} = -10\log_{10}\left[\frac{1}{n}\sum_{i=1}^{n}X_i^{\,2}\right] \quad (6)$$

Given n is the number of experiments run, and x_i is the response (tensile strength, flexural strength in the i^{th} experiment). For a Prediction model with three factors (x=MWCNT, y=epoxy polymer, and z=E-glass fiber), where t refers to tensile, f refers to flexural, generally, the equation is given as equations (7) – (12):

$$\sigma_t = -198x^2 - 0.701z * y + 564x + 43.7y + 47.6z - 2954 \quad (7)$$

$$E_t = 0.4884y^2 - 10.5534\,z^2 - 6.6262y * z + 5287x + 300.4y + 1907.5z - 61933 \quad (8)$$

$$\varepsilon_t = -0.04819x^2 - 0.00098z^2 - 0.000837x * z + 0.0003x * y + 0.1698x - 0.0007y + 0.3476 \quad (9)$$

$$\sigma_f = -197.7x^2 - 1.118y * z + 450x + 71.5y + 77.3z - 4667 \quad (10)$$

$$E_f = 0.04193y^2 + 0.03284z^2 - 0.1432x * z - 0.01301y * z + 9.12x - 4977y - 2914z + 285.2 \quad (11)$$

$$\varepsilon_f = -0.09667x^2 + 0.00017z^2 + 0.001167x * y + 0.19867x - 0.00168y - 0.021198z + 0.618 \quad (12)$$

3.8. Optimization of Mechanical Performance

The model that was created finds process parameters that try to get the best values for tensile strength, flexural strength, and modulus of elasticity while putting the least amount of strain on the material [24]. To get the best mechanical strength in a nanocomposite, you should use 1.5 vol% MWCNT nanofiller, 70 vol% epoxy polymer, and 72 g of E-glass fiber. The mathematical model predicts that the best nanocomposite sample will have a tensile strength of 99.468 MPa, a tensile modulus of 11.3 GPa, a flexural strength of 512 MPa, a flexural modulus of 37.8 GPa, and break strains for tensile and flexural tests of 0.003% and 0.005%, respectively. This ideal value was also recorded by [28], as shown in Figure 8.

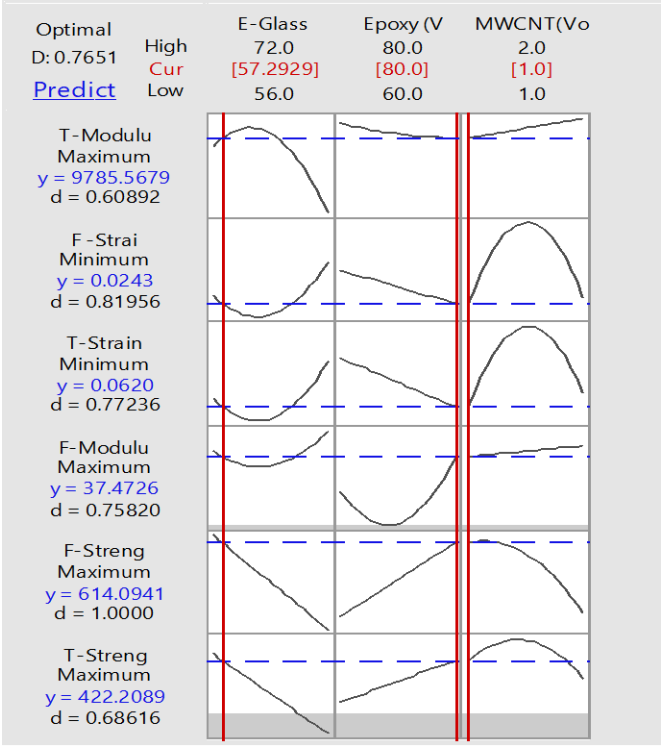

Figure 8. Optimization Plot.

© 2025 The Authors. This article is licensed under a Creative Commons Attribution 4.0 International License.

3.8.1. Surface Plots and Contour Plots

Figures 9 and 10 show the outcomes of changes in tensile strength, modulus, strain, and flexural strength that are caused by process parameters. Figure 9 shows contour plots, and Figure 10 shows surface plots [23]. These numbers show what the results were. You can utilize the shifts in hue to find differences and inconsistencies in the material's ultimate tensile and

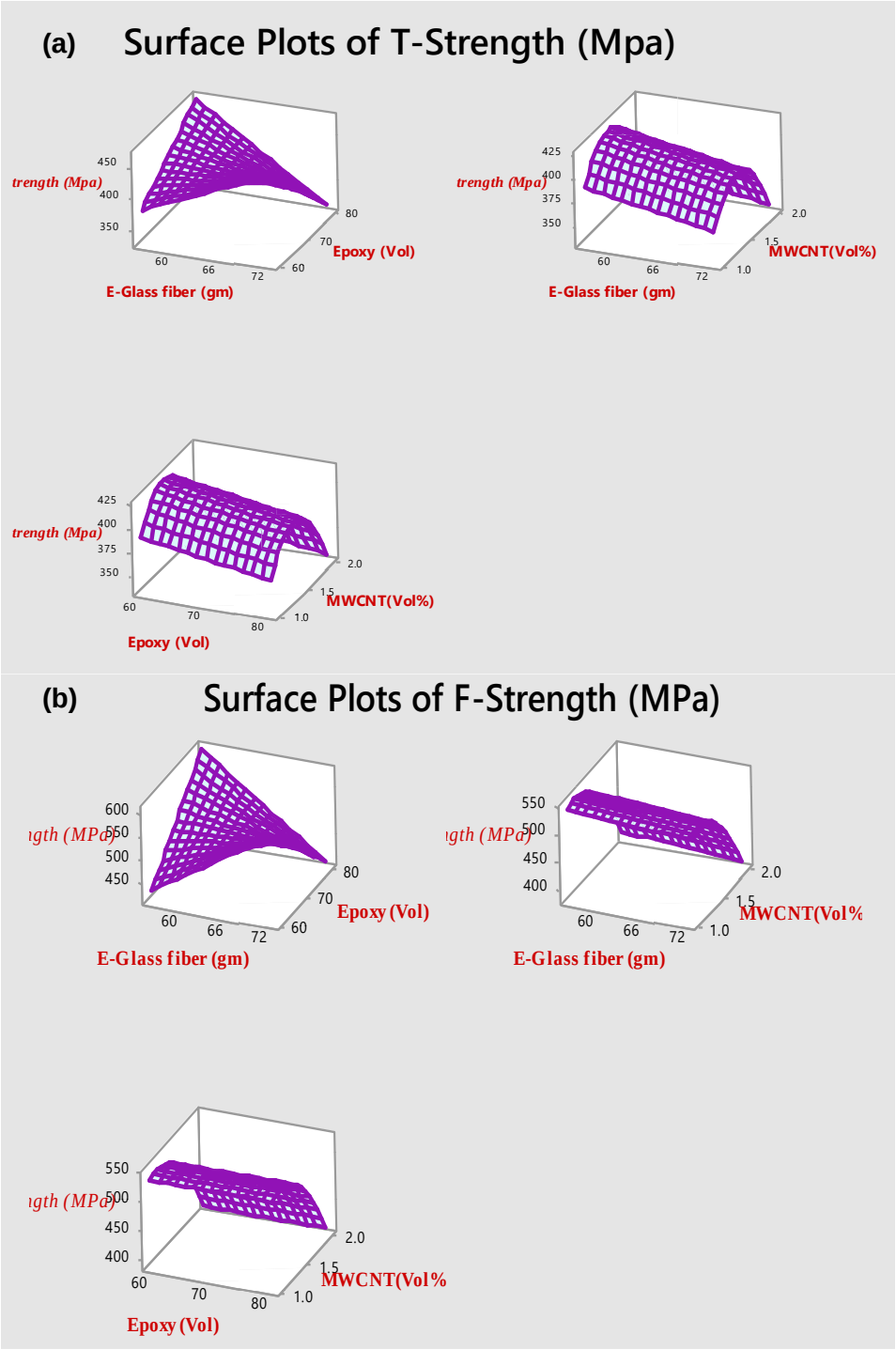

Figure 9. Surface plot (a) Tensile Strength, (b) Flexural Strength.

© 2025 The Authors. This article is licensed under a Creative Commons Attribution 4.0 International License.

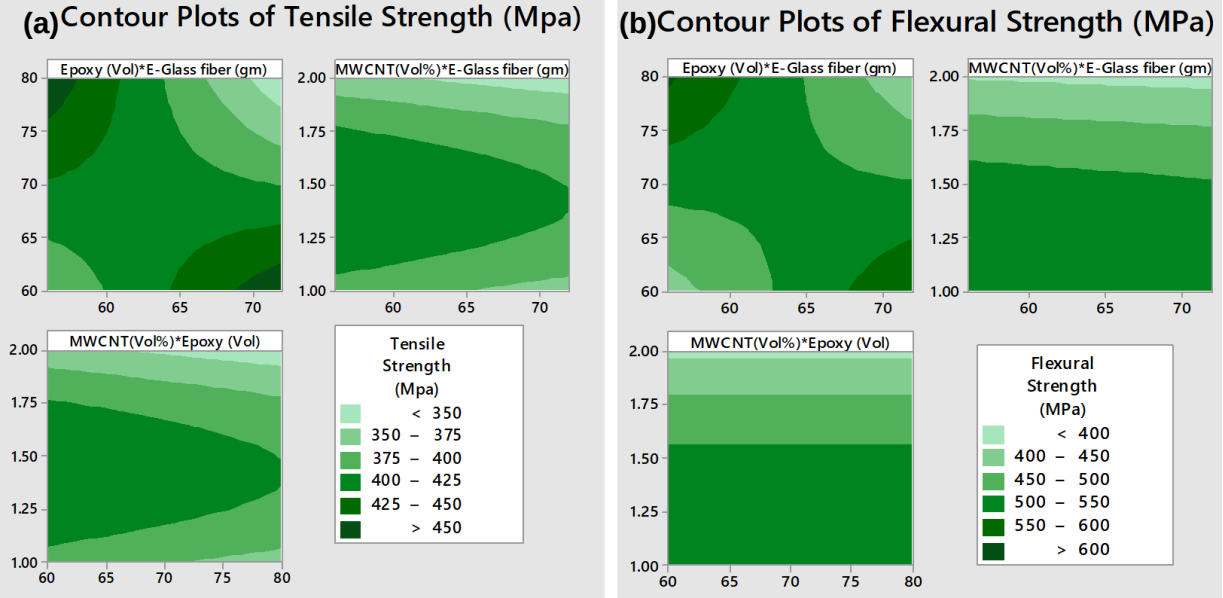

Figure 10. Contour Plot (a) Tensile Strength, (b) Flexural Strength.

flexural strength. The counterplot's color change from blue to light green and then back to green shows that the ultimate tensile and flexural strength values have gone up in a way that is proportional to the temperature change. Observing the graphs shows that when the number of passes goes up, the tensile strength and flexural strength of the material both go up in the same way.

3.8.2. Experimental Confirmation Analysis

The optimization process was finished, and then a confirmation analysis was performed using the optimal factor levels. This analysis was done after the optimization operation was finished. A total of seventy percent of epoxy polymer, seventy-two grams of E-glass fiber, and one volume percent of MWCNT were incorporated in these quantities [28]. In Table 3, the expected values and the experimental values are compared. Based on the data presented in Table 3, the experimental error between the predicted and experimental values aligns suitably with the anticipated value. The table's information leads to this conclusion.

4. Conclusions

This study investigates approaches to improve the strength of nanocomposites. We examined the grams of fiberglass, the volume percentage of multi-walled carbon nanotubes, and the volume percentage of epoxy polymers. The investigation employed various optimization techniques, including the Taguchi Method, Response Surface Methodology (RSM), and TOPSIS Analysis, to determine the optimal volume percentage of MWCNTs. The implementation of these steps enhanced the mechanical properties of the nanocomposite. Minitab software was utilized to formulate a hypothesis regarding potential outcomes. FTIR spectroscopy, scanning electron microscopy, and X-ray diffraction were employed to examine the morphology and

Table 3. Experimental and prediction verification

Response	Experiments	Predicted	Error (%)
Tensile Strength (MPa)	384.68	422.21	8.9
Tensile Modulus (GPa)	10.65	10.79	1.3
Flexural Strength (MPa)	559.18	614.1	8.94
Flexural Modulus (GPa)	36.7	37.47	2.06
Tensile-Strain at Break (%)	0.062	0.065	4.6
Flexural -Strain at Break (%)	0.08	0.085	5.9

© 2025 The Authors. This article is licensed under a Creative Commons Attribution 4.0 International License.

structural characteristics of the MWCNT powder and nanocomposite. The findings indicated a strong proximity between the epoxy matrix and the MWCNTs.

The morphological analysis of FE-SEM images indicates a significant enhancement in the COOH activity of MWCNTs incorporated into the epoxy polymer matrix. FTIR studies indicate that altering the chemical structure of MWCNTs containing carboxylic acid groups (COOH) is achievable. The interaction at the interface between the polymer and the acid-treated multi-walled carbon nanotubes (MWCNTs) appears to be more favorable due to the higher carbon content compared to oxygen. A servo-hydraulic machine was utilized to produce nanocomposite samples, which were subsequently analyzed to determine their strength and identify their most intricate features.

Table 3 summarizes that the verification test of the theoretical and experimental values shows that the error percentage stays about the same. The practical results indicated that the optimization model worked well for further processing and confirmed what was expected in theory. TOPSIS indicates that the MWNT concentration (1.5 vol%), the epoxy polymer (70 vol%), and the E-glass fiber-woven material (56 g) all have a major effect on the tensile and flexural modulus. The result means that both the tensile and flexural strength was optimized.

Acknowledgments

The author expresses gratitude to the Government of the United Republic of Tanzania, through the Rector of the National Institute of Transport in Dar es Salaam, and the Government of India, through the ICCR program, for their financial support during this study.

Conflict of Interest

The authors declare no conflict of interest.

References

1. A. Ali, et al. Carbon nanotube characteristics and enhancement effects on the mechanical features of polymer-based materials and structures – A review. *Journal of Materials Research and Technology*, **2023**, *24*, 6495.
2. A. Mostovoy, et al. Epoxy Nanocomposites Reinforced with Functionalized Carbon Nanotubes. *Polymers*, **2020**, *12*, 1816.
3. A. Kumar, K. Sharma, and A.R. Dixit. A review on the mechanical properties of polymer composites reinforced by carbon nanotubes and graphene. *Carbon Letters*, **2020**, *31*, 149.
4. A. Sharma and R. Kumar. Fabrication and characterization of carbon nanotubes-based Polymer nanocomposites. *INTEGRATED RESEARCH ADVANCES*, **2018**, *5*, 42.
5. D. Nyonyi, et al. Fabrication and Mechanical Analysis of Polymer Nanocomposites Reinforced With Multi-walled Carbon Nanotubes for Marine Applications. *Journal of Inorganic and Organometallic Polymers and Materials*, **2025**, *35*, 6709.
6. E.W. Fenta and B.A. Mebratie. Advancements in carbon nanotube-polymer composites: Enhancing properties and applications through advanced manufacturing techniques. *Heliyon*, **2024**, *10*, e36490.
7. M. Mirzapour, et al. Dispersion Characteristics, the Mechanical, Thermal Stability, and Durability Properties of Epoxy Nanocomposites Reinforced with Carbon Nanotubes, Graphene, or Graphene Oxide. *Polymers*, **2024**, *16*, 1836.
8. R. Islam Rubel, et al. Carbon nanotubes agglomeration in reinforced composites: A review. *AIMS Materials Science*, **2019**, *6*, 756.
9. S. Sharma, et al. Mechanical, morphological, and fracture-deformation behavior of MWCNTs-reinforced (Al–Cu–Mg–T351) alloy cast nanocomposites fabricated by optimized mechanical milling and powder metallurgy techniques. *Nanotechnology Reviews*, **2021**, *11*, 65.
10. U.U. Orji, et al. Development of polymer/carbon nanotubes incorporated sustainable materials for manufacturing of autobrake pad. *The International Journal of Advanced Manufacturing Technology*, **2024**, *132*, 3227.
11. R. Chipiri, et al. Experimental Investigation on Hybrid Laminated Composites Reinforced with Basalt-Pineapple-Bamboo Fibers. *Journal of Construction Engineering, Technology & Management*, **2023**, *13*, 9.
12. N. a and A. Faiyaz Ahmed. EVALUATION OF CARBON FIBRE REINFORCED POLYMERS USING FUZZY TOPSIS MCDM METHOD. *International Journal of Advanced Research*, **2023**, *11*, 1773.
13. U.A. Kumar, A. Kumar, and R. Nathawat. Taguchi design of experiments based optimization and experimental investigation of mechanical performance of hybrid epoxy nanocomposites. *Zastita Materijala*, **2023**, *64*, 433.
14. H. Sulistiani, et al. New TOPSIS: Modification of the TOPSIS Method for Objective Determination of Weighting. *International Journal of Intelligent Engineering and Systems*, **2024**, *17*, 991.

© 2025 The Authors. This article is licensed under a Creative Commons Attribution 4.0 International License.

15. S. Lamidi, et al. Applications of Response Surface Methodology (RSM) in Product Design, Development, and Process Optimization. *Research Advances and Applications*, **2020**, *1*, 1.

16. D. Nyonyi, V.S.P. Ventala, and S. Peravali. Graphene oxide nanofiller-reinforced polymer nanocomposites for marine applications: fabrication and mechanical testing. *Iranian Polymer Journal*, **2025**, https://doi.org/10.1007/s13726-025-01573-0.

17. D. Nyonyi, V.V.S. Prasad, and P. Swapna. Mechanical Performance Analysis and Seawater Absorption of Graphene Oxide (GO)-Reinforced Epoxy Nanocomposite for Marine Applications. *Journal of Materials Engineering and Performance*, **2025**, https://doi.org/10.1007/s11665-025-12328-6.

18. L. Adamo, et al., *A Response Surface Methodology Approach to Develop a Multiphysics Simulation Model of a Tensile Friction Test*, in *The 28th Saxon Conference on Forming Technology SFU and the 7th International Conference on Accuracy in Forming Technology ICAFT*. **2022**, MDPI. p. 22.

19. S. Bhaskar, M. Kumar, and A. Patnaik. Application of Hybrid AHP-TOPSIS Technique in Analyzing Material Performance of Silicon Carbide Ceramic Particulate Reinforced AA2024 Alloy Composite. *Silicon*, **2020**, *12*, 1075.

20. K. S V H, L. K V, and G.N. Yogavardhan Swamy. Nanocomposite Materials: Enhancing Mechanical and Thermal Properties Using Carbon Nanotubes. *Library Progress International,*, **2024**, *44*, 19256.

21. P.P. Pandey. Preparation and Characterization of Polymer Nanocomposites. *Soft Nanoscience Letters*, **2020**, *10*, 1.

22. P. Hiremath, et al. Investigation on tensile properties and analysis of wear property of glass fiber-epoxy-nanoclay ternary nanocomposite using response surface methodology. *Cogent Engineering*, **2021**, *8*, 1.

23. R. Butola, et al. Experimental analysis and optimization of process parameters using response surface methodology of surface nanocomposites fabricated by friction stir processing. *Journal of Nanomaterials, Nanoengineering and Nanosystems*, **2024**, *238*, 119.

24. S. Kumar and S. Balachander. Studying the effect of reinforcement parameters on the mechanical properties of natural fibre-woven composites by Taguchi method. *Journal of Industrial Textile*, **2020**, *50*, 133.

25. Haniel, B. Bawono, and P.W. Anggoro. Optimization of Characteristics Polymer Composite Reinforced Kenaf and Jute Fiber Using Taguchi-Response Surface Methodology Approach. *Journal of Natural Fibers*, **2023**, *20*.

26. K. Manjula and B.K. Narendra. An Analysis Using the Taguchi Optimization Process to Statistically Investigate the Mechanical Properties of Composite Materials. *Journal of the Institute of Engineers India Series D* **2025**, *106*, 825.

27. Y.R. Almahamid, S.H. Hussein-Al-Ali, and M.K. Haddad. Application of Factorial Design and Response Surface Methodology in the Optimization of Clindamycin Nanocomposites. *Journal of Nanomaterials*, **2022**, *2022*, 1967606.

28. J. R, et al. OPTIMIZATION OF HYBRID COMPOSITE USING TAGUCHI METHOD. *International Journal of Advanced Research Trends in Engineering and Technology (IJARTET)*, **2016**, *3*, 430.

© 2025 The Authors. Authors retain the copyright and full publishing rights. This article is licensed under a Creative Commons Attribution 4.0 BY International License.

© 2025 The Authors. This article is licensed under a Creative Commons Attribution 4.0 International License.